COHERENT CONTROL OF LASER FIELD AND SPECTROSCOPY IN DENSE ATOMIC VAPOR

A Dissertation

by

HEBIN LI

Submitted to the Office of Graduate Studies of
Texas A&M University
in partial fulfillment of the requirements for the degree of

DOCTOR OF PHILOSOPHY

May 2010

Major Subject: Physics

COHERENT CONTROL OF LASER FIELD AND SPECTROSCOPY IN DENSE ATOMIC VAPOR

A Dissertation

by

HEBIN LI

Submitted to the Office of Graduate Studies of
Texas A&M University
in partial fulfillment of the requirements for the degree of

DOCTOR OF PHILOSOPHY

Approved by:

Chair of Committee,	Marlan O. Scully
Committee Members,	Philip R. Hemmer
	Alexei V. Sokolov
	George R. Welch
	M. Suhail Zubairy
Head of Department,	Edward S. Fry

May 2010

Major Subject: Physics

ABSTRACT

Coherent Control of Laser Field and Spectroscopy
in Dense Atomic Vapor. (May 2010)
Hebin Li, B.S., Wuhan University, China
Chair of Advisory Committee: Dr. Marlan O. Scully

Coherent effects are studied in a dense atomic vapor driven by laser fields. With optical properties dramatically modified by these effects, the medium can be used to manipulate some of the properties of laser field. Our experiments demonstrate the coherent control over transmission, spatial distribution and noise feature of the laser field interacting with coherent media. The results have potential applications in the field such as precision metrology, precision spectroscopy, optical imaging and lithography.

We develop an experiment to investigate the atomic excitation by few-cycle radio frequency (RF) pulses interacting with Zeeman sublevels. The system provides the flexibility to fully control all parameters of RF pulses. Such a flexibility can not be achieved in optical domain. Based on this system, experiments can be conducted to simulate processes in ultra-short laser physics. In particular, we study the carrier-envelope effect of few-cycle pulses and the strong off-resonant excitation by short pulses.

We also discuss the selective reflection spectrum on a highly dense atomic vapor in which the dipole-dipole interaction can not be neglected. The spectrum broadening due to dipole-dipole interaction is much broader than the Doppler broadening. Our experiments show that the excitation by a pump laser can reduce the dipole-dipole interaction, thus reduce the broadening and improve the spectral resolution. The excitation dependence is studied at various atomic densities.

To my wife Lei

ACKNOWLEDGMENTS

The present dissertation is the result of a collective effort. Many people influenced, guided, and helped me and contributed to this effort. I am thankful to each and everyone of them.

First of all, I would like to thank my advisor, Professor Marlan O. Scully for his support, inspiration, guidance and providing opportunities for my research and academic development I could never have imagined. I am especially thankful to Dr. Vladimir A. Sautenkov and Dr. Yuri V. Rostovtsev who taught me everything I know in the lab and what it takes to be a scientist. Their enthusiasm, talent and energy inspired most of the work in this dissertation. I also would like to acknowledge the important guidance and contributions from Drs. Philip R. Hemmer, Dudley R. Herschbach, Michael M. Kash, Alexei V. Sokolov, George R. Welch, and M. Suhail Zubairy.

It is my pleasure to thank P. Anisimov, G.O. Ariunbold, H. Chen, J.P. Davis, H. Eleuch, P.S. Hsu, F.A. Narducci, Z.-E. Sariyanni, D. Sarkisyan, A. Svidzinsky, T.S. Varzhapetyan, A. Zhang, M. Zhi for collaborations and useful discussions. I acknowledge the support of the Robert A. Welch Foundation and the Office of Naval Research.

Finally, I would like to thank all my friends and family, especially my parents and my wife, Lei Wu, for their love and their spiritual and physical support.

TABLE OF CONTENTS

CHAPTER Page

LIST OF FIGURES

FIGURE Page

FIGURE Page

FIGURE Page

FIGURE Page

FIGURE Page

FIGURE Page

FIGURE Page

FIGURE Page

CHAPTER I

INTRODUCTION

The interaction of light with matter has been of great interest in modern physics. Recent advances in laser technology make it accessible to manipulate the properties of a medium via laser beams, thus to create new media with modified optical properties which sometimes do not exist in natural materials. For example, applying laser fields may substantially modify the absorptive and dispersive properties of a medium. The light-matter interaction is always an interplay of two aspects. The light changes properties of media on the one hand, and the medium with altered properties acts back on the light field on the other. Therefore, one can take the advantage of light-induced properties in media to control properties of light field. This is the key point which motivates the present studies.

Two aspects of light-matter interaction become even more interesting in the cases where a superposition of states is excited so that the system involves atomic coherence and quantum interference [1]. Spectacular examples such as Coherent Population Trapping (CPT) [2], Electromagnetically Induced Transparency (EIT) [3] and Lasing Without Inversion (LWI) [4] have shown the importance of atomic coherence to both fundamental physics and innovative applications. In EIT, for example, under the coherent driving of two laser fields, atoms in the medium can be pumped into the "dark" state which is a coherent superposition of atomic levels. The atoms in the "dark" state do not interact with light, therefore the medium is transparent to the light despite being on resonance. Associated with the vanishing absorption, the medium also displays an extreme nonlinearity in dispersion. In this way, the coher-

---

´This dissertation follows the style and format of Physical Review A.

ent interaction of light and atoms creates a new state of matter in which one can manipulate the properties such as absorption and dispersion. The interaction can lead to many remarkable phenomena such as enhancement of the index of refraction [5, 6] and light induced chirality in a non-chiral medium [7]. On the other hand, the extraordinary properties of coherently driven media can be used to control light fields in a counter-intuitive way to realize slow, fast and stored light [8, 9, 10], forward Brillouin scattering [11, 12] and electromagnetically induced coherent backscattering [13], to name a few. The coherent interaction of light with matter allows us to manipulate the properties of both media and light fields. Coherent phenomena also play a crucial role in other fields such as creation of a new type of matter (Bose-Einstein condensation), precision metrology (atomic clock and magnetometer), quantum computing and quantum information.

The subject of my present research is the quantum coherent effects in atom-field interaction and their applications. The major objective is to obtain better understanding of the fundamental properties of atom-field interaction in general and to study the coherent control of laser fields, the excitation by few-cycle pulses and the reflection spectrum, in a dense atomic vapor in particular.

The coherent medium can be utilized to control a laser field, for example, the spatial properties of laser field. In a simplified version of laser-atom interaction, the laser beam is considered as a geometric line which is sufficient for some measurements such as absorption. While in reality, the laser beam is not a plane wave and does not have an uniform intensity distribution in the plane transverse to the direction of propagation. In EIT, the properties such as absorption and index of refraction strongly depend on the laser intensity in a nonlinear way. Therefore, the inhomogeneous distribution of laser intensity may cause a certain inhomogeneity in the medium. For example, a drive beam with the Gaussian profile can induce a controllable gradient of

the index of refraction which can deflect laser beams. A careful arrangement of the intensity distributions of drive and probe beams can create an optical pattern with the characteristic size beating the diffraction limit.

One of the important topics in light-matter interaction is the interaction of medium with ultra short laser pulses which contains only a few cycles of the field oscillations. Modern lasers are capable of generating short bursts of radiation, even atto-second pulses. It remains a huge technology challenge to fully control all of the parameters such as pulse shape and carrier-envelope phase. However, in the radio frequency domain, it is easy to generate a few-cycle pulse with all parameters controlled. Such a field in radio frequency can be coupled with a low energy transition such as the ones between Zeeman sublevels. The combination of radio frequency fields and Zeeman sublevels provides an excellent model system to study the excitation by ultra-short laser pulses.

It is important study the nonlinear optical properties of a highly dense atomic vapor ($N > 10^{16}$ cm^{-3}). The conventional absorption spectroscopy may fail because of the large optical density, while a proper tool is the reflection spectroscopy. The reflectivity from an interface between a transparent dielectric and absorbing vapor has a resonant structure near an absorption line of the atomic vapor, this is known as selective reflection. In a highly dense atomic vapor, the dipole-dipole interaction between atoms in excite state and ground state dominates the self-broadening in spectrum. The selective reflection can be used to study the dipole-dipole interaction in the medium.

Besides the interests in fundamental understanding of atom-field interaction, the research also leads to innovative applications in the fields such as precision metrology, optical imaging and lithography, XUV generation and precision spectroscopy.

This dissertation is organized as the following: Chapter II reviews the semiclas-

sical theory of light-matter interaction; Chapter III studies the influence of phase in optical or microwave fields on EIT; Chapter IV studies the spatial control of laser fields in a coherent medium; Chapter V studies the intensity correlation of atomic excess noise in a coherent medium; Chapter VI studies the atomic excitation by few cycle radio frequency pulses; Chapter VII studies the reflection spectroscopy on highly dense atomic vapor; and Chapter VIII summarize the results in this dissertation.

CHAPTER II

THEORETICAL BASIS OF LIGHT-MATTER INTERACTION

This chapter reviews the semiclassical theory of light-matter interaction, which treats atoms quantum mechanically whereas electromagnetic fields classically. Simple examples are reviewed to introduce the notion of quantum inference and atomic coherence, as well as the notions which will be used in later chapters. The chapter is organized as the following. The first section reviews the theory of a monochromatic field interacting with a two-level atom. The second section reviews the density matrix formalism. The third section reviews how to describe the propagation of a field in a resonant medium. The final section deals with a three level system coherently coupled with two laser fields.

A. Light interacting with a two-level atom

Following the standard textbooks such as [1], we present the semiclassical theory of light-matter interactions. The simplest example is that a monochromatic field interacts with a two-level system.

Consider a electromagnetic field with the frequency ν interacting with an atom which has the excited state $|a\rangle$ and the ground state $|b\rangle$, as shown in Fig. 1. In the dipole approximation, the field can be expressed as $E(t) = \mathscr{E} \cos(\nu t)$. The Hamiltonian of the system can be written as $H = H_0 + H_I$, where H_0 is the unperturbed part given by

$$H_0 = \hbar\omega_a |a\rangle\langle a| + \hbar\omega_b |b\rangle\langle b| \ , \tag{2.1}$$

where ω_a and ω_b are atomic frequencies such that $H_0|a\rangle = \hbar\omega_a|a\rangle$ and $H_0|b\rangle = \hbar\omega_b|b\rangle$.

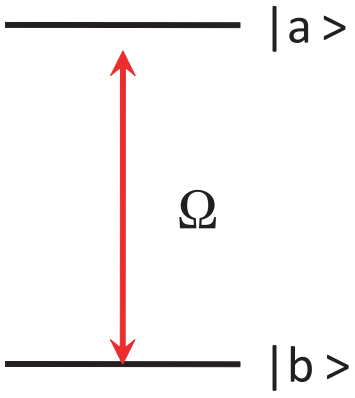

Fig. 1. An electromagnetic field with the Rabi frequency Ω interacts with a two-level atom. The excited state is $|a\rangle$ and the ground state is $|b\rangle$.

H_I represents the interaction between the field and the atom,

$$\begin{aligned} H_I &= -(\wp_{ab}|a\rangle\langle b| + \wp_{ba}|b\rangle\langle a|)\mathscr{E}\cos(\nu t) \\ &= -\hbar(\Omega\cos(\nu t)|a\rangle\langle b| + \Omega^*\cos(\nu t)|b\rangle\langle a|) \ , \end{aligned} \tag{2.2}$$

where $\wp_{ab} = \wp_{ba}^* = e\langle a|x|b\rangle$ is the matrix element of the electric dipole moment. Ω is the Rabi frequency defined as $\Omega = \wp_{ba}\mathscr{E}/\hbar$. The wave function of the system can be expressed in the basis of the eigenstates of H_0 as

$$|\psi\rangle = C_a|a\rangle + C_b|b\rangle \ . \tag{2.3}$$

The corresponding Schrödinger equation is

$$i\hbar\frac{\partial}{\partial t}|\psi\rangle = H|\psi\rangle \ . \tag{2.4}$$

Plug equations (2.1) (2.2) (2.3) into the Schrödinger equation (2.4), we obtain the equations of motion for the probability amplitudes

$$\dot{C}_a = -i\omega_a C_a + i\Omega\cos(\nu t)C_b \ , \tag{2.5}$$

$$\dot{C}_b = -i\omega_b C_b + i\Omega^* \cos(\nu t) C_a \ . \tag{2.6}$$

Use the slowly varying amplitude approximation $C_a = c_a e^{-i\omega_a t}$ and $C_b = c_b e^{-i\omega_b t}$, and the rotation wave approximation in which the counter-rotating terms including $e^{\pm i(\omega+\nu)t}$ are ignored, equations (2.5) and (2.6) become

$$\dot{c}_a = i\frac{\Omega}{2} e^{i(\omega-\nu)t} c_b \ , \tag{2.7}$$

$$\dot{c}_b = i\frac{\Omega^*}{2} e^{-i(\omega-\nu)t} c_a \ , \tag{2.8}$$

where $\omega = \omega_a - \omega_b$. These equations have exact solutions for an arbitrary detuning $\Delta = \omega - \nu$. For simplicity, we consider the resonant case ($\Delta = 0$) to understand the physics in the process. Assume the initial conditions $c_a(t=0) = 0$ and $c_b(t=0) = 1$, we have the solution

$$c_a = \sin(\frac{|\Omega|}{2} t) \ , \tag{2.9}$$

$$c_b = -i\frac{\Omega^*}{|\Omega|} \cos(\frac{|\Omega|}{2} t) \ . \tag{2.10}$$

So the inversion is given by $W(t) = |c_a(t)|^2 - |c_b(t)|^2 = -\cos(|\Omega| t)$ which indicates the inversion oscillates between -1 and 1 at the Rabi frequency Ω. The population of atoms is driven between the excited and ground states as a result of the laser-atoms interaction. For a certain atom, the frequency of oscillation represents the strength of the laser field.

B. Density matrix representation

In principle, a state vector $|\psi\rangle$ in Hilbert space contains all possible information for a given quantum mechanical system, while it does not provide a good approach in many practical situations. In many cases we may not know the exact form of $|\psi\rangle$, but

only the probability P_ψ of being in the state $|\psi\rangle$. To obtain the expectation value of an operator, we need to take the quantum mechanical average as well as the ensemble average for macroscopic objects.

A quantum mechanical system can be represented by a density operator and it provides a practical approach in many situations. The density operator is defined by

$$\rho = \sum_\psi P_\psi |\psi\rangle\langle\psi| \ . \tag{2.11}$$

If the probability P_ψ is nonzero only for a state $|\psi_0\rangle$, the state is called a pure state and the density operator is given by $\rho = |\psi_0\rangle\langle\psi_0|$. Knowing the density operator, we can calculate the expectation value of an operator $\hat{O}$

$$\begin{aligned} \langle\hat{O}\rangle &= \sum_\psi P_\psi \langle\psi|\hat{O}|\psi\rangle \\ &= \mathrm{Tr}(\hat{O}\rho) \ . \end{aligned} \tag{2.12}$$

To find out the physical meaning of the density operator, we can write the density operator in a matrix form for a given basis $\{|n\rangle\}$. The density matrix has matrix elements $\rho_{nm} = \langle n|\rho|m\rangle$. The diagonal elements ρ_{nn} represent the probabilities of being the states $|n\rangle$. The off-diagonal elements ρ_{nm} $(n \neq m)$ represent the coherence between the states $|n\rangle$ and $|m\rangle$, in particular cases it could be the dipole moment operator.

As an example, we consider a two level system in the state $|\psi\rangle = C_a|a\rangle + C_b|b\rangle$. The density matrix operator can be written as

$$\rho = |\psi\rangle\langle\psi| = |C_a|^2|a\rangle\langle a| + |C_b|^2|b\rangle\langle b| + C_aC_b^*|a\rangle\langle b| + C_bC_a^*|b\rangle\langle a|. \tag{2.13}$$

The matrix elements are given by $\rho_{aa} = |C_a|^2$, $\rho_{ab} = C_aC_b^*$, $\rho_{ba} = \rho_{ab}^* = C_a^*C_b$, and $\rho_{bb} = |C_b|^2$. We can see that ρ_{aa} and ρ_{bb} are the probabilities of being in the states $|a\rangle$

and $|b\rangle$. The off-diagonal elements ρ_{ab} and ρ_{ba} are related with the atomic polarization $P = \rho_{ab}\wp_{ba} + \rho_{ba}\wp_{ab}$.

For a particular system described by the Hamiltonian H, the equations of motion for the density matrix are needed to study the dynamics of the system. Staring from the Schrödinger equation (2.4), we have

$$|\dot{\psi}\rangle = -\frac{i}{\hbar}H|\psi\rangle \ . \tag{2.14}$$

From equation (2.11), the time derivative of ρ is given by

$$\dot{\rho} = \sum_{\psi} P_{\psi}(|\dot{\psi}\rangle\langle\psi| + |\psi\rangle\langle\dot{\psi}|) \ . \tag{2.15}$$

Plug (2.14) into equation (2.15), we obtain the equation of motion for the density matrix,

$$\dot{\rho} = -\frac{i}{\hbar}[H, \rho] \ . \tag{2.16}$$

The equation of motion (2.16) is not completed to describe a real system since the decay of atomic levels are not considered. The decay can be considered by including phenomenological decay terms in the equation of motion. Define a relaxation matrix Γ by the equation $\langle n|\Gamma|m\rangle = \gamma_n\delta_{nm}$, the equation of motion with decay terms can be written as

$$\dot{\rho} = -\frac{i}{\hbar}[H, \rho] - \frac{1}{2}\{\Gamma, \rho\} \ , \tag{2.17}$$

where $\{\Gamma, \rho\} = \Gamma\rho + \rho\Gamma$.

We now use the density matrix to treat the two-level atom problem in section A. The Hamiltonian of the system is given by $H = H_0 + H_I$ with H_0 and H_I shown (2.1) and (2.2). Plug the Hamiltonian into equation (2.17), we obtain the equations of motion for the elements of the density matrix,

$$\dot{\rho}_{aa} \ = \ i\Omega\cos(\nu t)\rho_{ba} - i\Omega^*\cos(\nu t)\rho_{ab} - \gamma_a\rho_{aa} \ , \tag{2.18}$$

$$\dot{\rho}_{bb} = i\Omega^* \cos(\nu t)\rho_{ab} - i\Omega \cos(\nu t)\rho_{ba} - \gamma_b \rho_{bb} \ , \tag{2.19}$$

$$\dot{\rho}_{ab} = -i(\omega + \gamma_{ab})\rho_{ab} - i\Omega \cos(\nu t)(\rho_{aa} - \rho_{bb}) \ , \tag{2.20}$$

where $\omega = \omega_a - \omega_b$ and $\gamma_{ab} = \frac{1}{2}(\gamma_a + \gamma_b)$. With the initial conditions given, we are able to solve these equations for the matrix elements ρ_{aa}, ρ_{bb}, ρ_{ab} and ρ_{ba} which give us the information of the system.

C. Light propagation in a resonant medium

So far we have considered a simplified case in which a single mode laser field interacts with a single atom. However, many problems involve a laser beam propagating in an ensemble of atoms. In this case, the light-atom interaction is position dependent. Moreover, we need to consider the influence of the field on atoms on one hand, and how the atoms affect back on the field on the other. The applied field induces not only coherence and transitions but also atomic electric dipole moments. The dipole moment of a single atom may have a negligible effect on the field, but a large number of atoms can significantly affect the field. A self-consistent theory taking account the effect of both the field and the atoms is needed to calculate the evolution of the system.

The electromagnetic field is governed by the Maxwell equations. In free space, they can be written as the following

$$\nabla \cdot \mathbf{E} = 0; \tag{2.21}$$

$$\nabla \cdot \mathbf{B} = 0; \tag{2.22}$$

$$\nabla \times \mathbf{E} = -\frac{\partial \mathbf{B}}{\partial t}; \tag{2.23}$$

$$\nabla \times \mathbf{B} = \frac{1}{c^2}\frac{\partial}{\partial t}(\mathbf{E} + \frac{1}{\epsilon_0}\mathbf{P}); \tag{2.24}$$

take the curl of equation (2.23), use the identity $\nabla \times (\nabla \times \mathbf{A}) = \nabla(\nabla \cdot \mathbf{A}) - \nabla^2 \mathbf{A}$ and equations (2.21,2.24), we then have the wave equation of the electric field as the following,

$$\nabla^2 \mathbf{E} - \frac{1}{c^2}\frac{\partial^2}{\partial t^2}\mathbf{E} = \frac{1}{\epsilon_0 c^2}\frac{\partial^2}{\partial t^2}\mathbf{P}. \tag{2.25}$$

We now use the so called slowly varying amplitude approximation to reduce this second order differential wave equation to a first order differential equation. A nearly monochromatic electric field can be written in a form with a slowly varying amplitude $\mathcal{E}(r,t)$. Let us introduce slowly varying amplitudes for both the electric field and the polarization,

$$\mathbf{E}(r,t) = \mathcal{E}(r,t)e^{ikz-i\nu t} + c.c. \tag{2.26}$$

$$\mathbf{P}(r,t) = \mathcal{P}(r,t)e^{ikz-i\nu t} + c.c. \tag{2.27}$$

Take the derivatives of equations (2.26,2.27), we have

$$\nabla^2 \mathbf{E} = (\nabla_\perp^2 \mathcal{E} + 2ik\frac{\partial}{\partial z}\mathcal{E} - k^2\mathcal{E})e^{ikz-i\nu t} + c.c. \tag{2.28}$$

$$\frac{\partial^2}{\partial t^2}\mathbf{E} = (\frac{\partial^2}{\partial t^2}\mathcal{E} - 2i\nu\frac{\partial}{\partial t}\mathcal{E} - \nu^2\mathcal{E})e^{ikz-i\nu t} + c.c. \tag{2.29}$$

$$\frac{\partial^2}{\partial t^2}\mathbf{P} = (\frac{\partial^2}{\partial t^2}\mathcal{P} - 2i\nu\frac{\partial}{\partial t}\mathcal{P} - \nu^2\mathcal{P})e^{ikz-i\nu t} + c.c. \tag{2.30}$$

where $\nabla_\perp^2 = \frac{\partial^2}{\partial x^2} + \frac{\partial^2}{\partial y^2}$ is in the transverse direction. Substitute these equations into equation (2.25), we have

$$\nabla_\perp^2 \mathcal{E} + 2ik\frac{\partial}{\partial z}\mathcal{E} - k^2\mathcal{E} - \frac{1}{c^2}(\frac{\partial^2}{\partial t^2}\mathcal{E} - 2i\nu\frac{\partial}{\partial t}\mathcal{E} - \nu^2\mathcal{E}) = \frac{1}{\epsilon_0 c^2}(\frac{\partial^2}{\partial t^2}\mathcal{P} - 2i\nu\frac{\partial}{\partial t}\mathcal{P} - \nu^2\mathcal{P}). \tag{2.31}$$

In the slowly varying amplitude approximation, we have $|\frac{\partial}{\partial t}\mathcal{P}| \gg |\nu\mathcal{P}|$, $|\frac{\partial}{\partial t}\mathcal{E}| \gg |\nu\mathcal{E}|$, $|\frac{\partial}{\partial z}\mathcal{P}| \gg |k\mathcal{E}|$. Together with the relation $\nu = ck$, equation (2.31) can be reduced into

$$\frac{1}{2ik}\nabla_\perp^2 \mathcal{E} + \frac{\partial}{\partial z}\mathcal{E} + \frac{1}{c}\frac{\partial}{\partial t}\mathcal{E} = \frac{ik}{2\epsilon_0}\mathcal{P}. \tag{2.32}$$

This is a self-consistent equation which describes a laser field interacting with an ensemble of atoms. The right side of the equation is the source of the field which is driven by the local field. The left side of the equation describes the evolution of the field in both space and time. Particularly, the first term is related with the field distribution in the transverse direction of the laser beam. The term is important to the transverse effects such as beam focusing, it can not be neglected whenever the beam profile concerns. However, in the cases we care about the overall power rather than the variation in the transverse direction, the first term can be ignored. The second term is related with the field propagation. It gives the field distribution along the direction of propagation. The third term gives the time dependence of the field.

For a continuous wave, the slowly varying amplitude $\mathcal{E}$ does not change in time, i.e. $\partial\mathcal{E}/\partial t = 0$. Therefore, equation (2.32) becomes

$$\frac{1}{2ik}\nabla_{\perp}^{2}\mathcal{E} + \frac{\partial}{\partial z}\mathcal{E} = \frac{ik}{2\epsilon_0}\mathcal{P}. \tag{2.33}$$

Use the Rabi frequency $\Omega_p = \wp_{ba}\mathcal{E}/\hbar$ and the polarization $\mathcal{P} = N\wp_{ba}\rho_{ab}$, substitute them into equation (2.33), we have

$$\frac{1}{2ik}\nabla_{\perp}^{2}\Omega_p + \frac{\partial}{\partial z}\Omega_p = \frac{iNk\wp_{ba}^{2}}{2\hbar\epsilon_0}\rho_{ab} \tag{2.34}$$

Identifying the dipole moment with the spontaneous emission rate $\gamma_r = \wp_{ba}^{2}k^3/3\pi\epsilon_0\hbar$ and using $k = 2\pi/\lambda$, we have

$$\frac{1}{2ik}\nabla_{\perp}^{2}\Omega_p + \frac{\partial}{\partial z}\Omega_p = i\eta\rho_{ab} \tag{2.35}$$

where $\eta = 3\lambda^2 N\gamma_r/8\pi$ is the coupling coefficient. Equation (2.35) is used to describe most of experiments in the following text involving a continuous wave laser field propagates in an atomic gas.

D. Three level Λ system

A two level system is theoretically the simplest case of light-atom interaction. However, it is hard to realize a two level system experimentally. The simplest realistic system is a three level system. This section reviews a three level atom interacting with two laser fields. The coherent interaction between the atom and two laser fields makes it possible to have the quantum interference of two excitation pathways. As a result, it dramatically changes the optical properties of the atoms and results in many counter intuitive phenomena such as Electromagnetically Induced Transparency (EIT) [1, 14, 3].

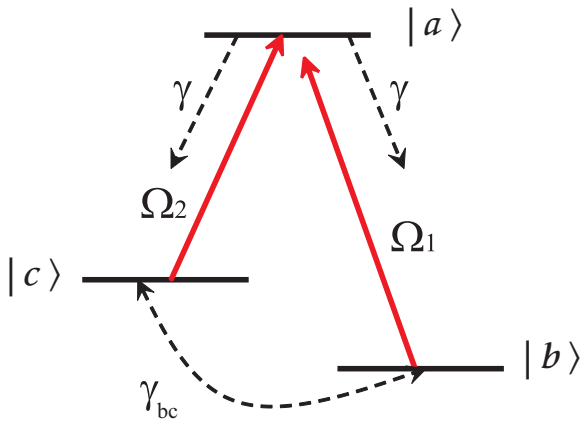

Fig. 2. The energy diagram of a three level atom interacting with two laser fields Ω_1 and Ω_2. Such a system is called a Λ scheme.

We consider an atom with the energy scheme shown in Fig. 2 interacting with two laser fields with Rabi frequencies Ω_1 and Ω_2. The fields with Rabi frequencies Ω_1 and Ω_2 are called probe and drive respectively. The Hamiltonian of the system can be written as $H = H_0 + H_I$, where

$$H_0 = \hbar\omega_a|a\rangle\langle a| + \hbar\omega_b|b\rangle\langle b| + \hbar\omega_c|c\rangle\langle c|, \tag{2.36}$$

$$H_I = -\hbar(\Omega_1 e^{-i\nu_1 t}|a\rangle\langle b| + \Omega_2 e^{-i\nu_2 t}|a\rangle\langle c| + h.c.), \tag{2.37}$$

where ω_i $(i = a, b, c)$ are the corresponding atomic frequencies, and ν_i $(i = 1, 2)$ are the optical frequencies. Plug the Hamiltonian into the equation of motion $\dot{\hat{\rho}} = -\frac{i}{\hbar}[H, \hat{\rho}] - \frac{1}{2}\{\Gamma, \hat{\rho}\}$ for the density operator $\hat{\rho}$, we then have the equations of motion as the following,

$$\dot{\hat{\rho}}_{aa} = i\Omega_1 e^{-i\nu_1 t}\hat{\rho}_{ba} - i\Omega_1^* e^{i\nu_1 t}\hat{\rho}_{ab} + i\Omega_2 e^{-i\nu_2 t}\hat{\rho}_{ca} - i\Omega_2^* e^{i\nu_2 t}\hat{\rho}_{ac} - 2\gamma\hat{\rho}_{aa} \tag{2.38}$$

$$\dot{\hat{\rho}}_{bb} = i\Omega_1^* e^{i\nu_1 t}\hat{\rho}_{ab} - i\Omega_1 e^{-i\nu_1 t}\hat{\rho}_{ba} - \gamma\hat{\rho}_{bb} - \gamma_{bc}\hat{\rho}_{bb} + \gamma_{bc}\hat{\rho}_{cc} \tag{2.39}$$

$$\dot{\hat{\rho}}_{cc} = i\Omega_2^* e^{i\nu_2 t}\hat{\rho}_{ac} - i\Omega_2 e^{-i\nu_2 t}\hat{\rho}_{ca} - \gamma\hat{\rho}_{cc} - \gamma_{bc}\hat{\rho}_{cc} + \gamma_{bc}\hat{\rho}_{bb} \tag{2.40}$$

$$\dot{\hat{\rho}}_{ab} = -i\omega_{ab}\hat{\rho}_{ab} + i\Omega_1 e^{-i\nu_1 t}(\hat{\rho}_{bb} - \hat{\rho}_{aa}) + i\Omega_2 e^{-i\nu_2 t}\hat{\rho}_{cb} - \gamma\hat{\rho}_{ab} \tag{2.41}$$

$$\dot{\hat{\rho}}_{ac} = -i\omega_{ac}\hat{\rho}_{ac} + i\Omega_2 e^{-i\nu_2 t}(\hat{\rho}_{cc} - \hat{\rho}_{aa}) + i\Omega_1 e^{-i\nu_1 t}\hat{\rho}_{bc} - \gamma\hat{\rho}_{ac} \tag{2.42}$$

$$\dot{\hat{\rho}}_{cb} = -i\omega_{cb}\hat{\rho}_{cb} + i\Omega_2^* e^{i\nu_2 t}\hat{\rho}_{ab} - i\Omega_1 e^{-i\nu_1 t}\hat{\rho}_{ca} - \gamma_{bc}\hat{\rho}_{cb} \tag{2.43}$$

where $\omega_{ab} = \omega_a - \omega_b$, $\omega_{ac} = \omega_a - \omega_c$ and $\omega_{cb} = \omega_c - \omega_b$.

We can write the density operator in the form of slowly varying amplitude such that the matrix elements satisfy

$$\hat{\rho}_{aa} = \rho_{aa} \tag{2.44}$$

$$\hat{\rho}_{bb} = \rho_{bb} \tag{2.45}$$

$$\hat{\rho}_{cc} = \rho_{cc} \tag{2.46}$$

$$\hat{\rho}_{ab} = \rho_{ab} e^{-i\nu_1 t} \tag{2.47}$$

$$\hat{\rho}_{ac} = \rho_{ac} e^{-i\nu_2 t} \tag{2.48}$$

$$\hat{\rho}_{bc} = \rho_{bc} e^{-i(\nu_1 - \nu_2)t}. \tag{2.49}$$

Substituting these into equations ($2.38 \sim 2.43$), they turn into the following equations

$$\dot{\rho}_{aa} = i\Omega_1\rho_{ba} - i\Omega_1^*\rho_{ab} + i\Omega_2\rho_{ca} - i\Omega_2^*\rho_{ac} - 2\gamma\rho_{aa} \tag{2.50}$$

$$\dot{\rho}_{bb} = i\Omega_1^*\rho_{ab} - i\Omega_1\rho_{ba} + \gamma\rho_{aa} - \gamma_{bc}\rho_{bb} + \gamma_{bc}\rho_{cc} \tag{2.51}$$

$$\dot{\rho}_{cc} = i\Omega_2^*\rho_{ac} - i\Omega_2\rho_{ca} + \gamma\rho_{aa} - \gamma_{bc}\rho_{cc} + \gamma_{bc}\rho_{bb} \tag{2.52}$$

$$\dot{\rho}_{ab} = -\Gamma_{ab}\rho_{ab} + i\Omega_1(\rho_{bb} - \rho_{aa}) + i\Omega_2\rho_{cb} \tag{2.53}$$

$$\dot{\rho}_{ac} = -\Gamma_{ac}\rho_{ac} + i\Omega_2(\rho_{cc} - \rho_{aa}) + i\Omega_1\hat{\rho}_{bc} \tag{2.54}$$

$$\dot{\rho}_{cb} = -\Gamma_{cb}\rho_{cb} + i\Omega_2^*\rho_{ab} - i\Omega_1\rho_{ca} \tag{2.55}$$

where $\Gamma_{ab} = \gamma + i(\omega_{ab} - \nu_1)$, $\Gamma_{ac} = \gamma + i(\omega_{ac} - \nu_2)$ and $\Gamma_{cb} = \gamma_{bc} + i(\omega_{cb} + \nu_2 - \nu_1)$. Known initial conditions, we are able to solve these equations for the matrix elements of the density operator. As an example, we solve for ρ_{ab} which describes the optical properties of the transition $|a\rangle \rightarrow |b\rangle$. For the steady state in which $\rho_{ij} = 0$, we obtain the solution

$$\rho_{ab} = i\Omega_1 \frac{(\rho_{bb} - \rho_{aa})(\Gamma_{ac}^*\Gamma_{cb} + |\Omega_1|^2) + |\Omega_2|^2(\rho_{aa} - \rho_{cc})}{\Gamma_{ab}\Gamma_{ac}^*\Gamma_{cb} + \Gamma_{ac}^*|\Omega_2|^2 + \Gamma_{ab}|\Omega_1|^2}. \tag{2.56}$$

In a practical case, the drive field is much stronger than the probe field, i.e. $|\Omega_2|^2 \gg |\Omega_1|^2$. The state $|a\rangle$ is most populated, i.e. $\rho_{bb} \approx 1$, $\rho_{aa} \approx 0$ and $\rho_{cc} \approx 0$. We then can write ρ_{ab} as the following

$$\rho_{ab} = \frac{i\Gamma_{cb}\Omega_1}{\Gamma_{ab}\Gamma_{cb} + |\Omega_2|^2}. \tag{2.57}$$

For an ensemble of atoms with the density N, the polarization is given by $P = N\wp_{ab}\rho_{ab}$ and we also have the relation $P = \varepsilon_0\chi_{ab}E$ where χ_{ab} is the susceptibility. Therefore, the susceptibility χ_{ab} can be expressed as $\chi_{ab} = \frac{N\wp_{ab}\rho_{ab}}{\varepsilon_0 E}$. Use equation (2.57), we have

$$\chi_{ab} = i\kappa \frac{i\Gamma_{cb}}{\Gamma_{ab}\Gamma_{cb} + |\Omega_2|^2}, \tag{2.58}$$

where $\kappa = 3N\lambda^2\gamma_r/8\pi^2$. If the drive field is on resonant ($\nu_2 = \omega_{ac}$) and the probe field is not, the single photon detuning is defined by $\Delta = \omega_{ab} - \nu_1$. The dependence of the susceptibility χ on the detuning Δ is shown in Fig. 3. The parameters used in the plots are $\Omega_1 = 0.1\gamma$, $\Omega_2 = \gamma$ and $\gamma_{bc} = 0.01\gamma$. Plot (a) is the imaginary part of χ which represents the absorption of the medium. Plot (b) is the real part of χ which represents the index of refraction. Unlike what one would expect for a two level system, at the resonance ($\Delta = 0$), the absorption approaches zero and the medium is transparent to the resonant probe field. This phenomenon is called Electromagnetically Induced Transparency (EIT). Besides the transparency, the associated abnormal dispersion near resonance is more interesting. It is attributed to many effects which will be described in the rest of the dissertation.

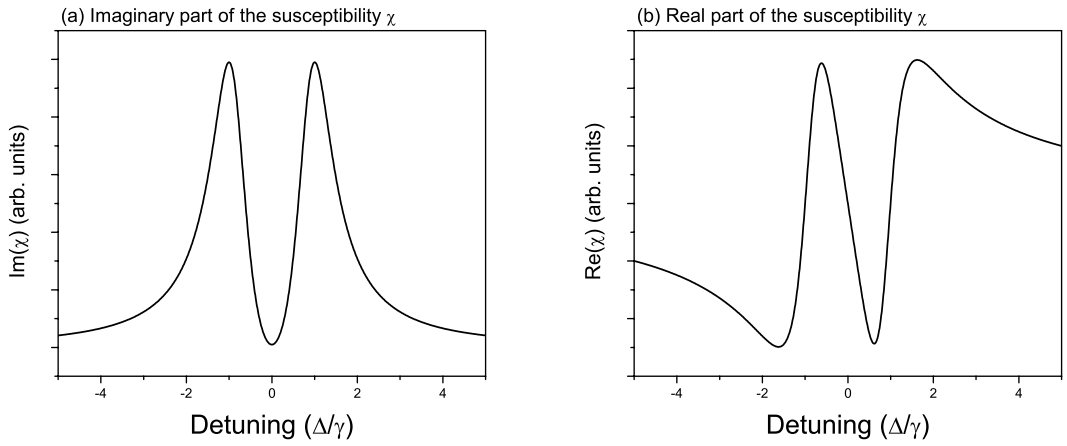

Fig. 3. Susceptibility χ_{ab} dependence on the detuning Δ. Both the imaginary part (a) and the real part (b) of the susceptibility are shown. The parameters are $\Omega_1 = 0.1\gamma$, $\Omega_2 = \gamma$ and $\gamma_{bc} = 0.01\gamma$.

To consider two laser fields propagating in an ensemble of three level atoms, the expression of ρ_{ab} such as (2.56) can be used in the propagation equation (2.35). The properties of the probe field are given by the solution of this equation.

CHAPTER III

PHASE EFFECTS IN EIT

As described in Chapter II, one can have Electromagnetically Induced Transparency when two laser fields coherently interacts with a three level system. Under EIT conditions, the medium has an unusual transparency at resonance frequency and an associated abnormal dispersion which are contributed by quantum coherence [1, 3, 2, 15, 16]. Besides these properties, the quantum coherence in EIT leads to many other counter-intuitive phenomena such as slow and stored light in various media [8, 9, 17, 18, 19, 10, 20], the scattering via a gradient force in gases [21], the forward Brillouin scattering in ultra-dispersive resonant media [11, 12, 22], controlled coherent multi-wave mixing [13], Doppler broadening elimination [23], light induced chirality in a nonchiral medium [7], switching faster than relaxation rate [24], a new class of entanglement amplifier [25] based on correlated spontaneous emission lasers [26, 27, 28, 29]. Because of the importance of EIT to both understanding the fundamental physics and the novel applications, EIT and related effects have been extensively studied throughout the years. In this chapter, we discuss how the phase of electromagnetical fields affects and controls EIT.

Usually EIT can be realized in atoms that have a three level configuration such as Λ, V, and Ladder schemes [1, 3]. Natural generalizations of the three level schemes are the double-Λ, double-V, double-Ladder and Λ-V schemes [30, 31, 32, 33, 34, 35] in which two additional laser fields are used to have extra control of the coherence of two states (for example, two ground states for the Λ scheme). Although the easiest way to control the coherence is to apply one field to the transition between two ground states, it is not allowed for a closed loop consisting of three transitions which are all dipole transitions. Such a closed loop is possible if one of the transitions is a magnetic

dipole transition which can be driven by a microwave field. The optical properties such as absorption and dispersion of a coherently prepared medium can be modified by applying an additional microwave [33, 36, 37] or optical fields [34, 38]. In some regard, the generalized scheme mentioned above can be related to a three level system coupled with two optical fields and a microwave field. In both the standard three level systems and the generalized systems, the phase of the fields is crucial to determine the optical response of the medium. We are interested in how the phase of both the optical fields and microwave field affects the optical properties of the medium.

In the first section, we study the time response of EIT in a standard Λ scheme to a rapid variation of the phase of the optical field. In the experiment, we observed a very fast growth of the absorption when the phase of the optical field was abruptly changed, followed by a slow return to the level of steady-state absorption. The magnitude of the variation in absorption is proportional to the magnitude of the phase variation. The recovery time decreases with increasing optical power and the low power limit of the recovery time is determined by the ground state relaxation time. The technique can be used to control the absorption in EIT. It can also be used as a technique to measure the ground state relaxation rate.

In the second section, we study a closed Λ system in which two laser fields interacting with a three level system (rubidium atoms) and an additional microwave field is coupled to two ground state hyperfine levels. It is found that the relative phase of the microwave field to optical fields can affect the transmission in EIT. The additional microwave field provide a way to control the coherence of the system. It is a way to efficiently control EIT and optical properties of the medium.

A. Coherent control of EIT by the optical phase *

The basic EIT system we study is a Λ scheme atomic system coupled with two stationary optical fields Ω_d (drive) and Ω_p (probe) as shown in Fig. 4. In the steady state, the phase of optical fields and the phase of the coherence are locked. The medium has the transparency and the abnormal dispersion as described before. One way to understand EIT is to use the concept of dark state. The Λ system is equivalent to the system shown on the right side of Fig. 4, where two eigenstates $|B\rangle$ and $|D\rangle$ are given by

$$|B\rangle = \sin\theta|b\rangle + \cos\theta|c\rangle \tag{3.1}$$

$$|D\rangle = \sin\theta|b\rangle - \cos\theta|c\rangle \tag{3.2}$$

with $\tan\theta = \Omega_d(\phi_d)/\Omega_p(\phi_p)$. The state $|D\rangle$ has zero eigenvalue, so it has no coupling with the laser field and it is called dark state. In the steady state, most of atoms are trapped in the dark state so that the medium becomes transparent.

We can see from equation (3.2) that the dark state depends on the Rabi frequencies of optical fields which are phase dependent. We have to keep a stable phase relation to maintain a stationary dark state. A fast variation in phase of one optical field will break the phase relation and destroy the dark state. This process has been theoretically studied in [39], in which the simulation shows a fast variation in the absorption as a result of a fast variation of optical phase.

In this section, we report the experimental study on the effect of a fast variation of optical phase in EIT. We are interested in the dynamic processes of establishing

*Part of the data reported in this section is reprinted with permission from "*Dynamic control of EIT by changing optical phase,*" by V.A. Sautenkov, H. Li *et al.*, J. Mod. Opt. **55**, 3093 (2008) and "*Using phase dynamics in EIT to probe ground state relaxation in rubidium vapor,*" by V.A. Sautenkov, H. Li *et al.*, J. Mod. Opt. **56**, 975 (2009), Copyright by Taylor & Francis Group.

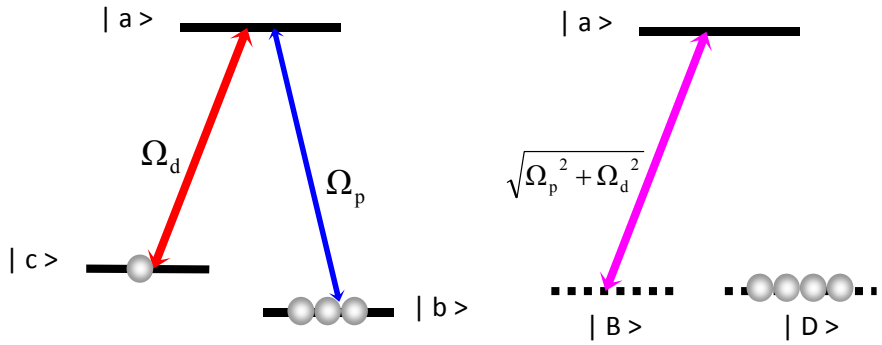

Fig. 4. A standard Λ scheme EIT system (left side) including a three level system and two laser fields. The system is equivalent to the system (right side) with two eigenstates bright state $|B\rangle$ and dark state $|D\rangle$.

and destroying EIT instead of the steady state EIT. The time scales of destroying and recovering the transparency is studied. Based on the experimental results, the potential applications such as control of EIT and probing the ground state relaxation rate will also be discussed.

1. Experimental setup

The experimental setup is shown in Fig. 5. An extended-cavity diode laser (ECDL) is tuned to the maximum absorption resonance which is a combination of two Doppler broadened optical transitions $5S_{1/2}(F=3) \leftrightarrow 5P_{1/2}(F=2)$ and $5S_{1/2}(F=3) \leftrightarrow 5P_{1/2}(F=3)$ of ^{85}Rb (D_1 line, $\lambda = 795$ nm). The linearly polarized laser beam is split and a $\lambda/2$ wave plate rotates the linear polarization of one beam. An electro-optical modulator (EOM) is installed in the path of one of the beams to change the relative optical phase. The orthogonally linearly polarized beams are combined by a polarizing beam splitter (PBS). After a $\lambda/4$ wave plate the laser beams are sent into a glass cell (the length is 7.5 cm) with rubidium atomic vapor. The ^{85}Rb atomic density is estimated as 2×10^{11} cm^{-3} from the cell temperature. To reduce the contribution of the stray magnetic

field the cell is installed in a magnetic shield. Two circularly polarized optical fields create a coherent coupling between ground state Zeeman sublevels in rubidium atomic vapor and generate EIT. The transmitted optical beams with orthogonal polarizations are separated using a second $\lambda/4$ wave plate and PBS. After the second PBS the optical beams are sent to photodiodes PD1 and PD2. The signals from photodiodes (bandwidth 0∼50 MHz) are recorded by a digital storage oscilloscope (DSO) with the bandwidth of 0∼100 MHz.

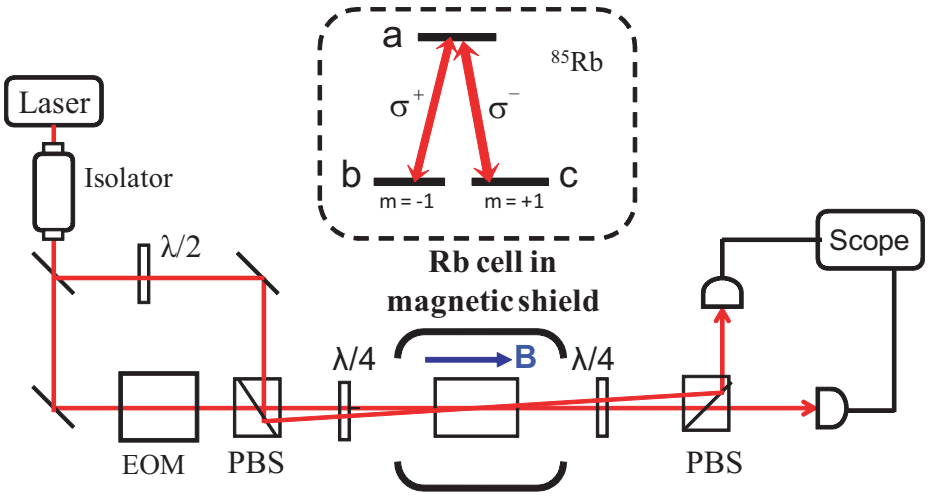

Fig. 5. Experimental setup and simplified energy level scheme in the inset. EOM, electro-optical modulator; PBS, polarizing beam splitter; $\lambda/2$ and $\lambda/4$, wave plates; PD1 and PD2, photo-detectors; DSO, digital storage oscilloscope.

In practice the beams with orthogonal polarizations can be aligned to be near perfectly overlapped [40] or crossing with a small angle [41] in the Rb cell. There are both advantages and down sides for each case. In the first case, the coherent region where two beams are overlapped is limited by the crossing angle, thus the time of flight for atoms is not well defined by the geometry of beams. However, the beams will be well separated for the detection because of the non-parallelism of the beams. In the later case, the coherent region is maximized to the beam size and the time

of flight can be estimated by the beam diameter. While in the detection stage, the separation of beams is limited by the extinction ratio of the polarizing beam splitter. We have studied the response of EIT to phase change in both cases.

In this experiment, the frequency of the laser field is fixed and the detuning is introduced by changing the separation of energy levels. As shown in Fig. 5, the ground states are two Zeeman sublevels. The splitting can be controlled by applying a longitudinal magnetic field B. Varying the two-photon detuning by the magnetic field, we can record the EIT resonance in transmission. A typical EIT transmission peak is shown in Fig. 6. The experimental EIT peak has a perfect Lorentzian fit.

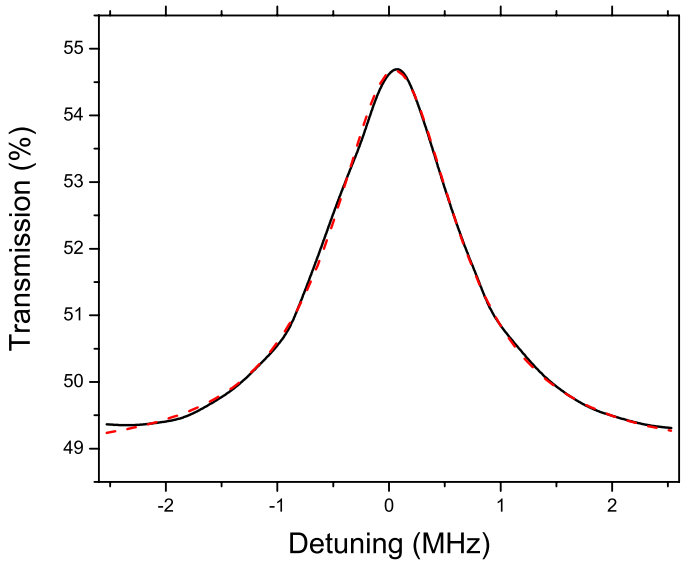

Fig. 6. The EIT resonance in transmission. The experimental result (solid curve) and the Lorentzian fit (red dot curve) versus the two-photon detuning are shown.

Changing the phase of the optical field is realized by an electro-optical modulator (EOM) inserted in the path of the beam. We apply low voltage rectangular pulses

with a repetition rate of 100 kHz to the EOM (bandwidth 0∼200 MHz) directly from a function generator. The rise time of pulses is about 20 ns and the edge of pulses can be considered as a step function in our experiment. We have adjusted the beam polarization and the position of the EOM to avoid intensity modulation at the photo detector PD1. The measured residual intensity modulation is less than the noise level in our experiment. We record the transmission of the coupled optical beam by the photo detector PD2.

2. Experimental results and discussion

As shown in Fig. 7, as we change the phase like curve (a), a general response of the transmission is represented by the curve (b). We observe a fast drop of the transmission when the optical phase is abruptly changed, followed by a slow return to the steady state transmission. The magnitude of the variation in transmission is dependent on the magnitude of the variation of the optical phase. It is illustrated in the right plot of Fig. 7.

The temporal response of transmission can be analyzed by using the theoretical model developed in [39]. A simplified energy level scheme is shown in Fig. 5. We suppose that optical transitions $a \rightarrow b$ and $a \rightarrow c$ are homogeneously broadened with spectral width γ_a. In the experiment the Rabi frequencies of the fields with orthogonal circular polarizations are equal, $\Omega_- = \Omega_+ = \Omega$ and $\Omega^2/\gamma_a > \gamma_{bc}$, where γ_{bc} is relaxation rate of the ground state coherence ρ_{bc}. Under these conditions when the variation of EIT is small (the optical phase Φ and the ground state coherence ρ_{bc} have small variations, $|\Delta\Phi| \ll \pi$, $|\Delta\rho_{bc}| \ll |\rho_{bc}|$) the master equations in [39] can be simplified by using the perturbation theory. A slow return of the ground state

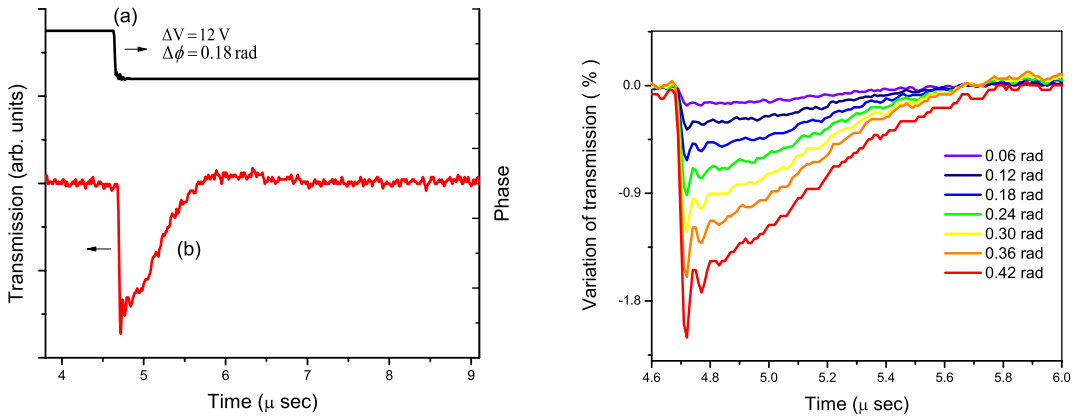

Fig. 7. The left figure shows the change of the EIT transmission (b) as the phase of optical field (a) changes abruptly. The transmission decreases and slowly recovers to the steady state level. The right figure shows the variation of transmission for different variations of the phase.

coherence variation to zero can be described by the exponential function,

$$|\Delta\rho_{bc}| \sim \exp(-2\gamma_{bc} - \frac{\Omega^2}{\gamma_a}) \tag{3.3}$$

For estimation the spectral width γ_a can be substituted by the Doppler width Δ_D. The expression of the recovery rate is similar to the ground state decoherence rate in a Λ system discussed in [42]. We shall note that a simple expression for the temporal response is valid only for the selected parameters. In a general case the time response of EIT could be more complicated.

We have performed measurements with the selected experimental parameters in order to satisfy the simplified theoretical model. The power of each optical beam is $P = 0.45$ mW and the phase change is $\Delta\Phi = 0.18$ rad. A detailed time dependence of the transmission is shown in Fig. 8. As we change the phase, there is a very sharp increase in the absorption followed by a slow return back to the steady-state

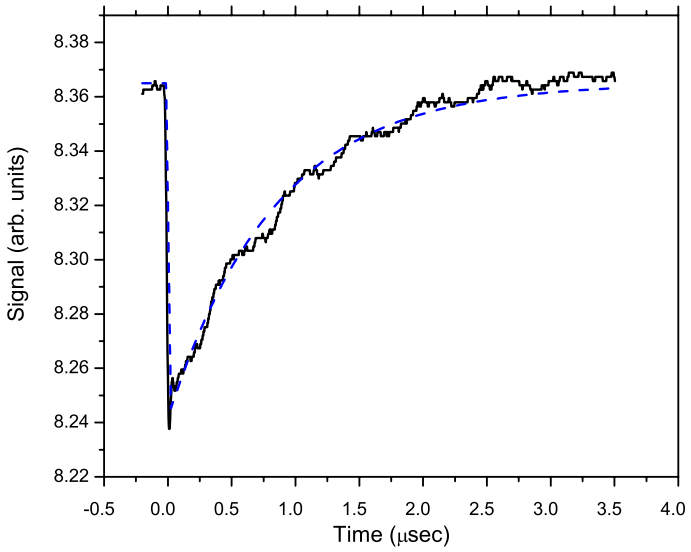

Fig. 8. The time dependence of transmission as the phase of optical field is changed abruptly. The solid line is the experimental result and the blue dash line is the exponential fit. The measurements are taken with overlapped beams.

transparency value.

The experiments have been done with both overlapped beams and crossing beams. For the case with overlapped beams, we estimate the rise time of the absorption between the 10% and 90% points to be on the order of 20 ns. We attribute this time to the response time of the electronic devices in our setup. The optical switch time could be much shorter [39]. Then the transmission restores slowly to the stationary value. The curve can be fit by a single exponential function, which we also plot in Fig. 8 as the dash line. The recovery time T at the optical power $P = 0.45$ mW of each beam is estimated by a least squares fit to be 0.84 μs. The variation of the transmission is estimated as 0.5%. This value is much less than the amplitude of the EIT resonance of 8%. For the case with crossing beams, the rise

time of the absorption between the 10% and 90% points is also on the order of 20 ns. The recovery time T is estimated to be 0.58 μs. The variation of the transmission is about 0.5%.

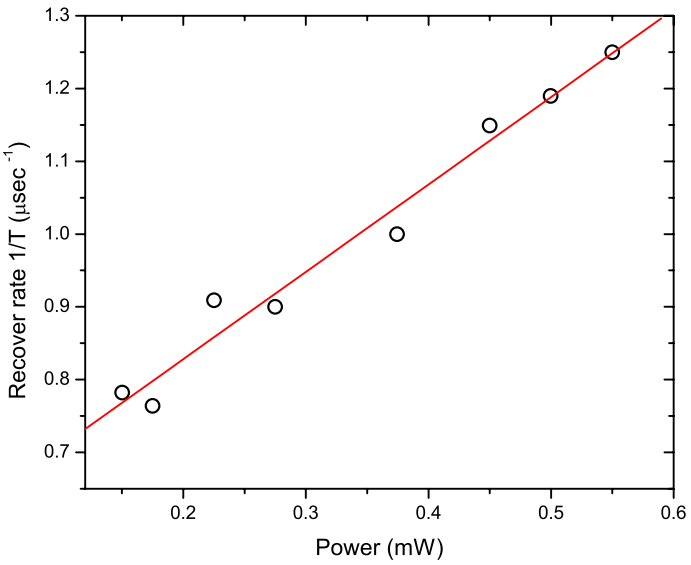

Fig. 9. The power dependence of the recovery rate $1/T$. The circles are the experimental data and the red line is the linear fit.

We have also measured the power dependence of the optical response. Keep the phase modulation and other parameters same as those used in Fig. 8, we did the measurements at different optical powers. The recovery time T is estimated for different optical powers from the least squares fit. The power dependence of the inverse recovery time $1/T$ (recovery rate) for the case with overlapped beams is presented in Fig. 9. We fit the experimental data in Fig. 9 by a linear function $y = A + B \cdot P$. The linear fit gives $A = 0.59\ \mu\text{s}^{-1}$ and $B = 1.2\ \text{mW}^{-1}\mu\text{s}^{-1}$. The low power limit of the recovery rate should coincide with the inverse effective ground state relaxation time according to equation (3.3). The estimated ground state relaxation

time is $T_0 = A^{-1} = 1.7 \pm 0.009$ μs. This value should be the same as the time of flight which can be calculated for the optical beam with a Gaussian distribution by using the expression $T_\nu = d/\nu_{th}$, where d is the beam diameter and ν_{th} is the thermal velocity of the rubidium atoms [43]. Based on the optical beam profile in the rubidium cell recorded by a CCD camera, we can make a rough estimation of the time of flight as order of 2 μs.

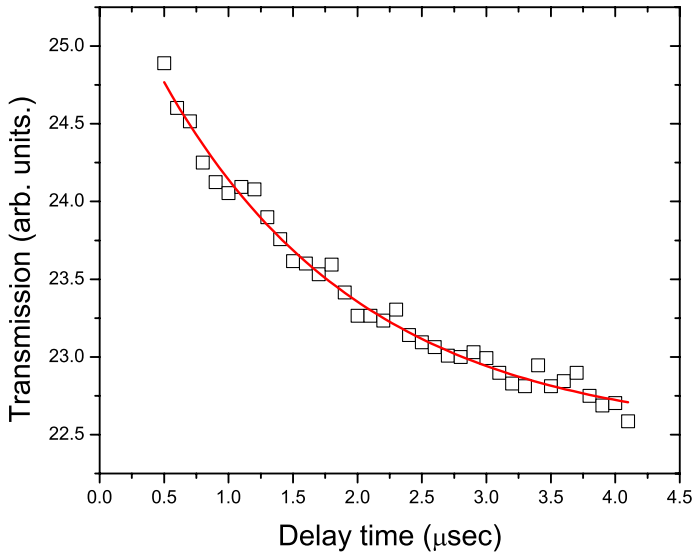

Fig. 10. The power dependence of the recovery rate $1/T$. The squares are the experimental data and the red line is the linear fit.

A direct measurement of the time of flight can be done by using the technique "relaxation in the dark" [44, 45]. In this method the pump pulse optically pumps the ground state sublevels to populate one of them. A following time-delayed pulse probes the population of the other sublevels. Changing the delay time between the pump and probe pulses, the dependence of probe pulse transmission on the delay time tells us the relaxation time of the ground state sublevels. In our experiment only one

laser beams is used to measure the relaxation time. The decay curve at low pump and probe powers is shown in Fig. 10. The measured decay time is 1.56 ± 0.12 μs. We can see that the relaxation time measured by "relaxation in the dark" is consistent with the value estimated by the power dependence of the EIT recovery rate considering the uncertainty of both measurements. The technique of using the phase dynamics in EIT can be an alternative method to measure the relaxation time or the time of flight.

B. Coherent control of EIT by a microwave field *

The system under study is a three level atomic system coupled with two optical fields and an additional microwave field forming so called "closed Λ scheme", as shown in Fig. 11. The EIT of the system is studied with the presence of the microwave field. We find that the microwave field "perturbs" the coherence of two ground states and leads to the change of the maximum transmission of the probe field. Both the enhanced or suppressed EIT peaks can be obtained depending on the relative phase between the optical fields and the microwave field.

The systems involving interactions of both optical fields and microwave fields have been of great interests. The closed Λ scheme with a microwave field coupled with two ground state hyperfine levels has been theoretically studied [46]. Experimentally, it has been shown the perturbation of microwave fields to EIT in both three [47] and four [48] level systems. The microwave field has been used to excite a Raman trapped state to study the influence of the microwave field on the CPT in a Λ system [49], it has also been used to realize four-wave mixing (FWM) with optical and microwave

*Part of the data reported in this section is reprinted with permission from "*Electromagnetically induced transparency controlled by a microwave field*," by H. Li *et al.*, Phys. Rev. A **80**, 023820 (2009), Copyright by the American Physical Society.

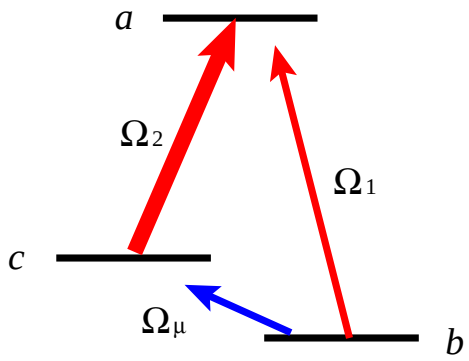

Fig. 11. Energy levels of a closed Λ scheme three-level system. Ω_1 and Ω_2 are two optical fields and Ω_μ is a microwave field.

fields [50] and to study double dark resonances [37]. Particularly, the control of the probe transmission by the microwave phase has been demonstrated [36] in a V scheme system of Pr^{3+}:$YAlO_3$ excited by a microwave field and two optical fields.

Owing to the additional control of coherence by the microwave field, the close Λ system has broad range of potential applications. For example, it has been considered as the perspective candidate for realization of stop-and-go slow light [51, 52, 53] and coherent backward scattering [13]. The interest in this topic is also stimulated by the quantum storage based on EIT [54, 55, 56]. It has been shown that the quantum state of light can be stored and retrieved in a dense medium by switching on and off a control field. The systems with a microwave field as the control field have better controlled probe transparency because the absorption of the microwave is much smaller than optical fields. This is important for improving and optimizing the quantum storage efficiency [57, 58, 59, 60, 61]. The microwave can also improve the performance of optical delay lines using slow light [62].

The rest of this section is organized by starting with a simple theoretical model of a close Λ system. It is followed by the experimental details as well as the experimental results and discussions. A numerical simulation is presented at the end.

1. Theory of a closed Λ system

Let us consider a cell filled with a gas of three-level atoms that have the energy level scheme shown in Fig. 11. Two optical beams are propagating through the cell of atoms along z axis, and the optical fields

$$E_1 = \mathcal{E}_1 \cos(\nu_1 t - k_1 z + \phi_1)$$

and

$$E_2 = \mathcal{E}_2 \cos(\nu_2 t - k_2 z + \phi_2)$$

are coupled to the atomic transitions $|a\rangle \rightarrow |b\rangle$ and $|a\rangle \rightarrow |c\rangle$ (see Fig. 11) correspondingly, where ν_1 and ν_2 are the optical frequencies of the corresponding fields; k_1 and k_2 are the wave numbers of the optical fields; ϕ_1 and ϕ_2 are the phases of the optical fields. The cell is placed in a microwave cavity and a microwave field

$$E_\mu = \mathcal{E}_\mu(z) \cos(\nu_\mu t + \phi_\mu)$$

is coupled to two ground states $|b\rangle$ and $|c\rangle$. Here $\mathcal{E}_\mu(z)$ is the dependence of the microwave field on position z inside the cavity, ν_μ is the microwave frequency, and ϕ_μ is the phase of the microwave field.

The Hamiltonian of the atom located at position z can be written as

$$\begin{aligned} H &= \hbar\omega_a|a\rangle\langle a| + \hbar\omega_b|b\rangle\langle b| + \hbar\omega_c|c\rangle\langle c| - [\wp_{ab}E_1|a\rangle\langle b| + \\ &\quad \wp_{ac}E_2|a\rangle\langle c| + \wp_{bc}E_\mu|c\rangle\langle b| + h.c.], \end{aligned} \tag{3.4}$$

where $\hbar\omega_\alpha$ is the energy of the corresponding level $|\alpha\rangle$, and $\wp_{\alpha,\beta} = \langle\alpha|\hat{\wp}|\beta\rangle$ are the dipole moments of corresponding transitions $|\alpha\rangle \rightarrow |\beta\rangle$ $(\alpha, \beta = a, b, c)$. Use the

density matrix equation of motion (2.17),

$$\dot{\rho} = -\frac{i}{\hbar}[H,\rho] - \frac{1}{2}\{\Gamma,\rho\} \tag{3.5}$$

The non-diagonal elements of the density matrix equations are found as the following,

$$\dot{\rho}_{ab} = -(\gamma_{ab}+i\omega_{ab})\rho_{ab} - i\frac{\wp_{ab}E_1}{\hbar}(\rho_{aa}-\rho_{bb}) + i\frac{\wp_{ac}E_2}{\hbar}\rho_{cb} - i\frac{\wp_{cb}E_\mu}{\hbar}\rho_{ac} \tag{3.6}$$

$$\dot{\rho}_{ac} = -(\gamma_{ac}+i\omega_{ac})\rho_{ac} - i\frac{\wp_{ac}E_2}{\hbar}(\rho_{aa}-\rho_{cc}) + i\wp_{ab}E_1\rho_{bc} - i\frac{\wp_{bc}E_\mu}{\hbar}\rho_{ab} \tag{3.7}$$

$$\dot{\rho}_{cb} = -(\gamma_{cb}+i\omega_{cb})\rho_{cb} - i\frac{\wp_{cb}E_\mu}{\hbar}(\rho_{cc}-\rho_{bb}) + i\frac{\wp_{ca}E_2}{\hbar}\rho_{ab} - i\frac{\wp_{ab}E_1\rho_{ca}}{\hbar} \tag{3.8}$$

where $\omega_{\alpha\beta} = \omega_\alpha - \omega_\beta$.

We make the rotating wave approximation by leaving only the resonance terms and neglecting the counter-rotating far-off resonance terms. Introducing slowly varying envelopes

$$\rho_{ab} = \sigma_{ab}\exp(ik_1z - i\nu_1t), \tag{3.9}$$

$$\rho_{ac} = \sigma_{ac}\exp(ik_2z - i\nu_2t), \tag{3.10}$$

$$\rho_{cb} = \sigma_{cb}\exp(i\Delta kz - i(\nu_1-\nu_2)t), \tag{3.11}$$

$$\rho_{\alpha\alpha} = \sigma_{\alpha\alpha}, \tag{3.12}$$

where $\Delta k = k_1 - k_2$, then the density matrix equations can be written as

$$\dot{\sigma}_{ab} = -\Gamma_{ab}\sigma_{ab} - i\Omega_1(\sigma_{aa}-\sigma_{bb}) + i\Omega_2\sigma_{cb} - i\Omega_\mu e^{i(\nu_1-\nu_2-\nu_\mu)t+i\Delta kz}\sigma_{ac} \tag{3.13}$$

$$\dot{\sigma}_{ac} = -\Gamma_{ac}\sigma_{ac} - i\Omega_2(\sigma_{aa}-\sigma_{cc}) + i\Omega_1\sigma_{bc} - i\Omega_\mu^* e^{-i(\nu_1-\nu_2-\nu_\mu)t-i\Delta kz}\sigma_{ab} \tag{3.14}$$

$$\dot{\sigma}_{cb} = -\Gamma_{cb}\sigma_{cb} - i\Omega_\mu e^{i(\nu_1-\nu_2-\nu_\mu)t+i\Delta kz}(\sigma_{cc}-\sigma_{bb}) + i\Omega_2^*\sigma_{ab} - i\Omega_1\sigma_{ca} \tag{3.15}$$

where

$$\Omega_1 = \frac{\wp_{ab}\mathcal{E}_1}{2\hbar}e^{i\phi_1},\ \ \Omega_2 = \frac{\wp_{ac}\mathcal{E}_2}{2\hbar}e^{i\phi_2},\ \text{and}\ \Omega_\mu = \frac{\wp_{bc}\mathcal{E}_\mu}{2\hbar}e^{i\phi_\mu}$$

are the Rabi frequencies of the optical probe and drive fields, and the microwave field respectively; $\Gamma_{ab} = \gamma_{ab} + i(\omega_{ab} - \nu_1)$, $\Gamma_{ac} = \gamma_{ac} + i(\omega_{ac} - \nu_2)$ and $\Gamma_{cb} = \gamma_{cb} + i(\omega_{cb} + \nu_2 - \nu_1)$. We consider the case in which the drive field is on resonant ($\nu_2 = \omega_{ac}$), while the probe field and microwave field have the same detuning $\Delta \equiv \omega_{ab} - \nu_1 = \omega_{cb} - \nu_\mu$, thus $\nu_1 - \nu_2 - \nu_\mu = 0$. Consider the steady-state regime ($\dot{\rho}_{ab} = \dot{\rho}_{ab} = \dot{\rho}_{cb} = 0$), and assume that the drive field is much stronger than the probe field and the microwave field ($|\Omega_2| \gg |\Omega_1|, |\Omega_\mu|$), so all of the population is in the ground state $|b\rangle$, i.e. $\rho_{bb} \simeq 1$ and $\rho_{aa} = \rho_{cc} \simeq 0$, we can solve Eqs. (6-8) for σ_{ab},

$$\sigma_{ab} = \frac{i\Gamma_{cb}\Omega_1}{\Gamma_{ab}\Gamma_{cb} + |\Omega_2|^2} - \frac{\Omega_2\Omega_\mu e^{i\Delta kz}}{\Gamma_{ab}\Gamma_{cb} + |\Omega_2|^2} \tag{3.16}$$

with $\Gamma_{ab} = \gamma_{ab} + i\Delta$ and $\Gamma_{cb} = \gamma_{cb} + i\Delta$.

Plug the expression of σ_{ab} into equation (2.35), we obtain the propagation equation

$$\frac{\partial\Omega_1}{\partial z} = -\frac{\eta\Gamma_{cb}\Omega_1}{\Gamma_{ab}\Gamma_{cb} + |\Omega_2|^2} - i\frac{\eta\Omega_2\Omega_\mu e^{i\Delta kz}}{\Gamma_{ab}\Gamma_{cb} + |\Omega_2|^2} \tag{3.17}$$

On the right hand side of equation (3.17), the first term is due to the contribution from the Lambda scheme EIT, and the second term is the contribution from the parameteric process involves the microwave field. The transmission of the probe field is determined by the interference of these two terms. The second term is interesting because of the strong dependence on the relative phase of the optical fields and the microwave field. This gives us several ways to control the coherence and the transmission of the probe field. For instance, one can use a microwave phase shifter to change the phase of microwave field; one can also use an optical delay line, like the one used in [49], to change the phase of optical field. An alternative way is simply changing the position of the Rb cell, which is described as the following.

Assume that the drive and probe fields are phase-locked, they form a wave pack-

age along the propagation direction with the frequency which is the frequency difference of two fields. For ^{87}Rb, this frequency is 6.835 GHz, and the corresponding wavelength is about 4.4 cm. If we put the Rb cell in a microwave cavity which is excited by a microwave with the frequency of 6.835 GHz, the phase of microwave field in the cavity does not change when we move the cell and the microwave cavity together. However, the relative optical phase changes since the relative position of the cell with respect to the wave package of optical fields changes. In other words, we are able to change the phase $\triangle kz$ by moving the cell and the microwave cavity along the propagation direction of the optical fields.

2. Experimental setup

The experimental setup is schematically shown in Fig. 12. The ^{87}Rb gas along with 5 Torr of Neon buffer gas is confined in a glass cell with the length of 25 mm. To efficiently couple the microwave field with Rb atoms, the Rb cell is installed in a microwave cavity. The microwave cavity with the cell is installed in a magnetic shield to isolate the cell from environmental magnetic fields in the laboratory, and the residue magnetic field is negligible. The Zeeman sublevels are not resolved in our experiment. A non-magnetic heater is used to heat the cell to reach the atomic density of 10^{12} cm^{-3}. The microwave cavity has the resonant frequency of 6.835 GHz. The loaded quality factor Q is about 2000, and the cavity mode is TE_{011}. A microwave signal generator provides the 6.835 GHz microwave field, which is amplified by a microwave amplifier and is then injected into the cavity through an antenna. The 6.835 GHz microwave field is coupled with two hyperfine ground states $5S_{1/2}(F = 1)$ and $5S_{1/2}(F = 2)$ of ^{87}Rb atoms.

The optical fields are provided by a diode laser which is tuned to the D_1 resonance line of ^{87}Rb atoms, specifically at the transition $5S_{1/2}(F = 2) \leftrightarrow 5P_{1/2}(F = 2)$. The

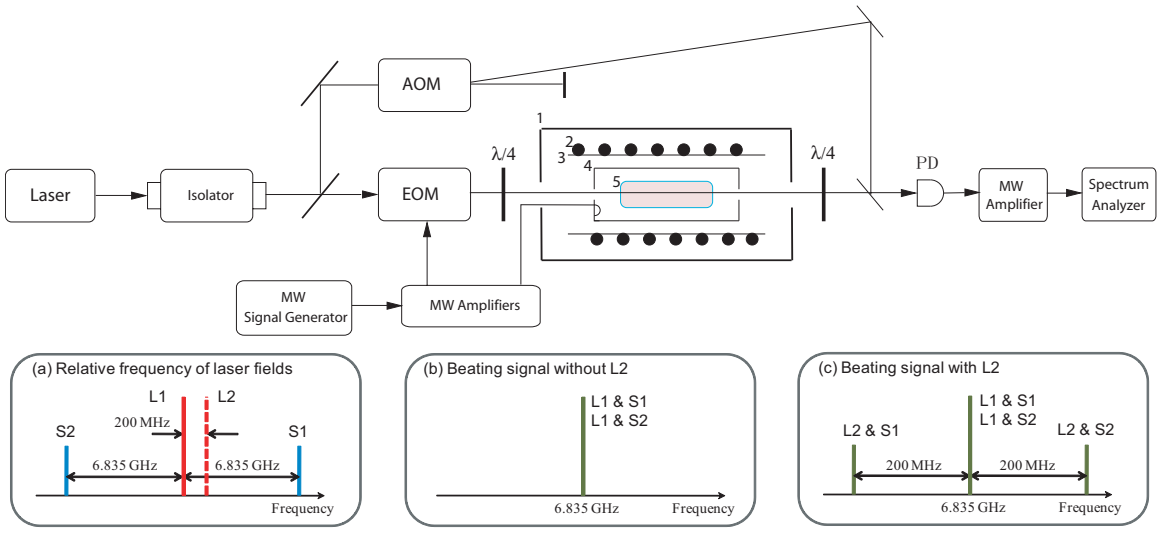

Fig. 12. Experimental setup. EOM - electro-optic modulator; AOM - acousto-optic modulator; PD - photodiode; the oven is assembled with 1. copper tube; 2. non-magnetic heater; 3. magnetic shield; 4. microwave cavity with antenna; 5. Rb cell. Inset (a) shows the relative frequency of the laser fields. L1 is the drive field, S1 and S2 are two sidebands generated by the EOM and S1 works as the probe field. L2 is the laser field shifted 200 MHz in frequency by the AOM. Inset (b) shows the beating signal without considering L2. Inset (c) shows the beating signals with all fields L1, L2, S1 and S2 considered.

laser beam is split into two beams by a beam splitter. One beam passes through an acousto-optic modulator (AOM) which shifts the laser frequency by 200 MHz. This beam with 200 MHz shift in frequency is denoted as L2 in Fig. 12(a). It will be used as a local oscillator of the heterodyne detection. The other beam is used to make the drive and probe fields. This beam passes through an electro-optic modulator (EOM) which is driven by a microwave field with the frequency of 6.835 GHz. Two sidebands are generated with the frequency separation of 6.835 GHz with respect to the original field. Two sidebands are denoted as S1 and S2 in Fig. 12(a). The original field works as the drive field. One sideband (S1) works as the probe field at the transition $5S_{1/2}(F = 1) \leftrightarrow 5P_{1/2}(F = 2)$. The intensity ratio of the probe field to the drive field

is about 15%. The other sideband (S2) is 6.835 GHz downshifted in frequency with respect to the drive field. It is far detuned from the resonance and it has negligible effect on the experiment. The laser beam from the EOM is circularly polarized by a quarter wave plate and it is directed into the Rb cell.

With the optical fields (drive and probe) coming out from the EOM and the microwave field in the cavity, we have a closed-Lambda system as shown in Fig. 11. Please note that the microwave signals used by the EOM and the microwave cavity come from the same microwave signal generator. During the experiment, the microwave generator is modulated 200 kHz in frequency around 6.835 GHz and the sweep period is 0.1 s. Therefore, the probe laser field and the microwave field are synchronized to scan 200 kHz in frequency, and they have the same detuning.

The transmitted probe field is detected by the heterodyne detection used in Ref [9]. Instead of a direct measurement of the transmitted intensity which contains the drive and two sidebands, we detect the beating signal using a fast photo detector with the bandwidth of 25 GHz. The signal from the photo detector is analyzed by a spectrum analyzer which is synchronized with the modulation of the microwave generator. As shown in Fig. 12(b), without the presence of the shifted drive beam L2, the detected beating signal is at 6.835 GHz. It includes the beating signal between L1 and S1, and the beating signal between L1 and S2. With the frequency shifted drive beam L2, it beats with the transmitted beam to separate the frequency components of S1 and S2 shown in Fig. 12(c). The beating signal between L2 and S2 is blue shifted by 200 MHz, and the beating signal between L2 and S1 is red shifted by 200 MHz. The transmission of the probe field is obtained by measuring the beating signal at the frequency of 6.835 GHz + 200 MHz.

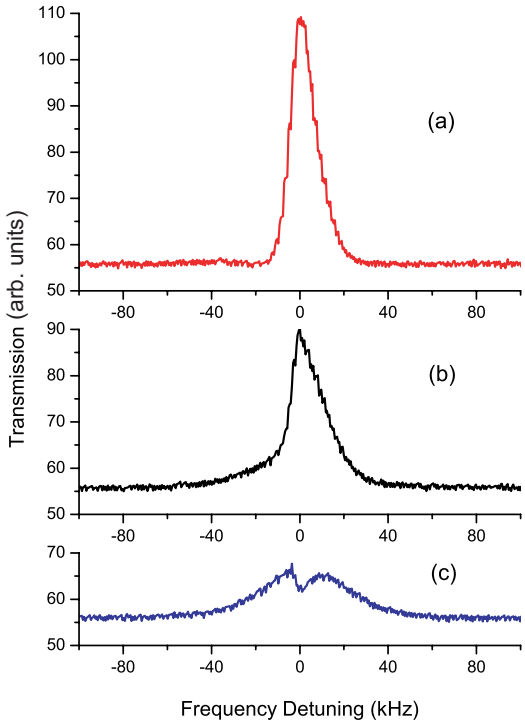

Fig. 13. The beating signal recorded by a spectrum analyzer at the center frequency of 7.035 GHz. It represents the transmission of the probe field. (a) the enhanced transmission with the microwave field applied; (b) the suppressed without the microwave field applied; (c) the destructive transmission with the microwave field applied. The positions of the cell where (a) and (c) were taken are about 2.2 cm apart.

3. Experimental results

We measure the transmission of the probe field as a function of the detuning and plot the transmission versus the detuning in Fig. 13. A normal EIT transmission peak without applying the microwave field is shown in Fig. 13(b). With the presence of the microwave field, we expect the ground state coherence is "disturbed" by the microwave field and it changes the transmission of the probe field. As discussed above, we change the relative phase between the optical fields and the microwave field by changing the position of the cell and the microwave cavity along the optical axis. The

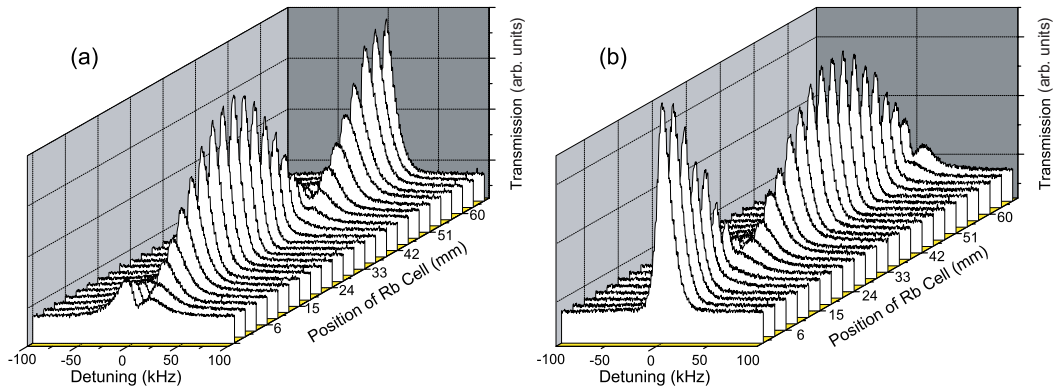

Fig. 14. The EIT peaks as we change the position of the cell along the propagation direction of optical fields. An EIT peak is recorded at every 3 mm we move the cell. Figures (a) and (b) correspond to the case where the input laser fields are right and left, respectively, circularly polarized. The distance between two maxima (or minima) next to each other is about 4.4 cm.

periodicity of the cell position influencing the probe field transmission is expected to be about 4.4 cm, the wavelength of the microwave field with the frequency of 6.835 GHz. Due to the interference of two terms on the right hand side of equation (3.16), the transmission of probe field could be either enhanced or suppressed depending on the relative phase. It is what we have observed in the experiment. As shown in Fig. 13, with applying the microwave field, we have obtained both enhanced (a) and suppressed (c) transmission of the probe field as we move the microwave cavity with the cell to change the relative phase between the optical fields and the microwave field. The positions of the cell corresponding to the curves (a) and (c) are at the distance of about 2.2 cm.

An interesting feature needs to be pointed out for the case of suppressed transmission (Fig. 13(c)). In this case, the amplitude of EIT peak decreases as we expected, and we also have a small dip on the top which indicates that one (the one due to presence of microwave field) of interfering terms has relatively narrower width. Its width is narrower than EIT width.

To systematically study the influence of the relative phase between the optical fields and the microwave field on the probe field transmission, the EIT transmission is recorded at different positions of the cell with a step of 3 mm along the propagation direction of the optical fields as shown in Fig. 14. The transmission has been obtained with different polarizations of optical fields. The results obtained with the right circularly polarized laser field are shown in Fig. 14(a), the results with the left circularly polarized laser field are shown in Fig. 14(b). The amplitude of EIT peak is oscillating with the change of the cell position. The distance between two maxima (or minima) next to each other is about 4.4 cm, which is exactly the wavelength of beating envelope of the input optical fields. This periodicity is consistent with the theoretical prediction described above.

The oscillation is shown in Fig. 15, where we plot the amplitude of EIT peaks as a function of the relative phase (phase 2π corresponds the wavelength 4.4 cm). The dash lines are fittings of the sinusoid function. Comparing the cases of right and left circularly polarized input laser fields, the behaviors are exactly opposite. This feature seems to be surprising, because the whole system is symmetrical about the optical axis and there is no obvious way to tell the difference between left and right circular polarizations. The physics of such behavior is the following. The left and right circularly polarized fields are coupled with different Zeeman sub-levels (see Fig. 16). Due to the optical pumping, among the Zeeman sub-levels of the ground state with $F = 1$, the state $|F = 1, m = +1\rangle$ is most populated for the right circularly polarized light and the state $|F = 1, m = -1\rangle$ is most populated for the left circularly polarized light. Then, we can see a simplified level scheme shown in Fig. 11 corresponding to the real Rb energy levels. For the right circularly polarized fields, we have $|a\rangle = |F' = 2, m = 2\rangle$, $|b\rangle = |F = 1, m = 1\rangle$, and $|c\rangle = |F = 2, m = 1\rangle$. For the left circularly polarized fields, we have $|a\rangle = |F' = 2, m = -2\rangle$, $|b\rangle = |F = 1, m = -1\rangle$, and

$|c\rangle = |F = 2, m = -1\rangle$. The magnetic transition dipole moments between hyperfine levels are equal to each other as

$$\langle 2, -m|\hat{\mu}_z|1, -m\rangle = \langle 2, m|\hat{\mu}_z|1, m\rangle, \tag{3.18}$$

while the relation between the dipole moments of optical transitions are the following

$$\langle 2', m+1|\wp_{+1}|2, m\rangle = -\langle 2', -m-1|\wp_{-1}|2, -m\rangle, \tag{3.19}$$

$$\langle 2', m+1|\wp_{+1}|2, m\rangle = \langle 2', -m-1|\wp_{-1}|1, -m\rangle, \tag{3.20}$$

where we use notations $|2', m\rangle = |F' = 2, m\rangle$ and $|2, m\rangle = |F = 2, m\rangle$. Consequently, for the simplified model (shown in Fig. 11), the Rabi frequencies for the right and left circularly polarized optical fields have the following relations

$$\Omega_1^r = \Omega_1^l, \quad \Omega_2^r = -\Omega_2^l, \tag{3.21}$$

where the indices r and l denote the Rabi frequencies of the right and left circularly polarized optical beams respectively. Thus, the corresponding change of the phase of the Rabi frequencies of the optical beams have opposite signs which introduce a phase difference of π in our results.

4. Simulation

We perform a simulation based on the equation (3.17). Assume that the length of the Rb cell be L, and the optical fields enter the Rb cell at position z_0 and leave at position $z_0 + L$. With the probe field Ω_{10} entering the cell, equation (3.17) gives the transmitted probe field Ω_1 as the following,

$$\Omega_1(z_0 + L) = \Omega_{10}e^{-\alpha L} - i\frac{\eta\Omega_\mu\Omega_2}{\Gamma_{cb}\Gamma_{ab} + |\Omega_2|^2} \times \frac{1}{i\Delta k + \alpha}[e^{i\Delta k(z_0+L)} - e^{i\Delta k z_0 - \alpha L}], \tag{3.22}$$

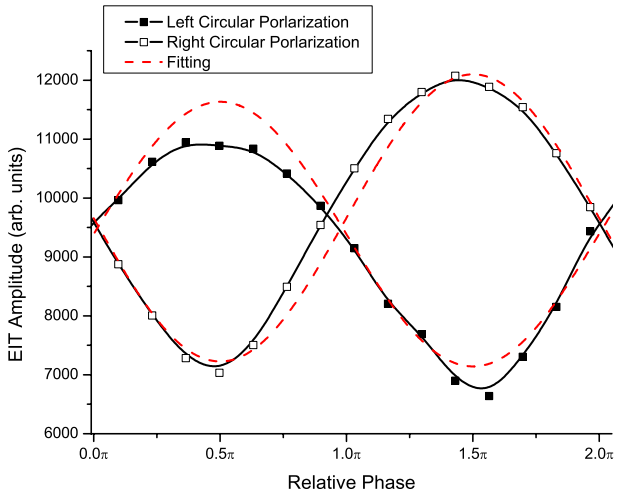

Fig. 15. The amplitude of EIT peaks dependence on relative phase. The solid squares and hollow squares correspond to the cases of left and right circularly polarized input laser fields respectively. Dash lines are fittings of the sinusoid function.

where α is the absorption coefficient which is given by

$$\alpha = \eta \frac{\Gamma_{cb}}{\Gamma_{cb}\Gamma_{ab} + |\Omega_2|^2} \ . \tag{3.23}$$

The simulation result is shown in Fig. 17. The parameters we used in the simulation are the following: $\gamma_{ab} = 5$, $\gamma_{bc} = 10^{-3}$, $\Omega_{10} = 0.1$, $\Omega_2 = 1$, $\Omega_\mu = 0.02$, $\eta = 0.9$, $L = 2.5\ cm$ and $\Delta k = 1.5\ cm^{-1}$. As varying the detuning, the maximum transmission appears at zero detuning. Meanwhile, the maximum transmission is oscillating when we change z_0 which determines the position of Rb cell, and the period of oscillation is about 4.4 cm. The simulation shows the similar behavior as the experimental results.

It is interesting to note that the obtained results can be considered for the realization of the stop-and-go slow light [51, 53, 52]. The dispersion can be modified in a controllable way that slows or accelerates the group velocity of light by tuning the

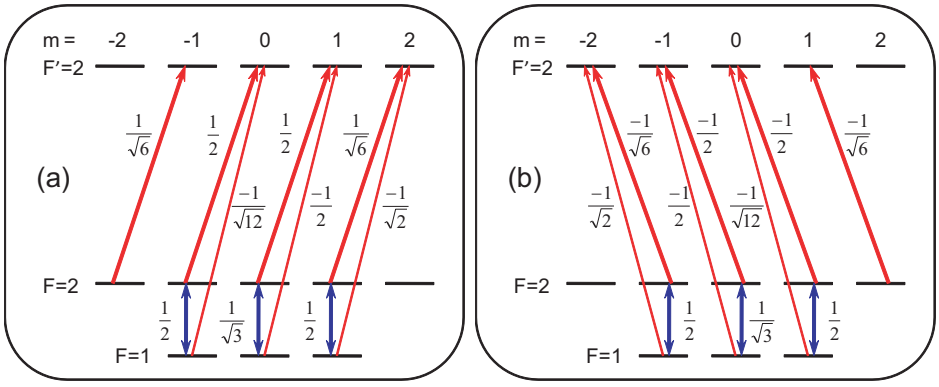

Fig. 16. Rb level scheme. The coupling between the right (a) and the left (b) circularly polarized optical probe and drive beams and Rb levels. Near each transition the corresponding Clebsch-Gordon factors are shown.

frequency of the microwave field near the resonance with the hyperfine transition.

The obtained results can be also applied to the backward scattering predicted in [13]. By controlling dispersion of the medium with the optical fields, a microwave field can be produced. Its direction of propagation is determined by the parameters of the fields, in particular, the detuning of the optical fields from the two-photon resonance.

The interest to this topic is also stimulated by the recent work [56, 55, 54] in which a quantum storage based on electromagnetically induced transparency has been predicted. The delay produced by slow light can be used in optical buffers, the delay time is limited by the absorption of probe field. Because the absorption of a microwave field is much smaller than optical fields, these systems have better controlled probe transparency, which is important for improving and optimizing efficiency of quantum storage [57, 58, 59, 60, 61]. Using auxiliary microwave field can improve the product of delay time and the bandwidth for the pulse case [62]. The broad range of applications stimulated our interest to the atomic system with the optical and microwave fields.

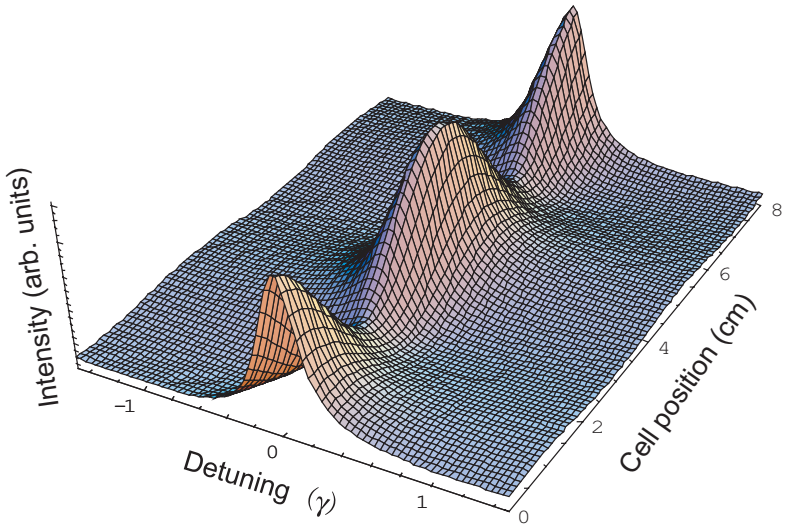

Fig. 17. Numerical simulation of the transmission of the probe field dependence on detuning and cell positions. In the simulation, we use $\gamma_{ab} = 5$, $\gamma_{bc} = 10^{-3}$, $\Omega_{10} = 0.1$, $\Omega_2 = 1$, $\Omega_\mu = 0.02$, $\eta = 0.9$, $L = 2.5\ cm$ and $\Delta k = 1.5\ cm^{-1}$.

CHAPTER IV

SPATIAL CONTROL OF LASER FIELDS IN A COHERENT MEDIUM

Optical properties of media can be changed dramatically due to interacting with optical fields. The ability to manipulate the medium's properties, such as absorption, dispersion and refractive index, allows one to control the properties of laser fields. In this chapter, we study the control of spatial properties of laser fields in a coherently driven medium as well as its applications.

The propagation of laser fields in a coherent medium is governed by equation (2.32), recall the equation

$$\frac{1}{2ik}\nabla_{\perp}^{2}\mathcal{E}+\frac{\partial}{\partial z}\mathcal{E}+\frac{1}{c}\frac{\partial}{\partial t}\mathcal{E}=\frac{ik}{2\epsilon_{0}}\mathcal{P}. \tag{4.1}$$

The second term on the left side is responsible to the field distribution in the propagation direction and it accounts for the dispersion and absorption of the medium. The first term on the left side is usually discarded in the cases where the profile of light beam is not important. In other cases, this term describes the field distribution in the transverse direction and it is crucial for the spatial manipulation of laser fields.

As an example, the spatial distribution in transverse direction can be manipulated by controlling the refractive index of medium. In EIT, the refractive index can be dramatically changed in the transparency window [5, 6, 63]. The change of refractive index is dependent on the intensity of laser field, usually the drive laser. Therefore, an inhomogeneous distribution of the drive laser intensity induces a gradient of refractive index which changes the propagation or beam profile of laser fields. Following this strategy, EIT can induce focusing and defocusing [64, 65] effects in a medium under proper conditions. It is even possible to realize EIT induced waveguiding [66, 67, 68] in which the drive laser works as an optical fiber and confine the

probe laser.

In this chapter, we first study the optical beam steering based on EIT. The possibility of using EIT to steer optical beams has been theoretically studied [69]. We have experimentally demonstrated [70] that a coherently driven Rb atomic gas can steer an optical beam just like a prism does. The device is then referred to "atomic prism". More important, the atomic prism possesses the highest spectral angular dispersion that has ever been shown, to the best of our knowledge. This property can be used to develop spectral devices with extremely high resolution.

In the second part of this chapter, we study the possibility of creating small spatial patterns by manipulating the intensity distribution of laser fields in EIT. Our experiments show that the spatial patterns can be smaller than the optical wavelength and beats the diffraction limit. This approach has potential applications in subwavelength imaging [71], lithography [72, 73] and nanoscale control of individual qubits [74].

A. Beam steering by an ultra-dispersive atomic prism

The ability to deflect and steer optical beams is important in modern optics. As a perfect example, a prism can not only deflect an optical beam but also spread out optical beams with different colors. On the one hand, the deflection of optical beam has important applications in many fields such as radar, optical imaging, laser machining and free space optical communication. On the other, the ability to spread out colors, which is characterized by angular dispersion, is essential to spectral devices and spectroscopy.

Many technologies have been developed for more accurate and faster beam steering. The simplest approach is to mechanically move or rotate a deflector such as

mirror and grating. Other approaches, such as using thermal gradient, acousto-optic effect or electro-optic effect to induce a gradient of refractive index, can provide faster control of beam deflection. Recent development has been focused on using photonic crystals [75] and phased arrays [76, 77]. A novel approach has been proposed [69] to use a light beam to deflect another light beam through the EIT effect. We have experimentally studied this effect and found that a coherently driven atomic gas can work as a prism to deflect an optical beam. The results have shown that this atomic prism has an extremely high angular dispersion which is at least six order of magnitude higher than that of a glass prism or a grating. Besides the potential applications of beam deflection and giant angular dispersion, the experiment is also of interest to fundamental physics such as the optical analogy of Stern-Gerlach experiment [78].

1. The idea of an atomic prism

A single frequency ray of light is bent by a prism upon an angle determined by the index of refraction, as shown in Fig. 18(a). Newton discovered several centuries ago that the dispersion of the index of refraction leads to spread of deviation angles for different wavelengths. We are trying to make a coherently driven atomic gas working like a prism and we call it "*atomic prism*".

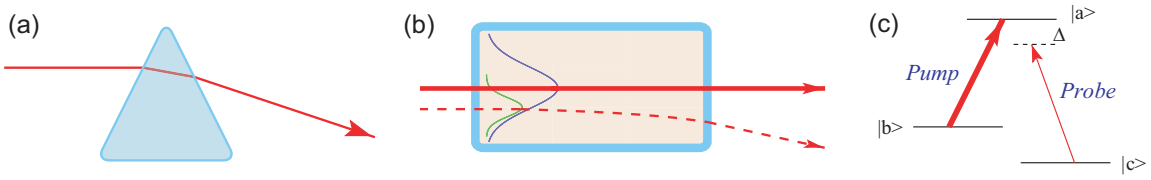

Fig. 18. (a) Refraction of light by the prism. (b) Configuration of the probe and drive laser beams inside the cell of Rb vapor. One can see that our setup can be viewed as a super-high dispersive prism. (c) Simplified scheme of the energy levels of Rb atoms.

The atomic prism is made of a cell filled with gas of three level atoms shown in Fig. 18(c). Two laser beams, drive and probe, are applied to realize EIT in the medium. The index of refraction is modified and dependent on the intensity of drive laser. As illustrated in Fig. 18(b), since the drive laser has a Gaussian profile, it induces a gradient of refractive index on the slope of Gaussian peak. If we align the probe laser on the slope of drive, it experiences the gradient of refractive index and changes the direction of propagation. Meanwhile the refractive index varies as the frequency of probe is varying within the EIT window. The deflection is different for different frequency. This property introduces an angular dispersion which is extremely high because of the extreme nonlinearity in EIT. Here we develop a simple mathematic description of the idea.

For a dispersive medium, the index of refraction is given by

$$n' = \sqrt{1 + \chi'(\omega)}, \tag{4.2}$$

where χ' is the susceptibility of the medium. It is frequency dependent and its specific form for our experiment will be discussed in the later text. The trace of a light beam propagating in a medium can be found by using the eikonal equation [79]. Start with Maxwell's equation,

$$\nabla^2 E - \frac{1}{c^2}\frac{\partial^2 E}{\partial t^2} = \mu_0 \frac{\partial^2 P}{\partial t^2}. \tag{4.3}$$

The field and the polarization can be expressed in terms of the slowly varying amplitudes E_ν and P_ν, and the eikonal ψ,

$$E = \sum_\nu E_\nu e^{-i\nu t + ik\psi}, \quad P = \sum_\nu P_\nu e^{-i\nu t + ik\psi}, \tag{4.4}$$

where $k = \nu/c$. The polarization of the medium is related to the field intensity as $P_\nu = \varepsilon_0 \chi_\nu E_\nu$, where the susceptibility $\chi_\nu = \chi'_\nu + i\chi''_\nu$. Neglecting the second order

derivative over coordinates for amplitude E_ν, we obtain the eikonal equation given by

$$(\nabla\psi)^2 = 1 + \chi' = n'^{\,2}. \tag{4.5}$$

The trajectory of the light rays propagating in an inhomogeneous medium can be found by solving a geometrical optics differential equation [79] that is given in vector form by

$$\frac{d}{ds}\left(n'\frac{d\mathbf{R}}{ds}\right) = \nabla n' \tag{4.6}$$

where $\mathbf{R}$ is the the point of the ray defined as $\mathbf{R}(x,z) = X(z)\hat{\mathbf{x}} + z\hat{\mathbf{z}}$, $\hat{\mathbf{x}}$ and $\hat{\mathbf{z}}$ are the unit vectors along the axes. Then, for the x and z components,

$$\frac{d}{ds}\left(n'\frac{dX}{ds}\right) = \frac{\partial n'}{\partial x}, \text{ and } \frac{d}{ds}\left(n'\frac{dz}{ds}\right) = \frac{\partial n'}{\partial z}. \tag{4.7}$$

The equation describing the amplitude of the electromagnetic field can be obtained similarly as we obtain equation (4.5). From the imaginary part of equation (4.3), we can get the equation

$$2k\nabla\psi\nabla E_\nu + k\nabla^2\psi E_\nu = -\frac{\nu^2}{c^2}\chi'' E_\nu. \tag{4.8}$$

The solution of the above equation has the following form

$$E_\nu = \frac{E_{0\nu}}{\sqrt{n'}}\exp\left(-\int_{s_1}^{s_2}\frac{\nu\chi''}{2n'c}ds\right). \tag{4.9}$$

At this point, the trajectory of light ray can be described by equations (4.7) and the absorption of the field can be described by equations (4.8, 4.9). The exact behavior depends on the susceptibility χ which is determined by the natural of the medium and the interaction with laser fields.

Our particular interest is the deflection angle of the beam when there is an induced gradient of refractive index. Consider an example in which the medium is

an atomic gas, the index varies in the transverse direction only and the variation is small so that the deflection is also small. From equation (4.7), we have

$$n' \frac{dX}{ds} = \int_{s(x=0)}^{s(x=L)} \nabla_\perp n' ds \simeq L \nabla_\perp n', \tag{4.10}$$

here L is the length of the sample, we use $s(x = L) - s(x = 0) \simeq L$ since the deflection angle is small. Integrate it again and consider the refractive index $n' \simeq 1$ for gas, we can find the beam variation in the transverse direction,

$$X = L^2 \frac{\nabla_\perp n'}{n'} \simeq L^2 \nabla_\perp n', \tag{4.11}$$

therefore the deflection angle θ can be estimated by

$$\theta = \frac{X}{L} = L \nabla_\perp n'. \tag{4.12}$$

This simple expression confirms the idea of using the gradient of refractive index to defect the laser beam. In the following section, we demonstrate this effect experimentally in a Rb gas driven by two laser beams under EIT conditions.

2. Experimental implementation

The experimental setup is illustrated in Fig. 19. An external cavity diode laser is used as the light source. The frequency is tuned to the center of the Doppler broadened D_1 line of ^{87}Rb atoms, specifically at the transition $5^2S_{1/2}(F = 2) \rightarrow 5^2P_{1/2}(F = 1)$. The laser beam is split into two beams which are tuned to possess orthogonal polarizations. The beams are later combined and a quarter wave plate converts the linear polarizations into two orthogonal circular polarizations. The beams, each has the power of 0.5 mW, are coupled with two ground state Zeeman sublevels and an excited state as shown in the energy diagram in Fig. 19. The rubidium cell with the length of 7.5 cm is installed in a magnetic shield, it is temperature controlled to

reach the atomic density of $N = 3 \times 10^{11}$ cm^{-3}. A longitudinal magnetic field can be applied to change the splitting of Zeeman sublevels so that the two photon detuning can vary.

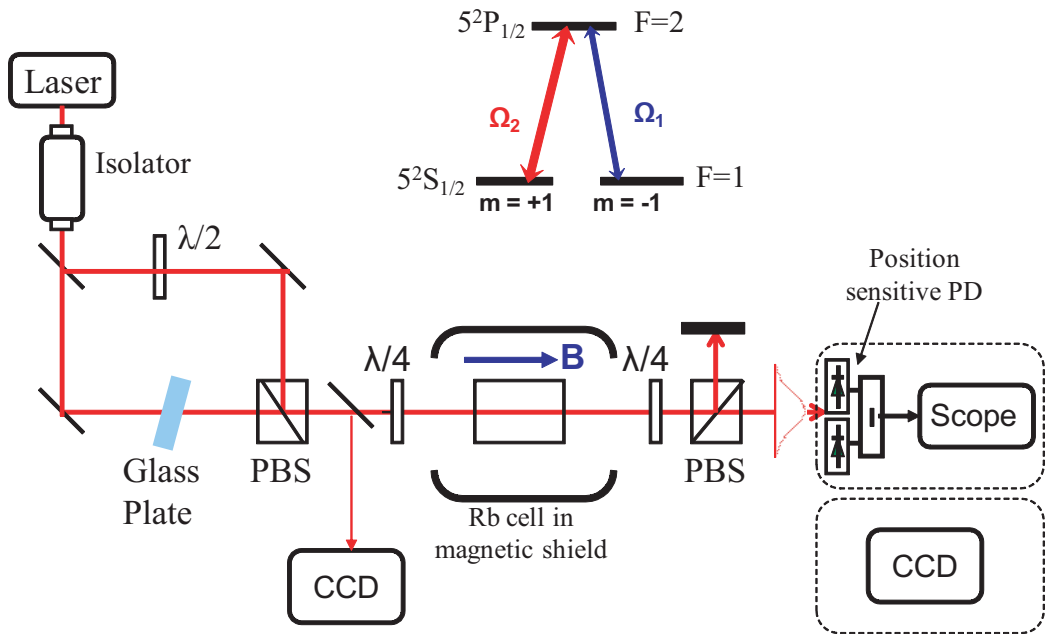

Fig. 19. The experimental setup of atomic prism and the corresponding energy scheme of Rb atoms. PBS is polarizing beam splitter. The glass plate is inserted to shift the beam yet keep the parallelism of the beams.

Two independent techniques are used to measure the probe beam position and the angle of deviation. The first technique is based on using a CCD camera and a removable mirror in front of the cell to measure the positions of the drive and probe beams. The CCD camera is used to record an optical field distribution for selected two-photon detuning. The second technique uses a position sensitive detector (PSD) [80] to obtain a relatively more accurate and continuous measurement of the beam direction. A PSD consists of a pair of photodiodes which are installed close to each other. If the laser beam covers the pair of photodiodes symmetrically, the difference signal from two photodiodes gives zero. The difference signal becomes non zero if the

laser beam moves, the magnitude of the signal tells us the displacement of laser beam. The distance from the center of the cell to PSD is 1 meter and to the CCD camera is 2.3 meters. We confirm that the measurements by each technique are consistent with each other.

The drive and probe beams are aligned to be parallel to each other initially. The probe beam can then be adjusted to the left or right side of the drive beam profile, shown in Fig. 20(a) and (c), by tilting a parallel glass plate. As the probe and drive beams are passing through the cell, the probe field experiences a gradient of refractive index due to the inhomogeneous intensity distribution of the drive field. As a result, the probe field is deflected and the deflection angle is dependent on the two photon detuning. The beam profiles recorded by the CCD camera are shown in Fig. 20. Prior to entering the cell, the probe field sits on either the right (a) or left (c) slope of the drive field. The probe field is observed being deflected in opposite directions. The CCD camera is also used to record the probe beam profiles at the distance of 2.3 m after it passes the cell. We can see the movement of the probe beam as the two photon detuning is varying. We record the probe beam profiles at the detunings where the maximum deviation occurs, as shown in (b) and (c). The experimental results show the deflection of laser beam caused by another beam through EIT.

However, one concern of the data might be that the behaviors are not exactly symmetric for the right and left cases. The reason is the imperfection of beam profiles in our experiments. The drive beam does not have a good Gaussian distribution as we expected. The intensity distribution is not very symmetric nor smooth. This introduces the complexity in the deflected probe beam profile. A better prepared Gaussian beam can work better. Another concern is the diffraction of laser beams. The width of the probe beam (0.7 mm at the Rb cell) is increased by about 1.7 times at 2.3 meter distance from the cell due to diffraction (the diffraction angle

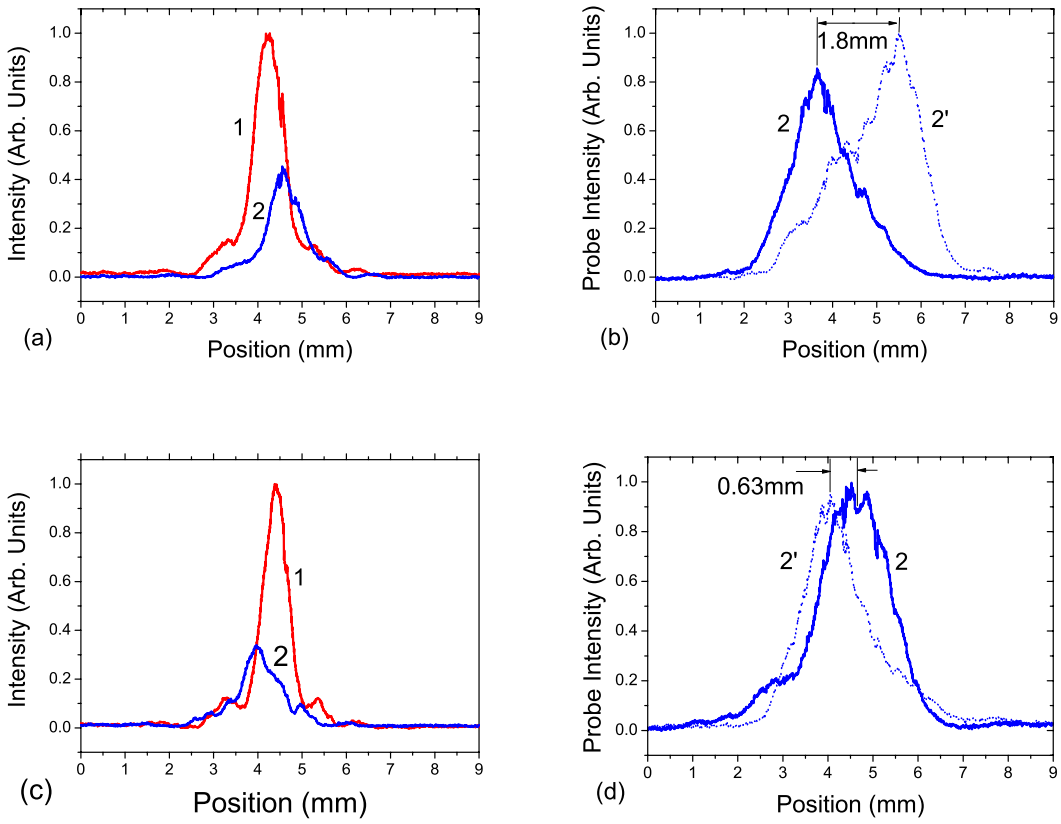

Fig. 20. The spatial distributions of the drive (1) and probe (2) fields at the input of the atomic cell. The probe is on either the right (a) or left (c) slope of the drive field. Figures (b) and (c) show the spatial distributions of the probe fields (2) and (2') at the distance of 2.3 meters after passing the atomic cell for different detunings corresponding to the maximum angles of deviation.

for a Gaussian beam profile is given by $2\lambda/\pi d$, where d is the diameter of the laser beam). For the data shown in Fig. 20(b), the displacement is larger than the spread of the probe beam due to the diffraction. Although the displacement in Fig. 20(d) is smaller than the diffraction spreading, the beam profiles systematically shift to two directions. So the deflection of probe beam is not caused by the diffraction.

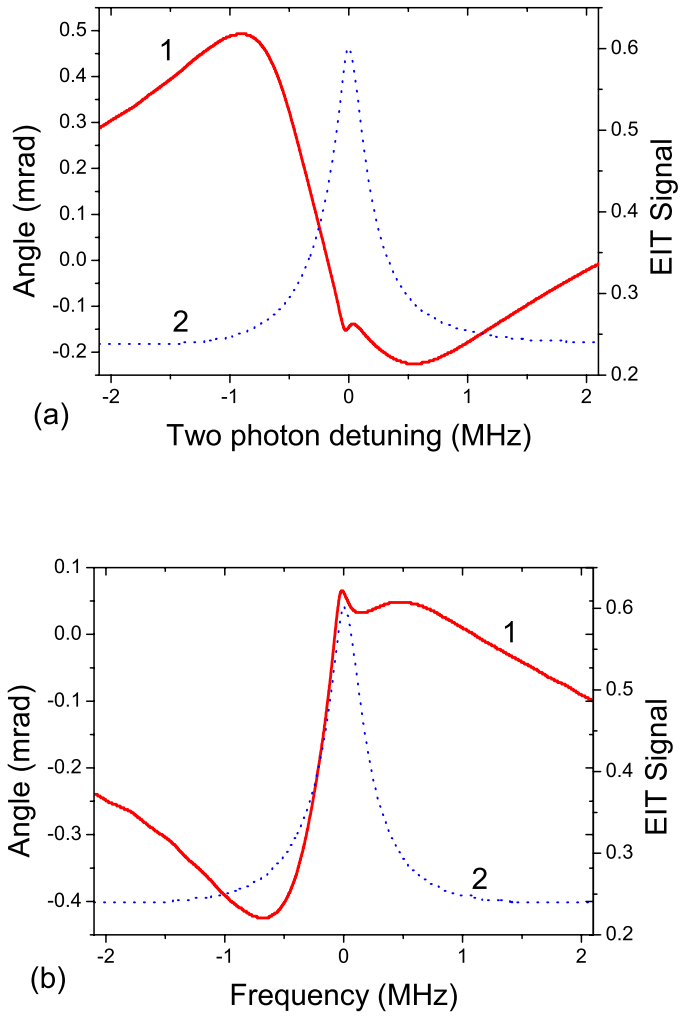

Fig. 21. (1) Dependence of the deflection angle of the probe beam on detuning for the probe beam initially shifted to the right (a) and left (b) slope of the drive beam. (2) Dependence of the probe field transmission on detuning.

To obtain the dependence of deflection angle on the two photon detuning, we replace the CCD camera with a PSD. The PSD is mounted on a translational stage, with which the voltage to displacement conversion is calibrated for the probe laser beam. The deflection angle, converted from the displacement, is continuously recorded as we change the detuning. As shown in Fig. 21, red curves (1) show how the deflection angle changes with the detuning for the cases with the probe beam initially sitting on the right (a) and left (b) slope of the drive. Blue dotted curves (2) are the EIT peaks. The dramatic deflection occurs within the EIT window. The maximum deflection is about 0.7 mrad. Considering the change of the deflection angle within a very small frequency change, the data indicates a very large angular dispersion. An estimation of the slope of the deflection angle curve gives the angular dispersion $d\theta/d\lambda \simeq 10^3$ rad/nm. Comparing with glass prisms ($d\theta/d\lambda \simeq 10^{-4}$ rad/nm) or diffraction gratings ($d\theta/d\lambda \simeq 10^{-3}$ rad/nm), the atomic prism has the potential to provide much better spectral resolution as a spectral device. It can spatially separate the light beams with the frequency difference of few kHz.

3. Numerical simulation

Using the density matrix approach, we perform the numerical simulation for a three level system coupled with two laser fields as shown in Fig. 18(c). The interaction Hamiltonian of the system can be written as

$$V_I = -\hbar[\Omega_1 e^{-i\omega_{ab}t}|a\rangle\langle b| + \Omega_2 e^{-i\omega_{ac}t}|a\rangle\langle c| + h.c.] \tag{4.13}$$

where $\Omega_{1,2} = \wp_{1,2}\mathcal{E}_{1,2}/\hbar$ is the Rabi frequency of the probe (drive) field, and ω_{ab}, ω_{ac}, ω_{cb} are the frequency differences between the corresponding atomic energy levels. The

time-dependent density matrix equations are given by

$$\frac{\partial \rho}{\partial \tau} = -\frac{i}{\hbar}[V_I, \rho] - \frac{1}{2}(\Gamma\rho + \rho\Gamma), \tag{4.14}$$

where Γ is the relaxation matrix. A self-consistent system also includes the field propagation equations

$$\frac{\partial \Omega_1}{\partial z} = -i\eta_1 \rho_{ab}, \quad \frac{\partial \Omega_2}{\partial z} = -i\eta_2 \rho_{ac}, \tag{4.15}$$

where $\eta_j = \nu_j N \wp_j^2/(2\epsilon_0 c)$ are the coupling constants ($j = 1, 2$), N is the particle density of the medium, ϵ_0 the permitivity in vacuum. The equations of motion for the density matrix elements of the polarization ρ_{ab} and the coherence ρ_{cb} are given by

$$\dot{\rho}_{ab} = -\Gamma_{ab}\rho_{ab} + i\Omega_1(\rho_{aa} - \rho_{bb}) - i\rho_{cb}\Omega_2^*, \tag{4.16}$$

$$\dot{\rho}_{cb} = -\Gamma_{cb}\rho_{cb} + i\rho_{ca}\Omega_1 - i\rho_{ab}\Omega_2. \tag{4.17}$$

where $\Gamma_{ab} = \gamma_{ab} + i(\omega_{ab} - \nu_1)$; $\Gamma_{ca} = \gamma_{ca} - i(\omega_{ac} - \nu_2)$; $\Gamma_{cb} = \gamma_{cb} + i(\omega_{cb} - \nu_1 + \nu_2)$; ω_{cb} is the frequency of $c \rightarrow b$ transition, and $\gamma_{\alpha\beta}$ are the relaxation rates at the corresponding transitions.

Assuming that the drive field is much stronger than the probe field ($|\Omega_1|^2 \ll |\Omega_2|^2$), then $\rho_{bb} \simeq 1$, and the succeptibility is given by

$$\chi = \frac{-i\eta\Gamma_{cb}}{\Gamma_{ab}\Gamma_{cb} + |\Omega_2|^2}. \tag{4.18}$$

The index of refraction is $n \simeq 1 + \frac{1}{2}\mathrm{Re}(\chi)$, and the angle of refraction can be found by solving

$$\frac{\partial \tan\theta}{\partial z} = \frac{1}{2}\frac{\partial \chi'}{\partial x} = \mathrm{Re}\left(\frac{i\eta}{(\Gamma_{cb}\Gamma_{ab} + |\Omega_2|^2)^2}\right)\frac{\partial |\Omega_2|^2}{\partial x}, \tag{4.19}$$

for our case the refraction angle is small so $\tan\theta \simeq \theta$, we can rewrite equation (4.19)

in the form

$$\theta = 2\pi \int_0^L dz \frac{\partial \chi'}{\partial x}, \tag{4.20}$$

where L is the length of the cell.

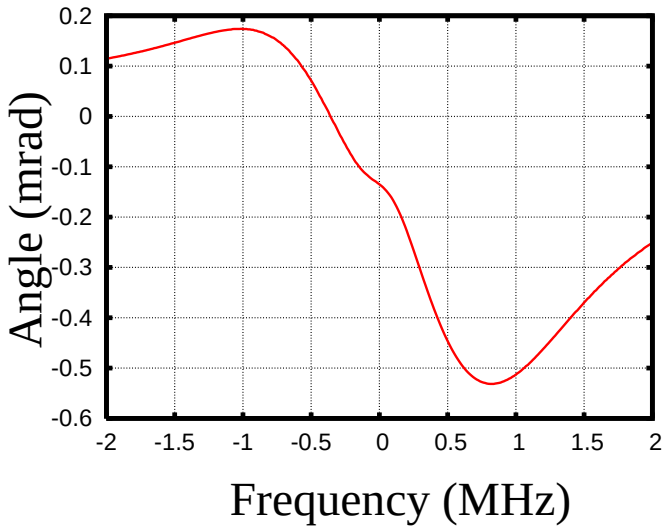

Fig. 22. Numerical simulation of the dependence of deflection angle on the detuning.

The numerical simulation of the dependence of deflection angle on detuning is shown in Fig. 22. The following parameters are used for the simulations: atomic density is $N = 3 \times 10^{11}$ cm^{-3}, the spin transition relaxation rate is $\gamma_{cb} = 10$ kHz, the homogeneous broadening of optical transitions is pure due to the radiative broadening determined by spontaneous relaxion and is given by $\gamma_{ab} = 5$ MHz, the Rabi frequency of the driving field $\Omega_2 = 4\gamma$. The simulation result has a good agreement with the experimental results.

In conclusion, we have experimentally demonstrated an atomic prism based on EIT and it has an extremely large angular dispersion. The obtained results have shown the capability of deflecting laser beams as well as spreading the light beams with small frequency difference. This technique can be potentially used for a spectral

device with an ultra-high spectral resolution. It can also be used to realized all optical steering and produce optical delay lines for radar system. However, the challenge remains on how to apply this technique to very short laser pulses or the applications with weak fields, such as single photon sources and controlling the flow of photons at the level of single quanta [81, 82].

B. Sub-diffraction optical beam for imaging and lithography *

In 1873, Ernst Abbe discovered that a lens-based optical microscope can not resolve two objects that are closer than half of the wavelength. Classically, the diffraction limit sets the half wavelength barrel for improving the spatial resolution of many applications including microscopy, optical lithography and atom localization, to name a few. The ability to create a small optical structure is essential to these applications since the size of the smallest optical structure, such as a focal spot by a lens, ultimately determines the resolution.

Recently, several methods have been proposed to overcome the diffraction limit. Based on the idea of quantum eraser [83], quantum entanglement between photons is used to produce novel interference effects which lead to subwavelength fringes [84, 85]. However, the difficulty of generating pure, high-order entangled photons and correlated detection slows down the practical realization of this idea. Alternatively, classical fields can also achieve the subwavelength interference pattern by using the Doppleron-type resonances [72, 73]. With the careful arrangements of classical field amplitude and phase, the fluorescence enables one to locate the position of atoms with the subwavelength precision [86, 87, 88, 89]. In the microscopy for biomedical

*Part of the data reported in this section is reprinted with permission from "*Optical imaging beyond the diffraction limit via dark states*," by H. Li *et al.*, Phys. Rev. A **78**, 013803 (2008), Copyright by the American Physical Society.

applications, the methods such as stimulated emission depletion (STED) [71, 90], photo-activated localization microscopy (PALM) [91] and stochastic optical reconstruction microscopy (STORM) [92] have experimentally achieved the subwavelength resolution.

In this section, we propose an approach to create spatial patterns having subwavelength size by using the dark states formed by the interaction between atoms and optical fields. Similar approaches have been theoretically studied by several groups [73, 74, 93, 94]. We have carried out, to the best of our knowledge, the first experiment [95] to demonstrate the proof of principle.

1. Beating the diffraction limit via dark states

As a qualitative introduction, assume that the drive field Rabi frequency Ω_d has the particular spatial distribution sketched in Fig. 23(a) by the solid line (1). The weak probe field Rabi frequency Ω_p has a diffraction limited distribution shown by the dashed line (2) in Fig. 23(a). The probe and drive fields are applied to an ensemble of atoms. According to the field distribution of the drive field, the absorption of the medium can be sketched as Fig. 23(b). At all positions where the drive field is strong enough ($\Omega_p \ll \Omega_d$), the dark state, which is given [1] by $|D\rangle = (\Omega_p|c\rangle - \Omega_d|b\rangle)/\sqrt{\Omega_p^2 + \Omega_d^2}$, is practically $|b\rangle$. When the drive field is zero or weak, the dark state is approximately $|c\rangle$. Depending on the intensity of the drive field and the optical density of the medium, we may have a narrow dip (Fig. 23(c)) or sharp peaks (Fig. 23(d)) in the transmission of the probe field. The width of the dip or peaks depends on the relaxation rate γ_{cb} between levels $|b\rangle$ and $|c\rangle$ and the Rabi frequency of the drive field. In either case, the width is narrower than the width in the profile of the drive field which is ultimately diffraction limited to the size of half wavelength. Therefore, the structures created in the transmitted probe field have the characteristic

size smaller than the diffraction limit.

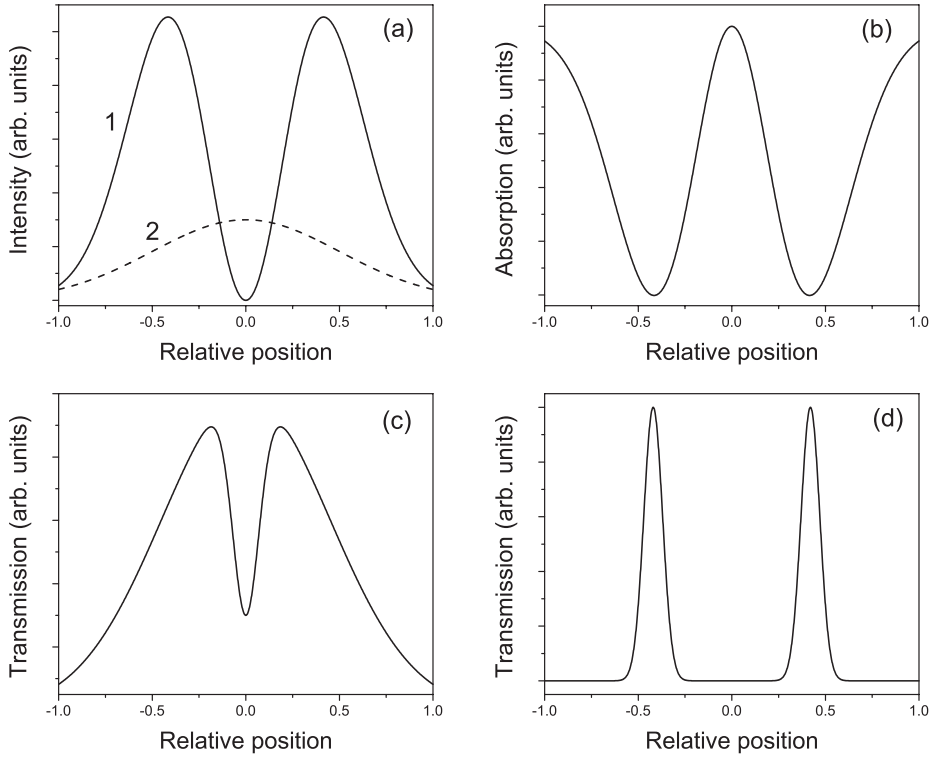

Fig. 23. Qualitative description of the idea. (a) Distribution of the drive (1) and the probe (2) fields vs. a transverse spatial coordinate at the entrance to the cell. (b) Dependence of the absorption coefficient given by Eq.(4.24) vs position. Plots (c) and (d) show the distribution of the probe beam after propagating through the cell. Case (c) is for a strong drive field and relatively low optical density. Case (d) is for a relatively weak drive field and large optical density.

We now present a simple mathematical description. The Hamiltonian of a three-level atom interacting with optical fields (see the inset in the figure on page 63 for the energy diagram) is given by

$$H = \hbar\Omega_d|a\rangle\langle b| + \hbar\Omega_p|a\rangle\langle c| + adj., \tag{4.21}$$

where $\Omega_{d,p} = \wp_{d,p}E_{d,p}/\hbar$ are the Rabi frequencies of the drive E_d and the probe E_p

fields, respectively; $\wp_{d,p}$ are the dipole moments of the corresponding optical transitions. Then, the atomic response is given by the set of density matrix equations

$$\dot{\rho} = -\frac{i}{\hbar}[H, \rho] - \frac{\Gamma\rho + \rho\Gamma}{2} \tag{4.22}$$

where Γ describes the relaxation processes. The propagation of the probe field Ω_p through the cell is governed by Maxwell's Equations and, for propagation in the z-direction, can be written in terms of the probe field Rabi frequency as

$$\frac{\partial\Omega_p}{\partial z} = -i\eta\rho_{ab} - i\frac{1}{2k}\frac{\partial^2}{\partial x^2}\Omega_p. \tag{4.23}$$

The first term accounts for the dispersion and absorption of the resonant three-level medium, and the second term describes the focusing and/or diffraction of the probe beam. The density matrix element ρ_{ab} is related to the probe field absorption which in turn depends on the detuning and the drive field. This is characterized by an absorption coefficient:

$$\kappa = \eta\frac{\Gamma_{cb}}{\Gamma_{ab}\Gamma_{cb} + |\Omega_d(z,x)|^2}, \tag{4.24}$$

where $\Gamma_{cb} = \gamma_{cb} + i\omega$ and $\Gamma_{ab} = \gamma + i\omega$; $\omega = \omega_{ab} - \nu$ is the detuning from the atomic frequency ω_{ab}; γ is the relaxation rate at the optical transition; and $\eta = 3\lambda^2 N\gamma_r/8\pi$; N is the atomic density; γ_r is the spontaneous emission rate. We now assume that the drive field has a distribution of intensity near its extrema given by

$$|\Omega_d(z,x)|^2 = |\Omega_0|^2 \begin{cases} \left[1 - \left(\frac{|x|-x_0}{L}\right)^2\right], & |x| \simeq x_0, \\ \left(\frac{x}{L}\right)^2, & |x| \ll L, \end{cases} \tag{4.25}$$

where $\Omega_0 = \Omega_d(z, x_0)$, L is the separation distance between the peaks of the drive field distribution, and a typical absorption profile vs. x is shown in Fig. 23(b). Neglecting the diffraction term in Eq.(4.23), we can write an approximate solution for Eq. (4.23)

as

$$\Omega_p(z,x) = \Omega_p(z=0,x)\exp(-\kappa z). \tag{4.26}$$

For relatively low optical density ($\kappa z \simeq 1$), nearly all of the probe field propagates through the cell except for a small part where the drive field is zero. Absorption occurs there because the probe beam excites the atomic medium.

We now estimate the width of the region of the excited medium in the vicinity of zero drive field. Since κz is small, we can rewrite equation (4.26) as

$$\begin{aligned} \Omega_p(z,x) &\simeq \Omega_{p0}(1-\kappa z) \\ &= \Omega_{p0}(1-\eta\frac{\Gamma_{cb}z}{\Gamma_{ab}\Gamma_{cb}+|\Omega_d(z,x)|^2}), \end{aligned} \tag{4.27}$$

where $\Omega_{p0} = \Omega_p(z=0,x)$. When the probe field exits the cell ($z = z_0$), the Rabi frequency of the field at the position $x = 0$ (at this point $|\Omega_d|^2 = 0$) is given by

$$\Omega_p(z_0,0) = \Omega_{p0}(1-\frac{\eta z_0}{\Gamma_{ab}}). \tag{4.28}$$

Suppose that we have the half maximum (intensity) at the position $x = x_h$, it satisfies the following equation

$$\frac{1}{\sqrt{2}}(\Omega_{p0}\frac{\eta z_0}{\Gamma_{ab}}) = \Omega_{p0}\eta\frac{\Gamma_{cb}z_0}{\Gamma_{ab}\Gamma_{cb}+|\Omega_0|^2(\frac{x_h}{L})^2}. \tag{4.29}$$

The solution of the equation gives

$$\begin{aligned} x_h &= (\sqrt{2}-1)^{1/2}L\sqrt{\frac{\Gamma_{ab}\Gamma_{cb}}{|\Omega_0|^2}} \\ &\simeq 0.64L\sqrt{\frac{\Gamma_{ab}\Gamma_{cb}}{|\Omega_0|^2}}. \end{aligned} \tag{4.30}$$

So the width (FWHM) of the dip in Fig. 23(c) is given by

$$\Delta x = 1.28L\sqrt{\frac{\Gamma_{ab}\Gamma_{cb}}{|\Omega_0|^2}}. \tag{4.31}$$

This region can potentially become smaller if the drive field becomes stronger. However, the contrast is limited because of the finite absorption of the medium at the center of optical field.

For higher optical density, this narrow feature becomes broadened (compare Fig. 23(c) and (d)), but two narrow peaks are formed during the propagation of the probe beam (see Fig. 23(d)). We now estimate the width of these peaks. Pick up the peak on the right, the maximum is at the position $x = x_0$. Suppose that the half maximum (intensity) is at the position $x = x_h$, it satisfies the equation

$$\frac{1}{\sqrt{2}}\Omega_{p0}\exp[-\kappa(x=x_0)z_0] = \Omega_{p0}\exp[-\kappa(x=x_h)z_0]. \tag{4.32}$$

The absorption coefficient κ at the positions x_0 and x_h can be written as

$$\kappa(x=x_0) = \eta\frac{\Gamma_{cb}}{\Gamma_{ab}\Gamma_{cb}+|\Omega_0|^2} \simeq \eta\frac{\Gamma_{cb}}{|\Omega_0|^2}, \tag{4.33}$$

$$\kappa(x=x_h) = \eta\frac{\Gamma_{cb}}{\Gamma_{ab}\Gamma_{cb}+|\Omega_0|^2[1-(\frac{x_h-x_0}{L})^2]} \simeq \eta\frac{\Gamma_{cb}}{|\Omega_0|^2}[1+(\frac{x_h-x_0}{L})^2], \tag{4.34}$$

where we assume that the drive field is strong ($\Gamma_{ab}\Gamma_{cb} \ll |\Omega_0|^2$), and the width of the peak is narrow ($x_h - x_0 \ll L$). Plug the absorption coefficients into equation (4.32), we have

$$\frac{\eta\Gamma_{cb}z_0}{|\Omega_0|^2} = -\ln\sqrt{2} + \frac{\eta\Gamma_{cb}z_0}{|\Omega_0|^2}[1+(\frac{x_h-x_0}{L})^2], \tag{4.35}$$

solving this equation gives us

$$x_h - x_0 = (\ln\sqrt{2})^{\frac{1}{2}}L\sqrt{\frac{|\Omega_0|^2}{\eta\Gamma_{cb}z_0}}. \tag{4.36}$$

For the zero detuning, the width (FWHM) of the peaks in Fig. 23(d) is given by

$$\Delta x = 1.18L\sqrt{\frac{|\Omega_0|^2}{\eta\gamma_{cb}z_0}}. \tag{4.37}$$

The drive field provides flexibility for creating patterns with size smaller than

the wavelength of the laser. Depending on the conditions (such as laser intensity and optical density), we are enable to create a subwavelength dip (Fig. 23(c)) or peak (Fig. 23(d)). The width of the structures depends on the laser intensity and the relaxation rates Γ_{ab} and Γ_{cb}. The width can be characterized by equations (4.31, 4.37). The distribution of fields is governed by electrodynamics and has a diffraction limit. In this approach, we take the advantage of the size of atoms to overcome the diffraction limit. The distribution of atoms in their excited states is not related to the diffraction limit, but rather determined by the relaxation rates Γ_{ab} and Γ_{cb}, and thus can have spatial sizes smaller than the wavelength.

2. A proof-of-principle experiment

We have done a proof-of-principle experiment in Rb vapor to demonstrate our approach. We have observed that the distribution of the transmitted probe beam intensity has a double-peak pattern, which is similar to that of the drive beam, but the width of the peaks of the probe beam is narrower than that of the drive beam.

The experimental schematic is shown in Fig. 24. We obtain a good quality spatial profile by sending the radiation of an external cavity diode laser through a polarization-preserving single-mode optical fiber. The laser beam is vertically polarized and split into two beams (drive and probe). The probe beam carries a small portion of the laser intensity, and its polarization is rotated to be horizontal.

To create a double-peak spatial distribution for the drive field, the drive beam is split into two beams that cross at a small angle, using a Mach-Zehnder interferometer (shown in the dashed square of Fig. 24). A typical two-peak interference pattern of crossing beams is shown as Fig. 24A.

The probe and drive beams combine on a polarizing beam splitter, arranged so that the probe field and the interference pattern of the drive field are overlapped in

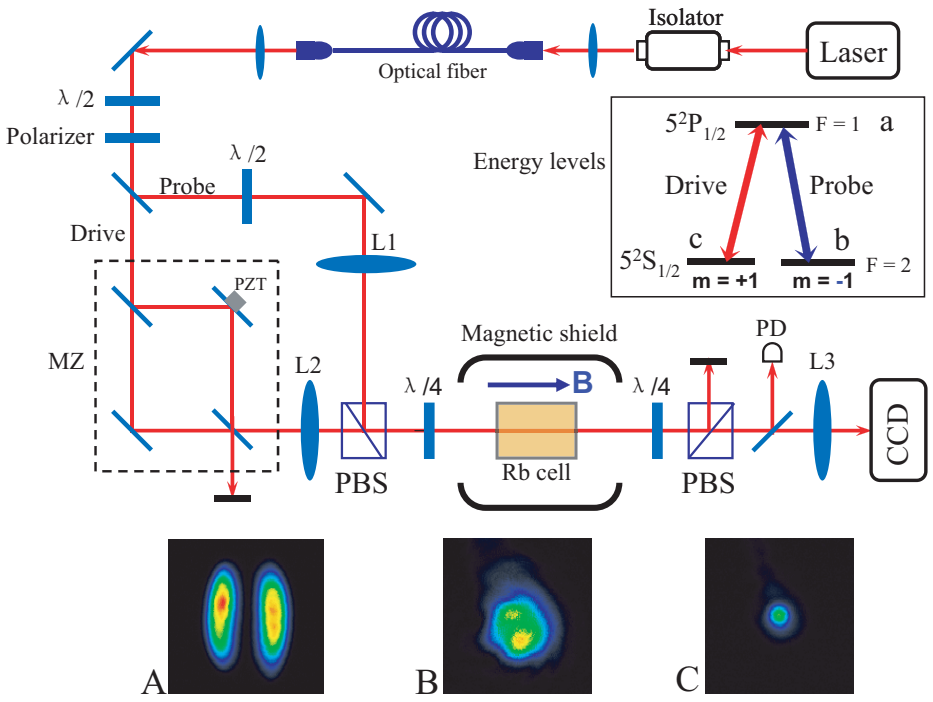

Fig. 24. Experimental schematic. $\lambda/2$: half-wave plate; $\lambda/4$: quarter-wave plate; L1, L2, L3: lenses; MZ: Mach-Zehnder interferometer; PZT: piezoelectric transducer; PBS: polarizing beam splitter, PD: photo diode; CCD: CCD camera. Picture A is the spatial intensity distribution of the drive field. Picture B is the beam profile of the parallel probe beam without the lens L1. Picture C is the beam profile of the diffraction limited probe beam with the lens L1. The inset is the energy diagram of the Rb atom, showing representative sublevels.

a Rb cell. The Rb cell has a length of 4 cm, and is filled with ^{87}Rb. A magnetic shield is used to isolate the cell from any environmental magnetic fields, while a solenoid provides an adjustable, longitude magnetic field. The cell is installed in an oven that heats the cell to reach an atomic density of 10^{12} cm^{-3}. The laser is tuned to the D_1 line of ^{87}Rb at the transition $5^2S_{1/2}(F = 2) \rightarrow 5^2P_{1/2}(F = 1)$. As shown in the inset of Fig. 24, the states $|a\rangle$, $|b\rangle$ and $|c\rangle$ correspond to the Zeeman sublevels as the following $|a\rangle = |5^2P_{1/2}, F = 1, m = 0\rangle$, $|b\rangle = |5^2S_{1/2}, F = 1, m = -1\rangle$,

$|c\rangle = |5^2S_{1/2}, F = 1, m = +1\rangle$.

As stated above, the probe and drive beams have the orthogonal linear polarizations. A quarter-wave plate converts them into left and right circularly polarized beams, which couple two Zeeman sublevels of the lower level and one sublevel of the excited level of the Rb atoms (see the inset of Fig. 24).

After passing through the cell, the probe and drive beams are converted back to linear polarizations by another quarter-wave plate and the separated by a polarizing beam splitter (PBS). The power of transmitted probe field is monitored by a photodiode (PD). The spatial intensity distribution of probe field is recorded by an imaging system, consisting of the lens L3 and a CCD camera.

The intensity of the probe beam is low enough that its transmission through the cell is almost zero without the presence of drive laser. Applying the drive laser makes the atomic medium transparent for the probe laser wherever the EIT condition is satisfied. If the drive laser has a certain transverse spatial distribution, then that pattern can be projected to the transmission profile of the probe laser.

Two different experiments have been performed. In the first experiment, the lenses L1 and L2 are not used, and the probe beam is a parallel beam with a diameter of 1.4 mm. The image of the drive intensity distribution in the cell is shown in Fig. 25(a). The probe intensity has a Gaussian distribution before entering the cell, and its distribution is similar to the drive intensity distribution after the cell. As shown in Fig. 25(b), however, the transmitted probe intensity has a distribution that has sharper peaks compared with the pattern of the drive intensity. The horizontal cross-sections of the drive and the transmitted probe distributions are shown in Figs. 25(c) and (d) respectively. In the drive intensity profile, the width (FWHM) of the peaks is 0.4 mm. The width (FWHM) of the peaks in the transmitted probe intensity profile is 0.1 mm. The spacing between two peaks is the same for both the

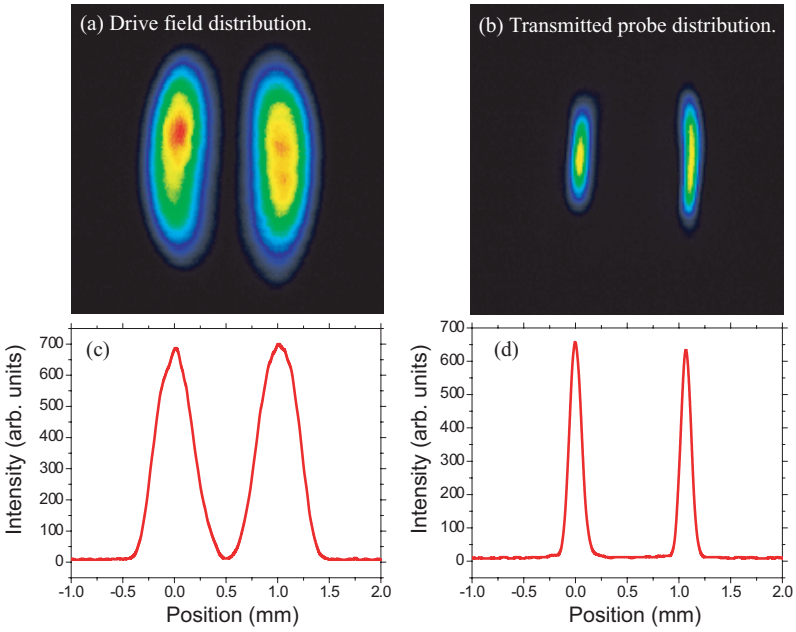

Fig. 25. The results of the experiment with a parallel probe beam. Picture (a) shows the image of the intensity distribution of the drive field in the Rb cell. Picture (b) shows the intensity distribution of the transmitted probe field. Curves (c) and (d) are the corresponding intensity profiles. The widths of the peaks in curves (c) and (d) are 0.4 mm and 0.1 mm, respectively.

drive and transmitted probe fields. We define the *finesse* as the ratio of the spacing between peaks to the width of peaks. The finesse of the transmitted probe intensity distribution is a factor of 4 smaller than that of the drive intensity distribution.

In the second experiment, the lenses L1 and L2 are used. A parallel probe beam (Fig. 24B) with a diameter of 1.4 mm is focused by the lens L1, which has a focal length of 750 mm. The beam size at the waist is 0.5 mm, which is diffraction limited. To assure experimentally that the beam is diffraction limited, we increased the beam diameter of the parallel beam by the factor of 2, and the beam size at the waist became two times smaller. The lens L2 is used to make the drive beam smaller in the Rb cell, where the pattern of drive field is spatially overlapped with the waist of the

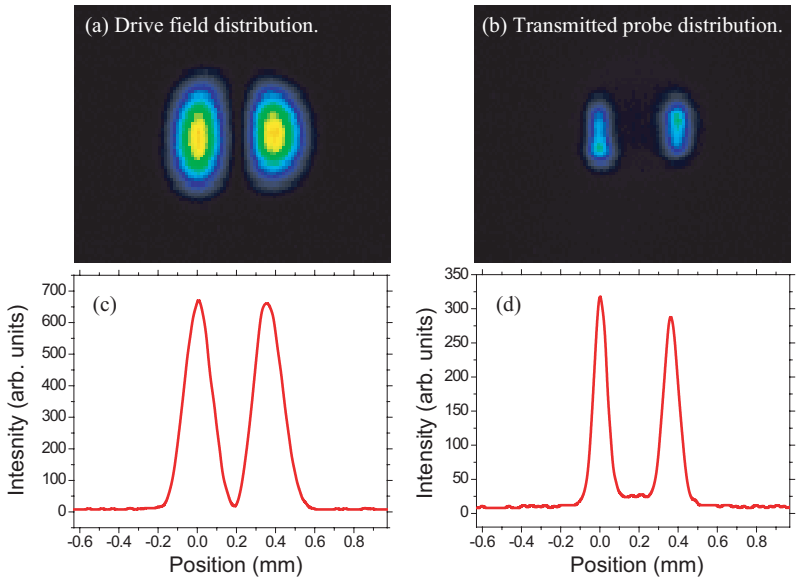

Fig. 26. The results of the experiment with the diffraction limited probe beam. Picture (a) shows the image of the intensity distribution of the drive field in the Rb cell. Picture (b) shows the image of the intensity distribution of the transmitted probe field. Curves (c) and (d) are the corresponding profiles. The widths of the peaks in curves (c) and (d) are 165 μm and 93 μm, respectively.

probe beam. Classically, there should be no structures at the waist of the probe beam because it is diffraction limited. Structures can be created in a region smaller than the diffraction limit in our experiment, however. The experimental result is shown in Fig. 26. The drive field still has a double peak intensity distribution (Fig. 26(a)). The transmission of the diffraction limited probe beam also has a double-peak intensity distribution as shown in Fig. 26(b). Curves (c) and (d) are the beam profiles of the drive and transmitted probe beams respectively. The width of the peaks in the drive beam is 165 μm, and the width of the peaks in the transmitted probe beam is 93 μm. The finesse of the transmitted probe beam is 1.8 times greater than that of the drive beam. For the probe beam, the structure created within the diffraction limit has a size characterized by the width of peaks (93 μm). This characteristic size is 5 times

smaller than the size of the diffraction limited probe beam (500 μm, see the spot of Fig. 24(C)).

Thus, we have demonstrated that our concept works in Rb vapor. Although the diffraction limit is "beaten," the experiment does not violate any laws of optics. The probe beam is diffraction limited, but the atoms are much smaller than the size of diffraction-limited beam.

Moreover, due to the strong nonlinearity of the EIT, the characteristic size of the pattern in the transmitted probe beam is much smaller than that of the drive beam and the diffraction limit of the probe beam.

3. Dependence on detuning

We have also measured the narrowing effect vs. the detuning of the probe field and have performed simulations using the density matrix approach. The results are shown in Fig. 27. We plot the narrowing factor (red curves) as a function of the detuning. The black dash curves are the EIT peaks as a reference. The left figure is the experimental data and the right figure is the simulation. The calculated results have a very good agreement with the experimental results.

The dependence on detuning has not been considered in [73, 74, 93, 94]. It is unique for our approach and can be understood in the following way. In the cases where we have a small detuning ($\omega \neq 0$), the absorption by the atomic medium given by Eq.(4.24) with a drive intensity distribution given by Eq.(4.25) can be written as

$$\kappa = \eta \frac{\gamma_{cb} + i\omega}{(\gamma_{ab} + i\omega)(\gamma_{cb} + i\omega) + |\Omega_0|^2[1 - (\frac{x_b - x_0}{L})^2]}, \tag{4.38}$$

Consider $|\Omega_0|$ is strong and $\gamma_{ab}\gamma_{cb}$, ω^2 are small, the real part of the absorption

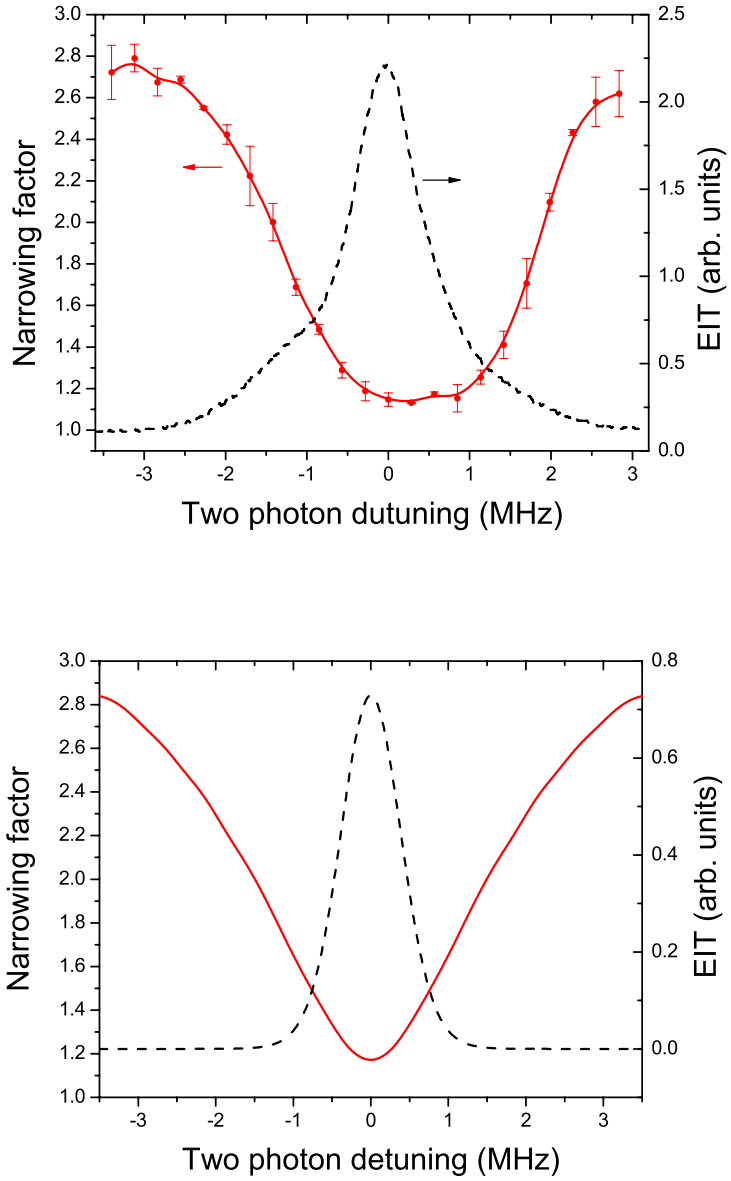

Fig. 27. Narrowing of the transmitted probe intensity distribution as function of the probe detuning: (a) experimental results (a) and (b) theoretical simulation. The transmitted probe profile is shown as well.

coefficient can be written as

$$\begin{aligned}
\mathrm{Re}(\kappa) &= \eta\frac{\gamma_{cb}(\gamma_{ab}\gamma_{cb}-\omega^2+|\Omega_0|^2[1-(\frac{x_h-x_0}{L})^2])+(\gamma_{ab}+\gamma_{cb})\omega^2}{(\gamma_{ab}\gamma_{cb}-\omega^2+|\Omega_0|^2[1-(\frac{x_h-x_0}{L})^2])^2+(\gamma_{ab}+\gamma_{cb})^2\omega^2} \\
&\simeq \eta\frac{\gamma_{cb}|\Omega_0|^2[1-(\frac{x_h-x_0}{L})^2]+(\gamma_{ab}+\gamma_{cb})\omega^2}{|\Omega_0|^4[1-(\frac{x_h-x_0}{L})^2]^2} \\
&\simeq \eta\frac{\gamma_{cb}}{|\Omega_0|^2}[1+(\frac{x_h-x_0}{L})^2]+\eta\frac{(\gamma_{ab}+\gamma_{cb})\omega^2}{|\Omega_0|^4}[1+2(\frac{x_h-x_0}{L})^2] \\
&= \eta[\frac{\gamma_{cb}}{|\Omega_0|^2}+\frac{\gamma\omega^2}{|\Omega|^4}+(\frac{\gamma_{cb}}{|\Omega_0|^2}+2\frac{\gamma\omega^2}{|\Omega|^4})(\frac{x-x_0}{L})^2], \qquad (4.39)
\end{aligned}$$

where $\gamma=\gamma_{ab}+\gamma_{cb}$. Then, the ratio of the width of the probe intensity distribution to the width of the drive intensity distribution is given by

$$R=\frac{L}{\Delta x}=\sqrt{\eta z\left(\frac{\gamma_{cb}}{|\Omega|^2}+2\frac{\gamma\omega^2}{|\Omega|^4}\right)}. \qquad (4.40)$$

From this we see that the finesse increases with the detuning.

In conclusion, we have performed a proof-of-principle experiment that our concept works in Rb vapor and have experimentally demonstrated the possibility of creating structures having widths smaller than those determined by the diffraction limits of the optical systems. The results obtained here can be viewed as an experimental verification of our approach, as well as evidence supporting the theoretical predictions and results obtained by others [73, 74, 93, 94]. The challenges associated with pushing our method to the subwavelength regime are formidable. In our experimental situation, transit-time broadening is the dominant dephasing mechanism that limits the smallness of the region in which a dark state can be formed. Solid-state systems may be more appropriate than a gas. Perhaps the most difficult aspect is devising a way to observe subwavelength structures. This technique might be used in microscopy by studying the distribution of molecules with subwavelength resolution or in lithography by manipulating molecules in the excited state. Also, note that it

may be possible to apply this approach to coherent Raman scattering (for example, CARS). This may improve the spatial resolution of CARS microscopy.

CHAPTER V

INTENSITY CORRELATION OF ATOMIC EXCESS NOISE IN A COHERENT MEDIUM

The intensity noise of optical fields increases dramatically when the fields interact with a resonant atomic vapor, the induced noise is referred to atomic excess noise [96, 97, 98]. One of the characteristics of diode lasers is that the output intensity is generally very stable while the frequency fluctuation is relatively large. It has been shown that the diode laser driven by a stable current source can have the intensity fluctuation less than the shot-noise level [99]. When the laser field from a diode laser interacts with an atomic vapor, especially on the resonance, the frequency or phase noise in the field is converted into the intensity noise [100, 101, 102] through the field-atoms interaction. The frequency noise to intensity noise conversion is one of the processes contributed to the atomic excess noise. Another possible process is the four-wave mixing involving the laser field and vacuum side modes [103]. Despite being referred to noise, the atomic excess noise has been studied early as a useful spectroscopic tool [98, 104] for high resolution spectroscopy rather than a source of noise. Yet it is a major noise and not desirable in many atom-optical-based applications such as atom-optical magnetometers, atomic clock [105], and the generation of squeezed light [105, 106, 107, 108, 109, 110].

As an example, improving the sensitivity of magnetometers is important both for practical applications and for fundamental research. Motivated by the potential applications to precision magnetometry [111, 112, 113, 114], researchers have extended a great interest in nonlinear magneto-optical effects [115, 116] in coherent media. Magnetometers based on atom-optical techniques, such as the optical pumping magnetometers [117] and the nonlinear magneto-optical rotation (NMOR) mag-

netometers [113, 114, 115, 118, 119], have achieved sensitivities of the order of 10^{-15} $\mathrm{THz}^{-1/2}$. Quantum noise starts to play a crucial role in obtaining higher sensitivity approaching the atom shot-noise-limited sensitivity [115, 119]. Coherent effects such as the squeezing of fields can be used to reduce the noise level below the shot-noise level. Several schemes for squeezing fields have been studied in EIT [120, 121, 122] as well as in nonlinear polarization self-rotation [107, 108, 109, 123]. However, it has been demonstrated that the atomic excess noise can reduce the squeezing of fields [109]. The addition of excess noise to atom-optical experiments needs to be taken into account in approaching the better performance, higher sensitivity in the case of magnetometers.

To reduce or eliminate the influence of atomic excess noise, one can take advantage of the intensity correlation properties of the optical fields passing through an atomic vapor. The strong coupling of optical fields in Λ-type atoms induces the intensity correlation or anti-correlation between two optical fields under certain conditions. In an EIT experiment performed by coupling two beams from one laser with an excited state and Zeeman sublevels of the ground state in a rubidium vapor, the intensity correlation and anti-correlation between two circularly polarized laser beams have been observed [124]. More generally, two laser beams from two independent lasers can realize the similar effect [125]. The intensity correlation has also been studied in NMOR experiments [126]. In the case of correlation or anti-correlation, the intensity noise in each of two laser fields is fluctuating with a phase difference of 0 or π. A simple summation or subtraction of these two signals can suppress or even eliminate the noise.

In this chapter, we study the intensity correlation of atomic excess noise in both EIT [127] and NMOR [128]. The study of power spectra of intensity fluctuations in both EIT [127] and NMOR [129] shows the possibility to reduce the atomic excess

noise and helps to find out the best working conditions for reducing noise.

A. Intensity correlation and noise spectra in EIT *

Recently the time-dependent intensity correlation function of two optical fields propagating through a dense rubidium vapor has been studied under the condition of EIT [124]. In this experiment, the intensity fluctuations of the output beams are highly correlated at two-photon resonance and anti-correlated when a two-photon detuning is introduced. The transition from correlation to anti-correlation of fields was observed as the two photon detuning changes. Using a similar setup, we now study the spectral dependence of the atomic excess noise and the correlation of noise. The noise will be analyzed in the frequency domain by using a spectrum analyzer. We also demonstrate that the subtraction of two correlated laser beams can suppress the noise to the shot-noise level.

1. Experiment of noise correlation in EIT

The schematic of experimental setup is presented in Fig. 28. An extended-cavity diode laser (ECDL) described in [130] is used as the laser source. The laser beam with the diameter of 0.1 cm is linearly polarized after an optical isolator which reduces the stray optical feedback from the optical elements of the setup. The spectral width of the laser emission is less than 1 MHz. The laser is tuned to the center of the Doppler broadened optical transition $5S_{1/2}$ (F=2) $\rightarrow$ $5P_{1/2}$(F=1) of ^{87}Rb (D1 line, λ=795 nm). The Doppler-free saturation resonance in the Rb reference cell is used as a frequency reference. After a warming-up time of 3 hours or longer, the laser

*Part of the data reported in this section is reprinted with permission from "*Power spectra and correlations of intensity fluctuations in electromagnetically induced transparency,*" by V.A. Sautenkov, H. Li *et al.*, J. Mod. Opt. **54**, 2451 (2007), Copyright by Taylor & Francis Group.

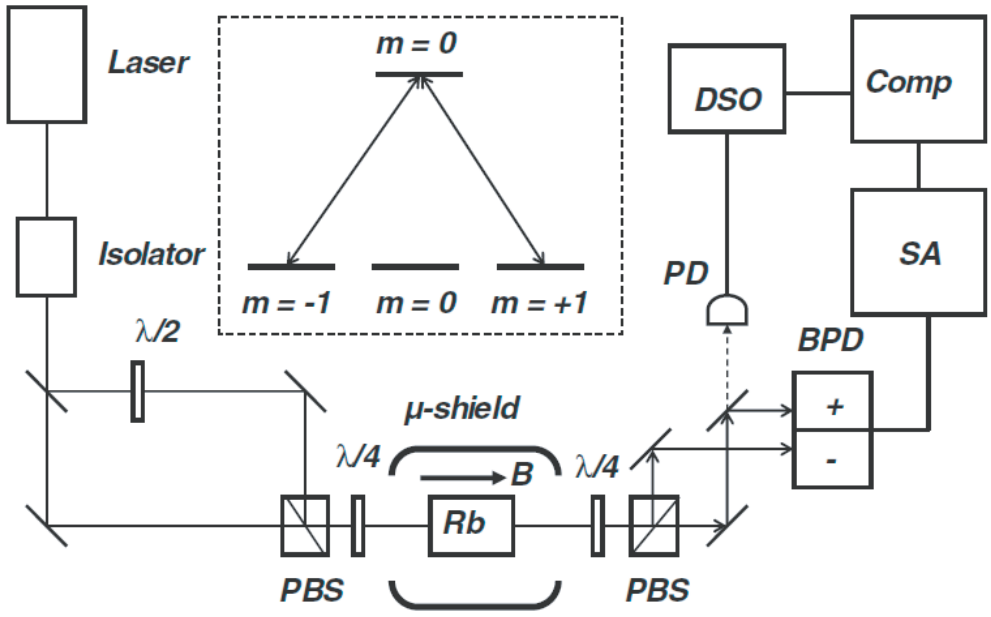

Fig. 28. Experimental setup of intensity correlation in EIT and simplified energy level scheme of rubidium atoms. PBS is the polarizing beam splitter, $\lambda/2$ and $\lambda/4$ are retardation wave plates, PD is the photo-detector, BPD is the balanced photo-detector assembly, DSO is the digital storage oscilloscope, SA is the spectrum analyzer and COMP is the computer.

frequency drift is less than 30 MHz per hour in our laboratory and this passive laser stability is acceptable for our measurements. To study EIT in Rb vapour the output laser beam is modified. The first laser beam is split and a retardation $\lambda/2$ wave plate is used to rotate the linear polarization of one beam by 90°. The orthogonally linearly polarized beams are combined together by a polarizing beam splitter (PBS). After the $\lambda/4$ wave plate the laser beams are sent to a glass cell with Rb atomic vapor at the density of 10^{-12} cm^{-3}. Combination of two orthogonally circularly polarized optical fields produces a ground state Zeeman coherence in Rb atoms and generates EIT. A simplified Λ-scheme is shown in the inset of Fig. 28. To avoid the contribution of environmental magnetic field the Rb cell is installed in a two-layer magnetic shield.

The transmitted optical fields with orthogonal polarizations are separated using a second $\lambda/4$ wave plate and another PBS. Then the optical beams are sent to the data acquisition system including photodiodes, oscilloscope and spectrum analyzer.

2. Experimental results and discussion

In order to measure the transmission, one of the beams after PBS is sent to a narrow bandwidth photo-detector (PD) (a mirror installed in a removable indexing mount to make the switch) and the signal from the photo-detector is recorded by a digital storage oscilloscope (DSO). The recorded EIT resonances for two different laser powers are shown in Fig. 29. Two-photon detuning is controlled by changing the longitudinal magnetic field B. In our case the two photon detuning is equal to the Zeeman magnetic splitting $\Delta\omega(F = 2) = 2\pi \times 1.4$ MHz/G. We have scan the longitudinal magnetic field at the frequency of 10 Hz. The width of the EIT resonance (FWHM) increases with the optical power (Rabi frequency) and it is less than the natural width of the optical transition 6 MHz. The power dependence of EIT width is shown in Fig. 31(a) and will be discussed later.

Spectral distribution of the excess noise is studied at the maximum transparency when the magnetic field B=0. Two fast photo-detectors with bandwidth 100 MHz are used to study intensity fluctuations of optical beams. The photo-detectors with opposite polarity (+) and (-) can be used separately or as a balanced photo-detector assembly (BPD) with the sensitivity of 2×10^4 V/W. The data acquisition system includes a radio frequency (RF) spectrum analyzer (Advantest R3162) and a computer with LabView software. The results in Fig. 30 are obtained under the same experimental conditions as those for EIT resonances in Fig. 29. The curves are recorded with the resolution of 300 kHz and video-band of 300 Hz. The electronics noise (dark noise) is extracted. Curves (1a) and (1b) in Fig. 30 are recorded with only one

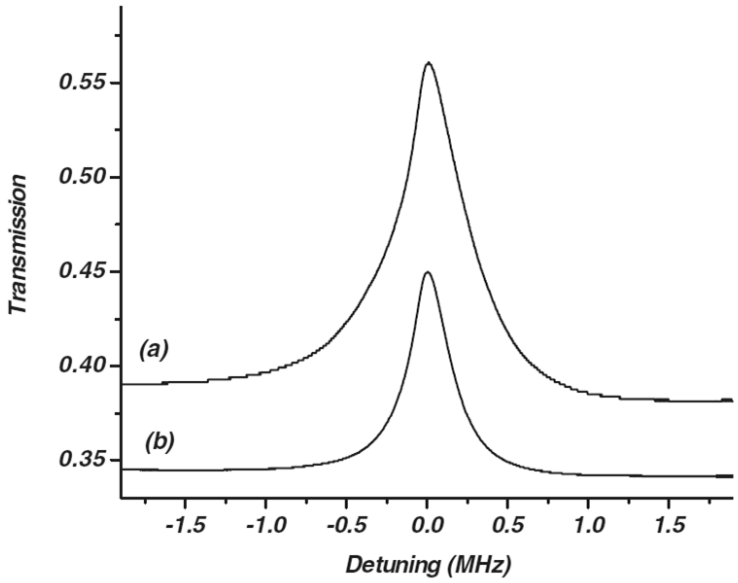

Fig. 29. The EIT resonances; (a) the power P_{in} of each beam at the cell is equal to 0.22 mW (total power P_t=0.44 mW), (b) P_{in}=0.11 mW (P_t=0.22 mW).

optical beam sent to the BPD. Curves (2a) and (2b) are recorded with both optical beams at BPD and the output signal is the subtraction of two beams. We also have recorded reference curves which is obtained when we remove the Rb cell from the optical path and reduce the optical powers at BPD by variable filters to the previous levels. The no-cell reference curves (3a) and (3b) are recorded with two beams in the subtraction scheme and they are close to the shot-noise-limited curves. There are small noise bumps in the low frequency region. This extra noise is associated with the gain of the registration system. We shall note that the diode laser has a very small intensity noise. When we have detected only one laser beam we have observed the same spectral distribution by taking into account a variation of the total optical power.

The intensity noise dramatically increases when optical fields propagate through

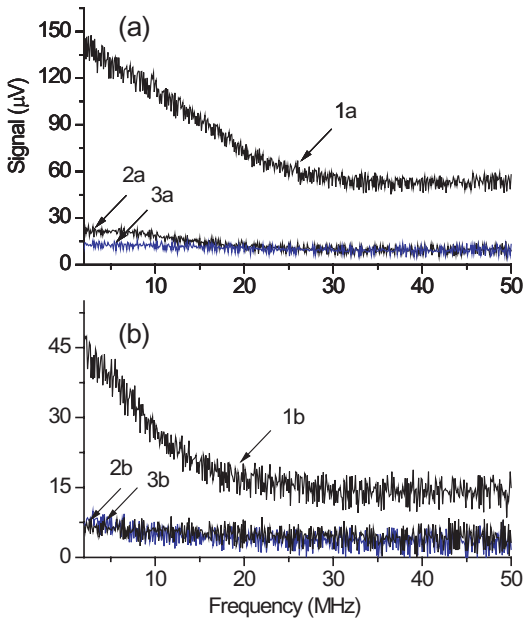

Fig. 30. Spectra of noise signal are recorded at power P_{in}=0.22 mW [set (a)] and P_{in}=0.11 mW [set (b)] under EIT conditions. Curves (1a) and (1b) are recorded with one laser beam sent to the photo-detector. Curves (2a) and (2b) are recorded with two beams at the balanced photo-detector assembly. Curves (3a) and (3b) are reference curves which were recorded without a Rb cell.

the Rb cell. The spectral distribution of the intensity fluctuations in one of the beams is presented in Fig. 30 as curves (1a) and (2b). The conversion of the laser frequency noise to the intensity noise in Rb atomic vapor enhances the intensity fluctuations. The spectra show a resonant behavior of the intensity fluctuations with a maximum at the low frequency and a flat background.

The correlation of the intensity fluctuation can be estimated when both optical beams are sent to the BPD. The difference in the signals is shown in Fig. 30(2a) and (2b). At the low optical power the correlation curve (2b) coincides with the reference curve (3b). At the high optical power there is a difference between the

subtracted correlation curve (2a) and the reference curve (3a). The correlation of the intensity fluctuation decreases with increasing optical power (Rabi frequency). Similar power behavior of correlations between two independent optical beams in the EIT experiment was observed in [125]. Variation in the correlation coefficient is explained in [125, 124] as a consequence of the competition between EIT and Raman processes. The result is that the best reduction of excess atomic noise in EIT can be reached at low optical intensity.

It is interesting that intensity fluctuations of coupled optical fields are highly correlated in a broader spectral range compared with EIT width.

The power dependence of the EIT width is presented in Fig. 31(a). The experimental data are shown as circles. The solid line in Fig. 31(b) is the result of a fit using expression $w = w_0 + kP$, where $w_0 = 0.07 \pm 0.02$ MHz and $k = 2.14 \pm 0.1$ MHz/mW. A linear dependence of EIT width on the moderate laser power was discussed earlier in [131]. The zero power limit of width w_0 is close to the calculated transient broadening $0.98 V_{th}/\pi D = 0.09$ MHz [43], where V_{th} is the thermal speed of an atom and D is the laser beam diameter. The estimated width w_0 is obtained by the linear intensity dependence which can be switched to nonlinear dependence at very low intensities. At the lowest laser beam power 0.048 mW we have measured an EIT width of 0.1 MHz which can be considered as the low power limit in our experiment.

The spectral distribution of intensity fluctuation is a combination of a resonant curve and a flat background. It is possible to fit the resonant part of the spectral distribution by the half Lorentzian function (half of a bell-shaped curve). In Fig. 30(1a) the amplitude drops to the half maximum at the frequency of 10.5 MHz. For curve (1b) it drops to the half at the frequency of 15.6 MHz. The noise width versus laser beam power P is presented in Fig. 31(b). The experimental data are shown as squares. The width is obtained from the Lorentzian fit of the noise spectral

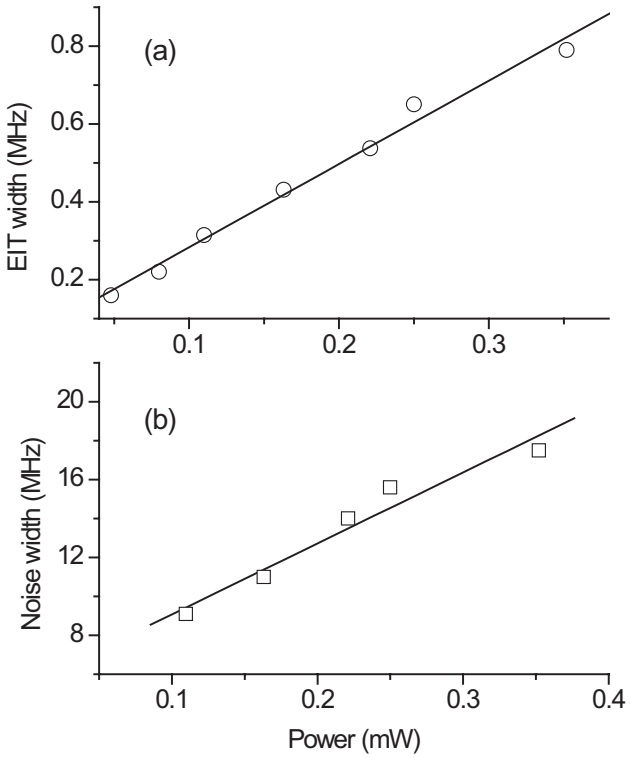

Fig. 31. Power dependence of (a) the width of the EIT resonance and (b) the width of the intensity noise spectrum. The solid lines are results of a linear fit.

distribution at different laser powers. The error bar is small, less than the size of the squares. The errors can be attributed to systematic errors in the power measurements and temperature (atomic density) drift. The solid line in Fig. 31(b) is the result of a fit to expression $W = W_0 + KP$, where $W_0 = 5.4 \pm 0.9$ MHz and $K = 36 \pm 3.9$ MHz/mW. The power dependence of the noise spectra can be associated with the spectral hole in the absorption due to the saturation of the optical transition and the re-population of the ground state levels [132, 133]. The results are consistent with previous studies of the time-dependent cross-correlation function for intensity fluctuations in the EIT experiment where a narrow correlation peak order of 20 ns

was observed [124].

To summarize this section, we have studied the spectral distribution and correlation of optical fields coupled the excited state and two ground state Zeeman sublevels in a dense rubidium atomic vapor. Under resonant EIT conditions, the intensity noise is highly correlated. The experiment has demonstrated that the atomic excess noise can be reduced to the shot-noise level by using the subtraction scheme. The results can be used to improve the performance of atomic clocks and magnetometers.

B. Intensity correlation in NMOR *

In the previous section, we have studied the correction between the fluctuations between the left and right circularly polarized beams, which are the normal modes of the system. However, the experimental configurations are slightly different in many atom-optical applications in optical magnetometry [115] measurements such as the NMOR experiment. We now study the correlation of intensity fluctuations in the configuration with two orthogonally linearly polarized beams, which are not the normal modes of the system.

In the first part of this section, we study the atomic noise correlation in a NMOR experiment with a rubidium vapor and the dependence of the correlation function on the longitudinal magnetic field. In the second part, we study the noise spectra in the same configuration and demonstrate the reduction of the atomic excess noise under proper conditions. In the final part, a simple theoretical model is presented.

---

*Part of the data reported in this section is reprinted with permission from "*Intensity correlations in resonance nonlinear magneto-optical rotation,*" by T.S. Varzhapetyan, H. Li *et al.*, Opt. Comm. **282**, 39 (2009), Copyright by Elsevier; and from "*Atomic noise spectra in nonlinear magneto-optical rotation in a rubidium vapor,*" by H. Li *et al.*, J. Opt. Soc. Am. B **25**, 1702 (2008), Copyright by Optical Society of America.

1. Experiments of atomic excess noise in NMOR

The experimental schematic is illustrated in Fig. 32. The laser source is an external cavity diode laser (ECDL) described in [130]. The laser is tuned to the rubidium D_1 line (795 nm), specifically at the transition $5S_{1/2}$ (F=2) $\leftrightarrow$ $5P_{1/2}$ (F=1) of ^{87}Rb, referenced to the Doppler-free saturation resonance in a rubidium cell at room temperature. The frequency drift is less than 30 MHz per hour after a sufficient warm-up time. The linewidth of the laser emission is less than 1 MHz. The laser beam has a diameter of 1 mm, and it is linearly polarized. After passing through an optical isolator, the beam proceeds through a polarizing beam splitter (PBS) and possesses a polarization parallel to the optical table.

The beam goes into a glass cell filled with a rubidium vapor that contains the natural isotope abundance of rubidium atoms. The cell has the length of 7.5 cm, and it is heated to reach an atomic density of 10^{12} cm^{-3}. A two-layer magnetic shield isolates the cell from environmental magnetic fields in the lab, while a solenoid inside the magnetic shield provides an adjustable longitudinal magnetic field. The linearly polarized beam is a combination of the left- and right-circularly polarized components. The two circular components are coupled to the energy levels of ^{87}Rb as shown in the energy diagram in Fig. 32(c).

To study the polarization rotation and the correlation of noise, the output beam from the rubidium cell is analyzed by a half-wave plate ($\lambda/2$) and two identical fast photo-detectors (block (a) in Fig. 32) with a frequency bandwidth of 75 kHz - 1.2 GHz. The optical path lengths for both beams and the length of cables between the photo-detectors and the oscilloscope are chosed to be the same to avoid any time delay between the signals in two registration channels. The half-wave plate is set to rotate the polarization by 45°, such that without the rubidium cell, the PBS equally splits

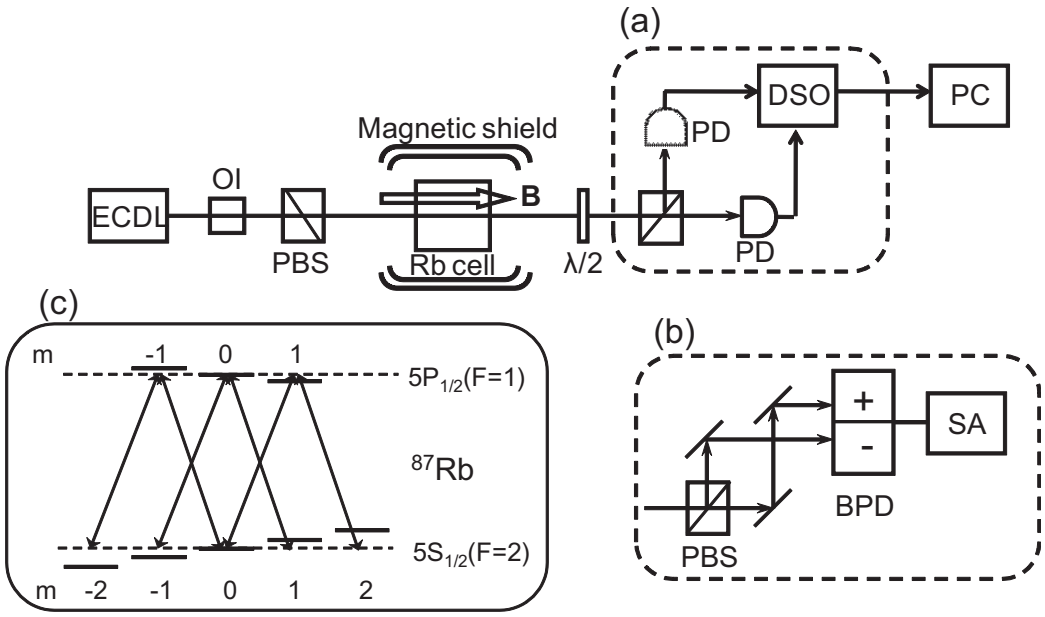

Fig. 32. Experimental setup of noise study in NMOR and the energy levels of rubidium atoms. (a) is the detection setup for measuring the correlation of noise, (b) is the detection setup for measuring the noise spectra, (c) is the energy diagram. The notations are the following: OI is an optical isolator; PBS is a polarizing beam splitter; DSO is a digital storage oscilloscope; PDs are photo-detectors; BPD is a balanced photo-detector; SA is a spectrum analyzer.

the intensity of the beam. If the rubidium cell is placed in the system, a rotation angle of the beam polarization will be introduced that depends on the magnitude of the longitudinal magnetic field [115]. With a nonzero magnetic field (B≠0), the two beams coming out from the PBS do not have equal intensities. Recording the intensities of two beams as I_1 and I_2, the polarization rotation due to rubidium atoms can be calculated using the following equation

$$\phi = \frac{1}{2}\arcsin\left(\frac{I_1 - I_2}{I_1 + I_2}\right) . \tag{5.1}$$

We can also calculate the correlation function of two beams from the recorded intensities.

To study the power spectra of the atomic excess noise, a balanced photo detector (BPD) with a sensitivity of 2×10^4 V/W and a bandwidth from DC to 100 MHz is used to register the intensities of two laser beams (block (b) in Fig. 32). The signal is analyzed by an RF spectrum analyzer. In the case of a zero magnetic field (B=0), for example, each channel of the BPD records an intensity

$$I_i = I_0 + I(t) + \delta I_i(t) \ , \ (i = 1, 2) \ , \tag{5.2}$$

where I_0 is the average intensity, $I(t)$ is the low frequency intensity fluctuations due to the instability of the laser source such as the fluctuations of temperature and current, and $\delta I_i(t)$ is the atomic excess noise due to the interaction between the laser beam and the atoms. Then, the difference signal ΔI from the BPD is given by $\Delta I(t) = \delta I_1(t) - \delta I_2(t)$. The spectrum analyzer gives the Fourier transform of the time dependence of the signal.

2. Intensity correlation in NMOR

In this part, we present the measurements of the intensity correlation function in NMOR. We start the presentation of experimental results with a demonstration of the narrow EIT resonance. The transmission T versus magnetic field B is shown in Fig. 33(a). In a magnetic field, the linear polarization of the laser field rotates, and the polarization rotation dependence on the external magnetic field is shown in Fig. 33(b). The width of nonlinear magnetic optical resonances is determined by the power broadening of the two-photon transition, which for our conditions is narrower than the natural optical width (6 MHz). The observed background in Fig. 33(b) is due to the linear rotation of polarization.

To study the fluctuations of an optical field transmitted through a dense Rb vapor, we have registered the time dependent signal fluctuations $\delta S_{1,2}(t)$ of the two

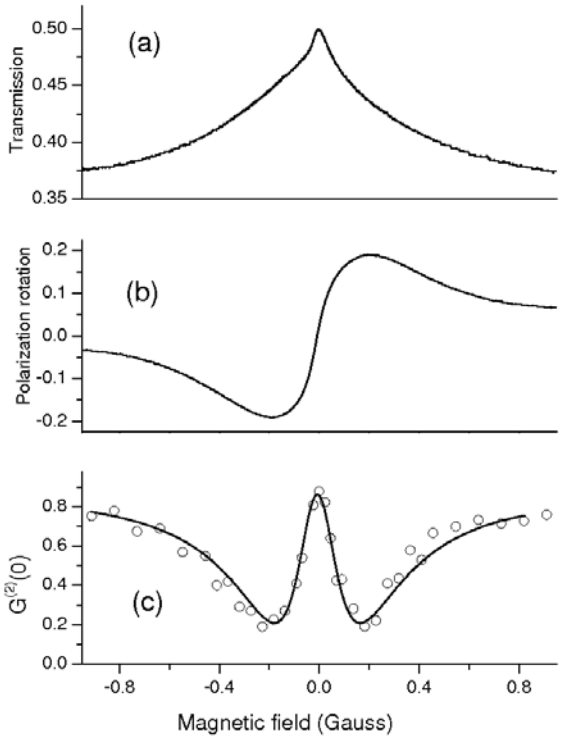

Fig. 33. Magnetic field dependence of the EIT (a), polarization rotation (b) and correlation function $G^{(2)}(0)$ (2b). In (c) the circles represent experimental data and the solid curve is a visual guide for the eye.

optical beams after the second PBS. We record these signal fluctuations for the two output beams in a 10 μs time-window for different magnetic fields, and then we calculate the normalized correlation functions given by

$$G^{(2)}(\tau) = \frac{\langle \delta S_1(t) \delta S_2(t+\tau) \rangle}{\sqrt{\langle [\delta S_1(t)]^2 \rangle \langle [\delta S_2(t+\tau)]^2 \rangle}}, \tag{5.3}$$

where $\delta S_{1,2}(t)$ are the time dependent fluctuations of the two beams, and stochastic averaging [1] denoted by angular brackets is defined as $\langle Q(t) \rangle \equiv 1/T \int_t^{t+T} Q(t')dt'$.

The intensity fluctuation is very low when the cell has been removed from the laser beams due to the fact that the diode laser radiation possesses low intensity noise. In the presence of a resonant medium, however, the situation changes, and the phase noise of a diode laser is transformed into intensity fluctuations. The laser beams then possess significant intensity noise. The study shows that the intensity noise of two beams can be well correlated depending on the magnetic field. The magnetic field dependence of the correlation function at zero time delay, $G^{(2)}(0)$, is shown in Fig. 33(c). The correlation magnitude is close to 0.9 at zero magnetic field.

Increasing the magnetic field up to 0.2 G results in decreasing the correlation function magnitude to about 0.2. But further increase of the magnetic field leads to a revival of the correlation, and it reaches about 0.7 at 0.8 G field strength. We underline here that this behavior is different from that observed in [124]. The key difference is that, in this experiment, we study the fluctuations of the orthogonal linear polarization components, which are not normal modes because of the Faraday effect. Unlike the experiment in EIT, no anti-correlation is observed in this experiment.

By examining the polarization angle rotation dependence shown in Fig. 33(b), one can conclude that the maximum correlation is obtained when the magnetic field and the polarization rotation in the atomic medium are close to zero. The correlation functions $G^{(2)}(\tau)$ for three different magnetic fields are shown in Fig. 34.

The signals from the photo-detectors in the time interval of 200 ns are shown in the inset boxes in Fig. 34. The signals are proportional to the laser beam power with a slope of 500 V/W. The vertical range of the plot is 4 mV. The amplitude variations of the signals are practically the same as in Fig. 34.

The temporal behavior of the signal is modified by the applied magnetic field. The signals shown in Fig. 34(a) and (c) are correlated, and the ones shown in Fig. 34(b) are not. We observe that at a low or high magnetic field, fluctuations

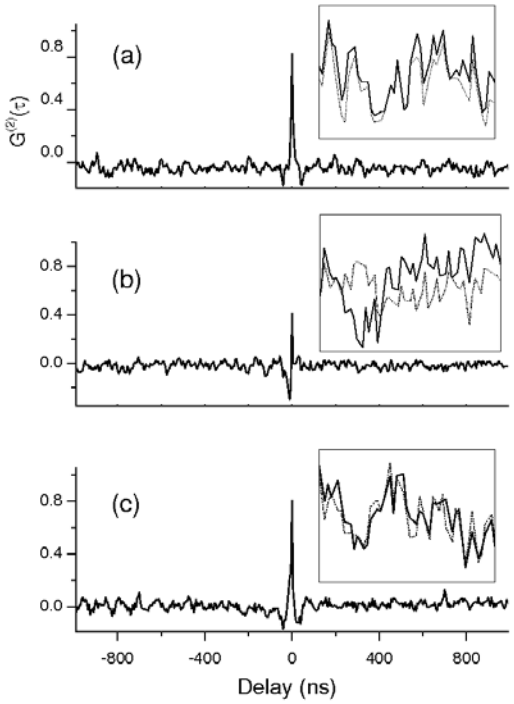

Fig. 34. Intensity correlation function $G^{(2)}(\tau)$: curve (a) recorded at zero magnetic field, curve (b) at a magnetic field of 0.18 G and curve (c) at a magnetic field of 0.9 G. Also signals from photo-detectors are shown in boxes. The waveforms are recorded in time intervals of 200 ns and amplitude intervals of 4 mW.

are strongly correlated. At an intermediate magnetic fields, the peaks of correlation function have less magnitude. The correlation function behaves as if it changes sign around zero time delay. Possibly different frequency components of the signals can be correlated or anti-correlated at these magnetic fields. For the dependence shown in Fig. 33(c), we have selected the magnitudes of the correlation function at zero time delay.

We note that the inverse width of the peaks is the order of $2\pi \times 20$ MHz, and

it is comparable with the width of the saturation resonance [132, 133, 134], and it is much broader than the ground state relaxation rate. The inverse width depends on the excited state decay rate $2\pi \times 6$ MHz and the optical excitation rate. The influence of one-photon optical saturation on MNOR is discussed in [115].

To summarize the results, we have studied atomic noise correlations in a nonlinear magneto-optical rotation experiment with rubidium atomic vapor by using broadband detection. The correlations between the orthogonally polarized components of the laser beam are maximal in the absence of a magnetic field. The width of the correlation function peak is proportional to the excited state lifetime and the inverse Rabi frequency. When a longitudinal magnetic field is applied, the correlations first decrease and then increase. The minimal correlations and the maximal rotation angles are observed at the same magnetic fields. The performed study is important for understanding of noise properties of radiation interacting with the Lambda-type atomic systems that demonstrate a variety of quantum coherence effects.

3. Atomic noise spectra in NMOR

In this part, we present the measurements of atomic noise spectra in NMOR. We begin the presentation of the results by showing the power spectra of noise with no magnetic field (B=0). Fig. 35 shows the noise spectra for different input laser intensities. The left and right figures display the spectra for input laser powers of 0.24 mW and 0.49 mW, respectively. Traces (a2) and (b2) are recorded with two laser beams sent to the BPD, and they show the noise spectra of the difference signal. The noise is larger in the low frequency region. The noise level approaches the shot-noise level at higher frequencies.

The expected shot-noise levels are indicated as the red dashed lines in Fig. 35. Note that the shot-noise in NMOR includes the spin shot-noise and the photon shot-

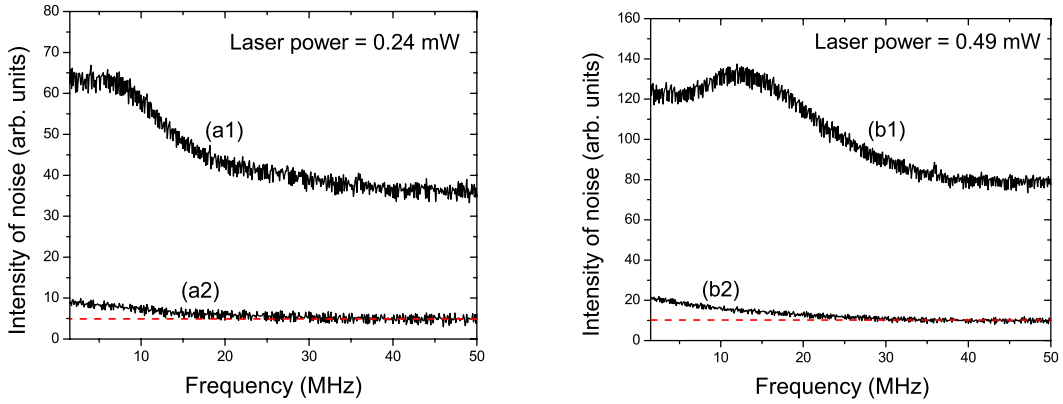

Fig. 35. The power spectra of the noise from laser beams in an NMOR experiment with the magnetic field B=0. The left and right figures show the spectra with input laser powers of 0.24 mW and 0.49 mW, respectively. Traces (a1) and (b1) are the noise spectra of one laser beam. Traces (a2) and (b2) are the noise spectra of the balanced signal (with both beams). The red dashed lines indicate the expected shot-noise level. The spectrum analyzer was setup with a resolution of 300 kHz and a video bandwidth of 100 Hz.

noise [113, 115], in our experiment the photon shot-noise dominates and determines the shot-noise level. As discussed in [127], the photon shot-noise level is experimentally determined by sending one or two laser beams to the BPD without passing through the rubidium cell. In this case the photon shot-noise is proportional to the square root of the laser power.

For comparison, traces (a1) and (b1) are recorded with only one laser beam sent to the BPD. They represent the noise spectra of the laser beam passing through the rubidium vapor. Before entering the cell, the laser beam has small intensity noise but large phase noise. The phase noise is converted into the intensity noise due to the laser interacting with the atoms. This process causes a substantial increase of intensity fluctuations in the laser beam coming out of the cell [98]. Our results show

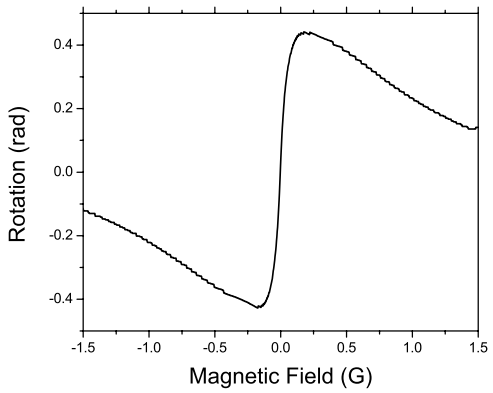

Fig. 36. The polarization rotation is plotted as a function of the longitudinal magnetic field B.

that these intensity fluctuations can be suppressed by subtracting the intensity of one laser beam from the other. Comparing the noise spectra of one laser beam and of the difference signal, (a1) and (a2) for instance, the noise level of the difference signal is dramatically reduced. When the input laser power is doubled (0.49 mW), the corresponding spectra presented as (b1) and (b2) show the same behavior, although the shot-noise level increases approximately two times because of the higher laser power. These results can be understood as a consequence of the intensity correlation between the two output laser beams from the PBS. As is shown in [128], the intensities of two beams in an NMOR experiment are highly correlated (correlation function $G^{(2)}(0) \approx 0.9$) at zero magnetic field (B=0). The fluctuations $\delta I_1(t)$ and $\delta I_2(t)$ are varying simultaneously, and thus $\Delta I(t)$ will be small.

The intensity correlation and the substantial reduction of noise in NMOR experiments is not trivial in terms of various behaviors at different magnitudes of the magnetic field B. To show this, besides the preceding results with a zero magnetic field, we have also studied the noise spectra in NMOR at magnetic fields of various

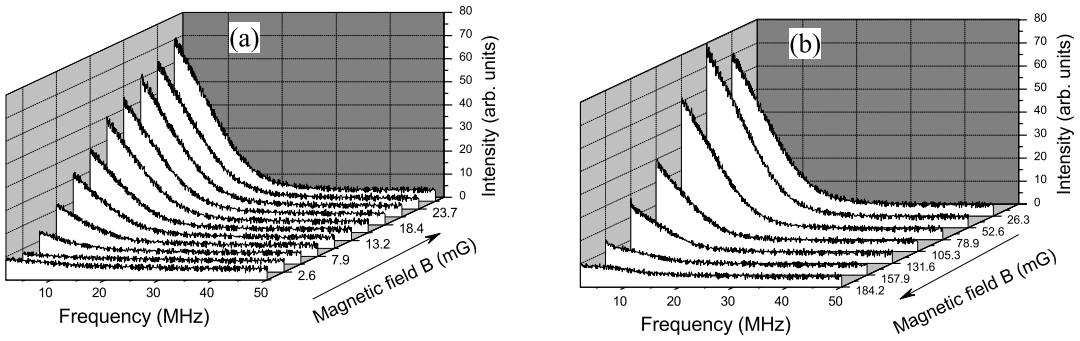

Fig. 37. The noise spectra dependence on the longitudinal magnetic field. The noise level is plotted as a function of both the frequency and the magnetic field. (a) The spectra corresponding to magnetic fields ranging from 0 to 26.3 mG; (b) The the spectra corresponding to magnetic fields ranging from 26.3 mG to 184 mG. The arrows denote the ascending direction of the magnitude of the magnetic field.

magnitudes. Prior to showing these results, a typical measurement of the polarization rotation in our experiment (laser power P=0.24 mW) is presented in Fig. 36, to remind us of the rotation dependence on the magnetic field.

We record the noise spectra of the difference signal with two output beams sent to the BPD for several magnetic fields. The results are presented as three dimensional plots in Fig. 37 (laser power P=0.24 mW). The magnetic field varies from 0 to 184 mG. The spectra corresponding to magnetic fields ranging from 0 to 26.3 mG are shown in plot (a), and the ones corresponding to magnetic field ranging from 26.3 mG to 184 mG are shown in plot (b). The spectra are sorted by the magnetic field ascending along the arrows shown in the figure. The magnetic field in plot (a) steps by about 2.6 mG, while it steps by about 26 mG in plot (b). Note that the noise spectra corresponding to negative magnetic fields, which are not plotted here,

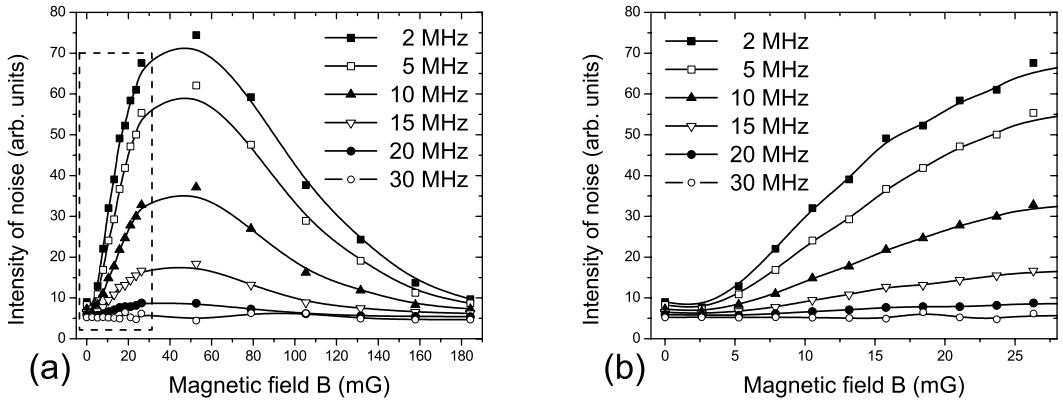

Fig. 38. (a) The level of noise at different frequencies is plotted as a function of the magnitude of the magnetic field. (b) The magnification of the dashed square region in (a). Different symbols denote different frequencies. Square: 2 MHz; hollow square: 5 MHz; triangle: 10 MHz; hollow triangle: 15 MHz; dot: 20 MHz; circle: 30 MHz. The solid lines are smooth connections of the data points.

have the symmetric behaviors. From these results, we see that the reduction of high frequency noise is nearly the same for different magnetic fields, but the low frequency noise is not appreciably reduced. This shows that the low frequency noise is not correlated at all magnitudes of the magnetic field, but the high frequency noise is better correlated. A detailed study of the noise spectra dependence on the magnetic field for each individual NMOR system can provide a guideline for choosing optimal working parameters to reduce or eliminate the atomic excess noise.

To better demonstrate how the noise at a certain frequency depends on the magnitude of the magnetic field, we cut the three dimensional plots in Fig. 37 at specific frequencies along the plane of the magnetic field axis and the intensity axis. The cross sections picked up are shown in Fig. 38(a), in which the symbols square, hollow square, triangle, hollow triangle, dot and circle represent the level of noise at

frequencies of 2 MHz, 5 MHz, 10 MHz, 15 MHz, 20 MHz and 30 MHz, respectively. At the zero magnetic field, the noise is strongly reduced over the entire frequency range and at the high frequencies it is close to the shot-noise level. For the frequencies lower than 20 MHz, the noise level increases quickly within about 50 mG, and comes back close to the shot-noise level within about 130 mG. For the frequencies higher than 20 MHz, the noise level essentially remains close to the shot-noise level. To show the details of the rising slope in the dashed square in Fig. 38(a), a magnification of this region is shown in Fig. 38(b). For low frequency noise, the noise level remains nearly minimum value not only at the zero magnetic field but also in a small region around zero magnetic field. In our data, the noise level of 2 MHz and 5 MHz noise is almost flat for magnetic fields ranging from 0 to 2.5 mG.

These results show that, for the best reduction of atomic excess noise in atom-optical applications, one should work near a zero longitudinal magnetic field. However, a rigorously exact zero magnetic field is not necessary, because the same reduction of noise can be obtained in a region around zero magnetic field. This property makes the implementation relatively easier and more reliable. As an example, to obtain the best reduction of the atomic excess noise in NMOR magnetometers, one might use an external calibrated magnetic field to compensate [115], so that longitudinal magnetic field is close to zero.

To summarize the results, we have experimentally studied the noise spectra in a nonlinear magneto-optical rotation experiment in rubidium vapor. We have shown that a detailed study of noise reduction, due to the intensity correlation between two orthogonally polarized components of the laser beam, can suggest the optimal working conditions for reducing atomic excess noise. The noise in the difference signal of two orthogonal components at different frequencies has been studied as a function of magnetic field. The study of the noise dependence on both the noise

frequency and the magnetic field shows that the maximum reduction of noise can be obtained around zero longitudinal magnetic field. Our results can be used to reduce or eliminate atomic excess noise, and thus improve the sensitivity of magnetometers. The study also indicates the potential importance of the intensity correlations in other atom-optical applications such as atomic frequency references and the generation of squeezed light.

4. Theoretical description and discussion

This part presents a simplified theoretical description of our system treating the laser fields classically and using a density matrix for the atomic response. The laser beams are in resonance with a three-level medium as depicted in Fig. 39. The Hamiltonian of the atom is given by

$$H = \hbar\Omega_{-}|a\rangle\langle b| + \hbar\Omega_{+}|a\rangle\langle c| + h.c., \tag{5.4}$$

where $\Omega_{\pm} = \wp_{c,b}E_{\pm}/\hbar$ are the Rabi frequencies of left- and right-circularly polarized beams; $\wp_{c,b}$ and $E_{\pm}$ are the corresponding dipole moments of the atomic transitions and the electric fields. The density matrix equation is given by

$$\dot{\rho} = -\frac{i}{\hbar}[H,\rho] - \frac{1}{2}(\hat{\Gamma}\rho + \rho\hat{\Gamma}), \tag{5.5}$$

where $\hat{\Gamma}$ is the relaxation matrix. The equations for field propagation are

$$\frac{\partial\Omega_{-}}{\partial z} = -i\eta_b\rho_{ab}, \quad \frac{\partial\Omega_{+}}{\partial z} = -i\eta_c\rho_{ac}, \tag{5.6}$$

where $\eta_b = \nu_{-}N\wp_b^2/(2\hbar\epsilon_0 c)$, $\eta_c = \nu_{+}N\wp_c^2/(2\hbar\epsilon_0 c)$ are the coupling constants, $\nu_{\pm}$ are the frequencies of circular polarized fields, $\wp_{b,c}$ are the dipole moments of the corresponding transitions, N is the atomic density of medium. Note that the left- and right-polarized beams are the normal modes of the current system, and their

polarizations do not change while they are propagating through the cell.

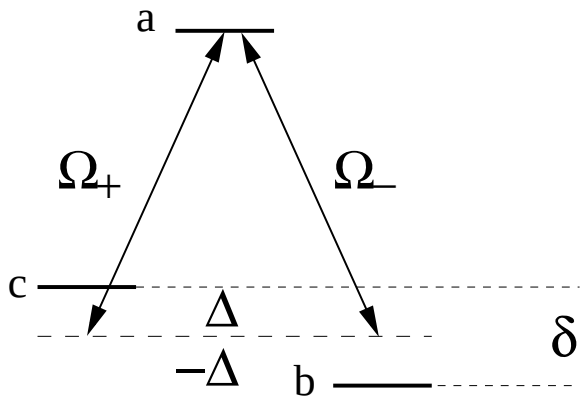

Fig. 39. A simplified three-level scheme. Splitting of the ground state is $\omega_{cb} = 2g\mu_B B$, where g is the Lande factor, μ_B is Borh's magneton, and B is the magnetic field.

The intensities of the optical beams propagating through the cell fluctuate. The corresponding correlation function is defined as

$$G^{(2)}(\tau) = \frac{\langle \delta I_-(t)\delta I_+(t+\tau)\rangle}{\sqrt{\langle[\delta I_-(t)]^2\rangle\langle[\delta I_+(t+\tau)]^2\rangle}}. \tag{5.7}$$

Intensity fluctuations have been studied in [124], and they are related to the atomic responses

$$\delta I_- \sim \mathrm{Im}\rho_{ab}\Omega_-^*, \quad \delta I_+ \sim \mathrm{Im}\rho_{ac}\Omega_+^*. \tag{5.8}$$

The corresponding atomic coherences in the three-level system can be found from the solution of the density matrix equations. Assuming the phase diffusion of optical fields is a slow process, the atomic coherences are given by

$$\rho_{ab} = -i\frac{n_{ba}\Omega_- + \rho_{cb}\Omega_+}{\Gamma_{ab}}, \quad \rho_{ca} = i\frac{n_{ca}\Omega_+ + \rho_{cb}\Omega_-}{\Gamma_{ca}} \tag{5.9}$$

$$\Gamma_{cb}\rho_{cb} = i\rho_{ca}\Omega_- - i\rho_{ab}\Omega_+, \tag{5.10}$$

where $\Gamma_{ab} = \gamma_{ab} + i(\omega_{ab} - \nu_-)$; $\Gamma_{ca} = \gamma_{ca} - i(\omega_{ac} - \nu_+)$; $\Gamma_{cb} = \gamma_{cb} + i(\omega_{cb} - \nu_- + \nu_+)$; and

γ_{ab}, γ_{ca} are the relaxation rates for atomic coherence at optical transitions, γ_{cb} is the relaxation rate for atomic coherence between magnetic sublevels (for $\gamma_{ab}, \gamma_{ca} \gg \gamma_{cb}$, $\gamma_{ab} = \gamma_{ca} = \gamma$); $n_\alpha = \rho_{\alpha\alpha}$; $n_{\alpha\beta} = \rho_{\alpha\alpha} - \rho_{\beta\beta}$; $\omega_{\alpha\beta}$ are the atomic frequencies; α and β are labels for atomic levels a, b, c; $\nu_-(t) = \nu_+(t)$ are the instantaneous frequencies of laser radiation in both beams having orthogonal polarizations. Assuming $\Omega_- = \Omega_+ = \Omega$, and defining $\delta = \omega_{ab} - \nu_- - \omega_{cb}/2$, we solve Eq. (5.10) with respect to ρ_{cb}. Then, substituting the solution into Eqs. (5.9) gives us the following:

$$\rho_{ab} = i\frac{\Gamma_{cb}(\Gamma - i\delta)n_{ab} + n_{cb}\Omega^2}{\Gamma_{cb}(\delta^2 + \Gamma^2) + 2\Gamma\Omega^2}\Omega, \tag{5.11}$$

$$\rho_{ca} = i\frac{\Gamma_{cb}(\Gamma + i\delta)n_{ca} + n_{cb}\Omega^2}{\Gamma_{cb}(\delta^2 + \Gamma^2) + 2\Gamma\Omega^2}\Omega. \tag{5.12}$$

The set of equations for populations can be obtained by substituting Eqs.(5.11,5.12) into Eq.(5.6) for the appropriate atomic populations:

$$\gamma_a n_a + \left(\frac{\Gamma_{cb}(\Gamma - i\delta)}{\tilde{\Gamma}_{cb}} + \frac{\Gamma_{bc}(\Gamma^* + i\delta)}{\tilde{\Gamma}^*_{cb}}\right)\Omega^2 n_{ab} + \left(\frac{1}{\tilde{\Gamma}_{cb}} + \frac{1}{\tilde{\Gamma}^*_{cb}}\right)\Omega^4 n_{cb} = 0, \tag{5.13}$$

$$\gamma_a n_a + \left(\frac{\Gamma_{cb}(\Gamma + i\delta)}{\tilde{\Gamma}_{cb}} + \frac{\Gamma_{bc}(\Gamma^* - i\delta)}{\tilde{\Gamma}^*_{cb}}\right)\Omega^2 n_{ac} + \left(\frac{1}{\tilde{\Gamma}_{cb}} + \frac{1}{\tilde{\Gamma}^*_{cb}}\right)\Omega^4 n_{bc} = 0, \tag{5.14}$$

where $\tilde{\Gamma}_{cb} = \Gamma_{cb}(\delta^2 + \Gamma^2) + 2\Gamma\Omega^2$. By introducing $A_b = A - \delta B$, $A_c = A + \delta B$, and

$$A = \left(\frac{\Gamma_{cb}\Gamma}{\tilde{\Gamma}_{cb}} + \frac{\Gamma_{bc}\Gamma^*}{\tilde{\Gamma}^*_{cb}}\right)\Omega^2, \quad B = -i\left(\frac{\Gamma_{cb}}{\tilde{\Gamma}_{cb}} - \frac{\Gamma_{bc}}{\tilde{\Gamma}^*_{cb}}\right)\Omega^2, \tag{5.15}$$

$$C = \left(\frac{1}{\tilde{\Gamma}_{cb}} + \frac{1}{\tilde{\Gamma}^*_{cb}}\right)\Omega^4, \tag{5.16}$$

the set equations for the populations can be re-written in the compact form

$$\gamma_a n_a + A_b n_{ab} + C n_{cb} = 0, \tag{5.17}$$

$$\gamma_a n_a + A_c n_{ac} + C n_{bc} = 0, \tag{5.18}$$

with the condition $n_a + n_b + n_c = 1$, we can solve the equations and get the following,

$$n_a = \frac{A_b A_c + C(A_b + A_c)}{3A_b A_c + C(3A_b + 3A_c + 4\gamma_a) + \gamma_a(A_b + A_c)} \tag{5.19}$$

$$n_b = \frac{A_b A_c + C(A_b + A_c + 2\gamma_a) + A_c\gamma_a}{3A_b A_c + C(3A_b + 3A_c + 4\gamma_a) + \gamma_a(A_b + A_c)} \tag{5.20}$$

$$n_c = \frac{A_b A_c + C(A_b + A_c + 2\gamma_a) + A_b\gamma_a}{3A_b A_c + C(3A_b + 3A_c + 4\gamma_a) + \gamma_a(A_b + A_c)} \tag{5.21}$$

The solution for the population difference in level b and c is given by

$$n_{cb} = \frac{2\gamma_a B\delta}{3A_b A_c + C(3A_b + 3A_c + 4\gamma_a) + \gamma_a(A_b + A_c)}. \tag{5.22}$$

Simplifying Eqs. (5.15,5.16), we obtain $A \simeq \gamma_{cb}$, $B \simeq \frac{\Delta}{\gamma}$, $C \simeq \frac{|\Omega|^2}{\gamma}$, and

$$n_{cb} \simeq \frac{\Delta\delta}{|\Omega|^2}. \tag{5.23}$$

The intensity fluctuations are determined by atomic coherences, which are

$$\mathrm{Im}\rho_{ab} \simeq \frac{\gamma_{cb}\gamma + \Delta\delta}{\gamma|\Omega|}, \quad \mathrm{Im}\rho_{ac} \simeq \frac{\gamma_{cb}\gamma - \Delta\delta}{\gamma|\Omega|}, \tag{5.24}$$

where the field phase fluctuation is related to the frequency deviation δ that is restricted by the EIT window [124], $\delta \sim \dfrac{\Omega^2}{\gamma}$.

We can see from Eq.(5.24) that the intensity fluctuations have two contributions: the first originates from absorption, which is the same for both modes, and the second originates from the Raman term appearing from the population difference n_{cb}, which has opposite signs for these two modes. One field is amplified due to absorption of the second field. Depending on the one- and two-photon detuning, Δ, the intensity fluctuations occur in phase if $\gamma_{cb}\gamma^2/\Omega^2 \gg \Delta$ or out of phase if $\gamma_{cb}\gamma^2/\Omega^2 \ll \Delta$. The last condition gives rise to the anti-correlations.

Let us note here that at the EIT condition, $\Delta = 0$, correlated intensities can be also considered from the point of view of matched pulses [135]. Note that in-

tensity correlations originate from the resonant interaction between radiation and matter. Phase of electromagnetic field propagating through the cell changes due to phase fluctuations of laser radiation and dispersion of the resonant medium, due to spontaneous emission and Raman-like scattering involving atomic coherence between magnetic sublevels of Rb atoms. These intensity correlations and anti-correlations have been experimentally observed in two orthogonally circularly polarized optical beams from the same laser [124] and in orthogonally linearly polarized optical beams from two independent lasers [125].

Now we are ready to consider intensity fluctuations between the orthogonally linearly polarized beams in the current experiment. Linearly polarized light can be regarded as a linear combination of left- and right-circular polarized light. The light with left- and right-circular polarizations does not change its state of polarization while propagating through the gas cell. We previously studied the correlation of intensity fluctuations between the normal modes [127].

In the current experiment, to detect rotation of polarization, we use the following scheme. After the polarizer, the beam propagates through the cell, and then after a half-wave plate, the polarization plane rotates 45^o degrees and is split by a PBS into two orthogonally polarized optical beams. The intensity of each beam is detected. Thus, the measured signals, S_1 and S_2, are proportional to the intensities of the propagated circularly polarized components, which are given by

$$S_{1,2} \sim I_{1,2} = \frac{1}{2}(I_+ + I_- \pm 2\sqrt{I_- I_+}\sin\phi), \tag{5.25}$$

and the polarization rotation ϕ is given by equation (5.1).

Then the correlation between S_1 and S_2 can be calculated by

$$G^{(2)}(\tau) = \frac{\langle \delta I_1(t)\delta I_2(t+\tau)\rangle}{\sqrt{\langle[\delta I_1(t)]^2\rangle\langle[\delta I_2(t+\tau)]^2\rangle}}. \tag{5.26}$$

As is seen from Eq. (5.25), the circularly polarized beams are equally split into two linear polarizations. Thus, the two intensities of the linearly polarized components are correlated. The only contribution that decreases the correlations is due to the terms depending on the rotational angle, which have different signs for orthogonal polarizations in Eq. (5.25).

The intensity fluctuations should be small for the components that are not perfectly anti-correlated. But as we have shown in a previous paper [124], increasing the magnetic field causes these components to become anti-correlated (note here that Raman-type effects described by Eq. (5.23, 5.24) are involved). On the other hand, increasing the magnetic field increases the rotation at first, but then once the splitting becomes bigger than the EIT width, the rotation angle decreases, restoring the correlations between the intensities of the linear components.

One can see from Eq. (5.25) that if the rotational angle in a magnetic field is small, the beams mainly consist of the sum of intensities for left- and right-circularly polarized beams, and thus the fluctuations are correlated. Anti-correlations come from the interference terms having different signs due to Faraday rotation in the magnetic field. So we have correlations at zero magnetic field. But for stronger magnetic fields, due to the decreasing of the angle of rotation, the interference term becomes much smaller than the sum of intensities of left- and right-circularly polarized components ($I_+ + I_- \gg 2\sqrt{I_- I_+}|\sin\phi|$), and only the correlation between beams is observed.

For larger two-photon detuning, the nonlinear magneto-optical rotation of polarization becomes smaller and intensity correlations restore their correlations. Define

$$I_+ = I_0 + i_+, \quad I_- = I_0 + i_-, \tag{5.27}$$

where $i_\pm$ are the intensity fluctuations of the beams $I_\pm$, correspondingly. Then,

using $\sqrt{1+z} \simeq 1 + \frac{z}{2} - \frac{z^2}{8}$, introducing $x = i_+ + i_-$ and $s = i_+ - i_-$ (note that $i_+ i_- - \frac{x^2}{4} = 4i_+ i_- - (i_+ + i_-)^2 = -(i_+ - i_-)^2 = -s^2$), we can rewrite Eqs. (5.25) as

$$I_{1,2} = 2I_0 + x \pm (2I_o + x - \frac{s^2}{4I_0}) \sin\phi. \tag{5.28}$$

Thus, we obtain

$$\delta I_{1,2} = I_{1,2} - \langle I_{1,2} \rangle = x(1 \pm \sin\phi) \mp \frac{s^2 - \langle s^2 \rangle}{4I_0} \sin\phi \tag{5.29}$$

and

$$\langle (I_1 - \langle I_1 \rangle)^2 \rangle = \langle x^2 \rangle (1 + \sin\phi)^2 + \frac{\langle s^4 \rangle - \langle s^2 \rangle^2}{16 I_0^2} \sin^2\phi \tag{5.30}$$

Finally, we can calculate the correlation function $G^{(2)}$, defined by Eq.(5.26),

$$G^{(2)}(0) = \frac{\langle x^2 \rangle \cos^2\phi + \frac{\langle s^4 \rangle - \langle s^2 \rangle^2}{16 I_0^2} \sin^2\phi}{\sqrt{\left(\langle x^2 \rangle \cos^2\phi + \left(\frac{\langle s^4 \rangle - \langle s^2 \rangle^2}{16 I_0^2} \right) \sin^2\phi \right)^2 + 4 \langle x^2 \rangle \frac{\langle s^4 \rangle - \langle s^2 \rangle^2}{16 I_0^2} \sin^4\phi}} \tag{5.31}$$

In the last equation, one can see that the correlation function $G^{(2)}(0)$ is close to unity for two cases: for small magnetic fields, when the rotation angle is small (the beam intensities are correlated [124]), and for strong magnetic fields, when the rotation angle is also small (the beam intensities are anti-correlated [124]). Correspondingly, in the intermediate case, we have correlations that are less perfect.

CHAPTER VI

ATOMIC EXCITATION BY FEW CYCLE RF PULSES

The development of modern laser technology has brought significant advantages to the study of field-matter interaction. As spectacular examples, modern lasers can cover a wide range of spectrum from X-ray to THz regime and produce remarkable ultra-short bursts of light such as atto-second pulses. However, there are cases where the sufficient flexibility of laser fields is not easily accessible, sometimes even impossible. For instance, it is extremely hard to obtain few cycle laser pulses with stable and controllable carrier-envelope phase, especially for atto-second pulses. Using electromagnetic waves in radio frequency (RF) or microwave regime provides an unique way to study field-matter interactions.

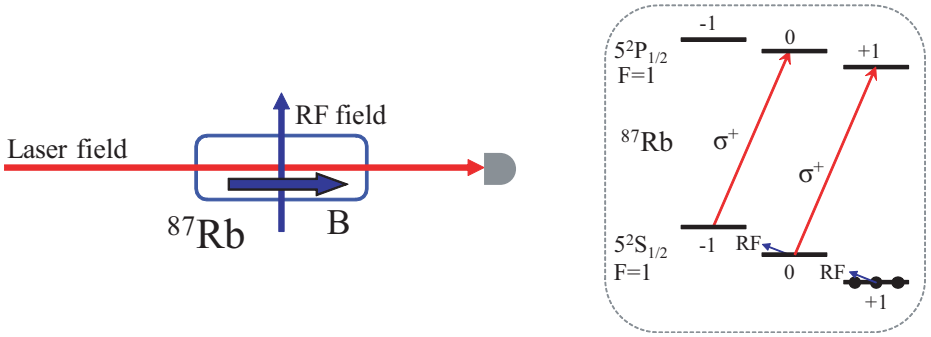

Fig. 40. The geometry of optical and RF fields alignment is shown on the left. The energy diagram is shown on the right.

It has been a long history to use RF fields to study properties of atoms [136]. In this chapter, we use an RF field to interact with the ground state Zeeman sublevels of rubidium atoms. The excitation by short RF pulses are studied under some extreme conditions which can hardly be realized with optical fields. In our experiments, the rubidium atoms are initially prepared by a circularly polarized laser field which opti-

cally pumps the system, thus populates one of the ground state Zeeman sublevels, as shown by the energy diagram in Fig. 40. We then apply an RF field to interact with the Zeeman sublevels and to transfer some population to the other Zeeman sublevels. The geometry of the field alignment is shown in Fig. 40(left). A static magnetic field along the propagation direction of the laser field is used to control the splitting of Zeeman sublevels. The excitation RF field is applied in the transverse direction. The population transferred by the RF field can be probed by measuring the absorption of the circularly polarized laser field.

This technique of using RF fields to interact with Zeeman sublevels has many advantages comparing with optical fields interacting with atoms. First of all, Zeeman sublevels are relatively well isolated from other levels since the transitions between them are energetically far away from other transitions, especially optical transitions. This makes it possible to have an experimental system with well isolated two level or three level atoms, which is fundamentally important from the theoretical point of view. The level splitting can be tuned over a large fractional range that no other system is capable of. Secondly, the RF field has an extreme flexibility on control of all parameters. It is hard or even impossible, in the optical domain, to achieve the same degree of control as in the RF domain over all parameters of the field. With the RF field, it is specially interesting that we can generate "ultra-short" (few cycles of oscillation) and "ultra-strong" (Rabi frequency comparable with the atomic frequency) pulses. We are able to fully control important parameters such as pulse shape, carrier-envelope phase, chirp and duration. With these advantages, this is a perfect system to model the processes in ultra-short laser physics. The studies conducted in the RF domain potentially have a great impact on experiments in the optical domain.

Before moving on to the study with RF fields, we have run several demonstrations

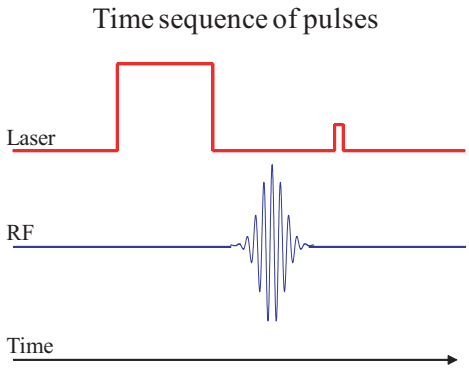

Fig. 41. The time sequence of optical and RF pulses.

to assure ourselves that the system with RF field can excite atoms as what we know in the optical domain. The experiment can be performed with continuous wave (CW) fields or pulsed fields. With CW fields, the optical field optically pumps the systems and has a certain transmission. The excitation by an RF field introduces changes in the transmission which can be recorded to characterize the excitation. While in the case of pulsed fields, as shown in Fig. 41, a strong optical field is used to prepare the system by the optical pumping, then we apply an RF pulsed followed by a weak optical pulse as the probe. The population transfer by the RF pulse can be measured by the absorption of the probe pulse.

In the first demonstration, we keep the optical field as a continuous wave and use an RF pulse to excite the transition. In Fig. 42, the red curve represents the transmission of the optical field which is related to the population of upper states, while the blue curve is the amplitude of RF field. Applying the RF pulse changes the transmission of optical field. The RF frequency matches the splitting of Zeeman sublevels such that the excitation is on resonance. The oscillation in the transmission of optical field is identified as the Rabi oscillations.

In the second demonstration, we use pulses for both the RF field and the optical

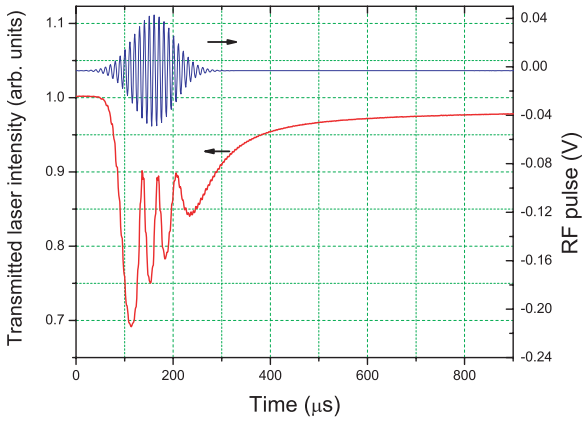

Fig. 42. The Rabi oscillation in the transmission of laser field as the an RF pulse excites the transition between Zeeman sublevels. The blue curve is the RF field and the red curve is the transmission of laser field.

field. For the convenience to implement in experiments, the frequency of RF field is kept constant as 50 kHz, and the splitting is varied by changing the longitudinal magnetic field. In Fig. 43, we plot the transmission of the probe pulse as a function of the Zeeman splitting. In (a), the applied RF field is linearly polarized, there are two absorption peaks corresponding to the one-photon and three-photon excitations. The one-photon excitation happens at 50 kHz, while the three-photon excitation is shifted to about 130 kHz due to Bloch-Siegert shift [137]. In (b), the applied RF field is circularly polarized (σ^-), the selection rules allow only the one-photon excitation but not the three-photon excitation. In (c), a σ^+ field is used, thus neither the one-photon excitation nor the three-photon excitation are allowed and there are no absorption peaks appear.

Both demonstrations show that the transition between Zeeman sublevels can be excited by RF fields. The transferred population due to excitation can be probed sufficiently by the optical field. The system works as we expect from the excitation by optical fields, thus we can use it to model the processes in the optical domain. We

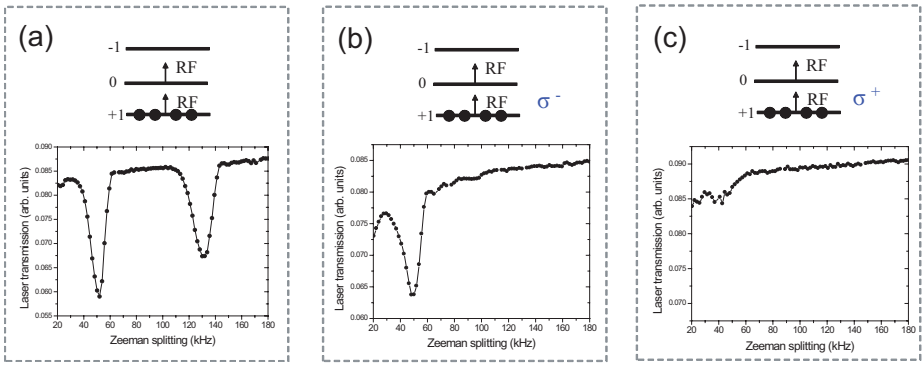

Fig. 43. The excitation by RF fields with different polarizations. There are one-photon and three-photon excitations according to the selection rules.

will discuss two of such examples in the following sections.

A. Carrier envelope phase effect on atomic excitation

Modern pulsed laser can produce ultra-short intense bursts of light with only few cycles of carrier oscillation [138]. The carrier-envelope (CE) phase strongly affects many processes involving few-cycle pulses. In particular, it has been demonstrated the CE phase effects on the high-harmonic generation [139], the strong-field photoionization [140], the ionization of Rydberg atoms [141], the dissociation of HD^+ and H_2^+ [142], and the injected photocurrent in semiconductors [143], by few-cycle pulses. The stabilized and adjustable CE phase is important for applications such as optical frequency combs [144] and quantum control in various media [145, 146, 147]. Several techniques have been developed to control the CE phase of femtosecond pulses [148, 149]. A crucial step is to measure the CE phase and provide a feedback to the laser system. Promising approaches use, for instance, the photoionization [150, 151] and the quantum interference in semiconductors [143].

In this section, we study the CE phase effect on population transfer between

two bound atomic states interacting with few-cycle pulses. For our experiment, we use intense RF pulses interacting with the magnetic Zeeman sublevels of rubidium (Rb) atoms. The pulses are only a few cycles in duration and have Rabi frequencies comparable to the carrier frequency. We have found that short pulses can be crafted to cause significant population transfer, the CE phase of the pulse strongly affects that transfer, and relatively large population transfer may be observed far off resonance.

The significance of our experiment is two-fold. First, it provides the insight of CE phase effect in a new regime. Unlike the processes mentioned above, our experiment is the first, to our knowledge, to observe the CE phase effect on a transition between two *bound* atomic states. The transition is driven by RF pulses with the Rabi frequency comparable to the carrier frequency, a regime being mainly studied theoretically [152, 153, 154]. Our study in RF domain suggests experiments with bound states and few-cycle pulses in optical domain as another way to measure the CE phase. Furthermore, the observed phase dependent excitation, as a result of the interference between one- and multi-photon transitions [143, 155], is important to quantum control experiments [145, 146, 147]. Second, as we mentioned before, our experimental system provides an unique system serving as an experimental model for studying ultrashort optical pulses. The system is suitable for studies which the technology in optical domain is not ready for, it may also lead to further suggestions for optical experiments.

1. Excitation by cos and sin pulses

In this experiment, we study the excitation by the ultrashort pulses described in Fig. 44(A,B) interacting with a two-level atom; states $|c\rangle$ and $|d\rangle$ refer to the excited and ground states, respectively, as shown in Fig. 44(C). These pulses have the same envelope but different CE phases. One pulse may be called a cosine pulse (see

Fig. 44(A)); the other, a sine pulse (see Fig. 44(B)). The amount of excited population depends on the shape of the pulses [156].

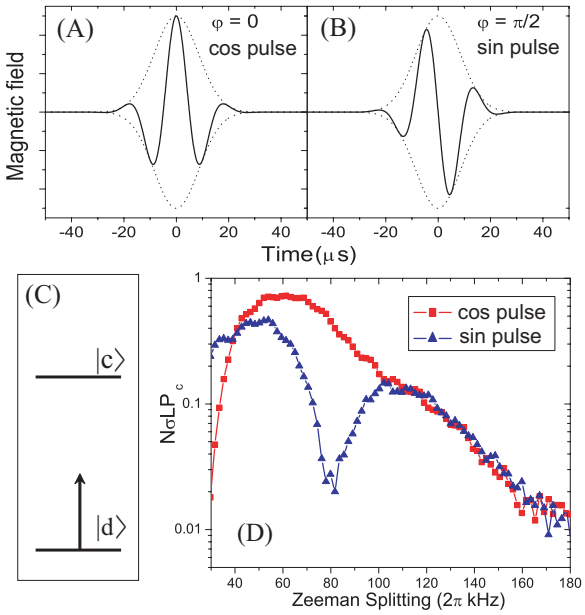

Fig. 44. A few-cycle RF pulse with different carrier-envelope phases: (A) $\varphi = 0$; (B) $\varphi = \pi/2$. The dotted curves indicate the envelope of the pulses. Figure (C) shows a two-level system with $|c\rangle$ as the excited state and $|d\rangle$ as the ground state. Figure (D) shows the population of $|c\rangle$ excited by an RF pulse as a function of the frequency difference of the two-level system. The two curves correspond to the results of the cosine ($\varphi = 0$)and the sine ($\varphi = \pi/2$) pulses.

Our experiment is performed in a gas of rubidium atoms. A 2.5 cm-long cell containing ^{87}Rb (and 5 torr of neon) is located within a magnetic shield. The cell is heated in order to reach an atomic density of the order of 10^{12} cm^{-3}. The configuration of the optical and magnetic fields is shown in Fig. 45. A longitudinal static magnetic field is applied along the laser beam to control the splitting of the Zeeman sublevels of the ground state. A pair of Helmholtz coils produces a transverse RF field at a frequency of 50 kHz.

The energy level scheme is shown in Fig. 45. The ground state (^{87}Rb, $5^2S_{1/2}$,

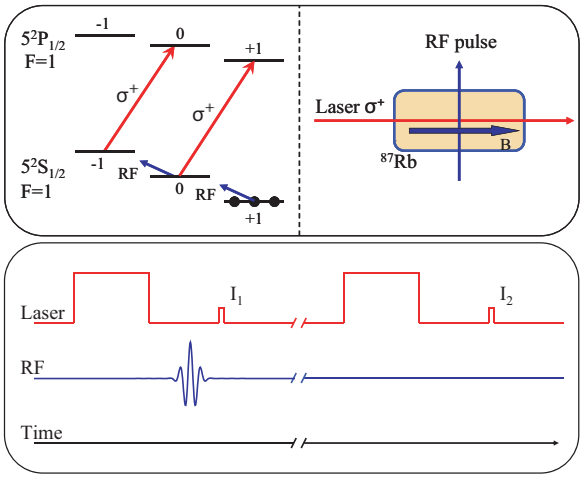

Fig. 45. The upper block shows a diagram of the relevant energy levels and the geometry of the Rb cell and the applied fields. The lower block shows the time sequence of the laser pulses and the RF pulses.

$F = 1$) has three sublevels; a circularly polarized laser pulse optically pumps the system and drives the atoms to the sublevel with $m_F = +1$. This is followed by a few-cycle RF pulse, which excites some population to the sublevels with $m_F = 0$ and $m_F = -1$. The population in the sublevels with $m_F = 0, -1$ is subsequently determined by measuring the transmission of a weak circularly-polarized probe pulse.

The Hamiltonian for an atomic state with $F = 1$ in a magnetic field $B = (B_x, B_y, B_z)$ is given by

$$\hat{H} = -g\mu_0 \begin{pmatrix} B_z & \frac{B_x+iB_y}{\sqrt{2}} & 0 \\ \frac{B_x-iB_y}{\sqrt{2}} & 0 & \frac{B_x+iB_y}{\sqrt{2}} \\ 0 & \frac{B_x-iB_y}{\sqrt{2}} & -B_z \end{pmatrix} \tag{6.1}$$

where $g = -1/2$ is the Lande factor for this Rb state, μ_o is the Bohr magneton, the $B_z = B_0$ is the static magnetic field that is chosen in the direction of z-axis; the B_x and B_y are the transverse components that are driven by a digital function generator.

The function generator can be programmed to provide short pulses with controllable parameters, such as the pulse duration and the CE phase. To make sure the coils produce the expected pulses, a signal from a sampling resistor in serial is used to monitor the current in the coils.

The time sequence of the laser pulses and RF pulses is detailed in Fig. 45. The sequence of laser pulses includes a 1.5 ms strong pulse to optically pump the Rb atoms, and a 5 μs weak pulse (100 μs later) to probe the population of the upper Zeeman sublevels. The sequence repeats every 20 ms. The linearly-polarized magnetic field component of the RF field, $B_x = B(t)\cos(\nu t + \phi)$ and $B_y = 0$, has a Gaussian-shaped envelope $B(t) = B_{ox}\exp\left[-\left(\frac{t}{\tau}\right)^2\right]$, where $\tau = T/(2\sqrt{\ln 2})$, and T is the FWHM duration of the pulse. The RF pulse is delayed by 50 μs with respect to the optical-pumping laser pulse, and its duration, T, varies from 20 to 28 μs. The transmitted intensity of the probe pulse is monitored by a fast photodiode.

The transmitted intensity of the probe pulse does not directly give the population of the upper levels. We need to take into account the processes of atomic relaxation and noise in the laser system. The latter is related to the intensity and frequency fluctuations of laser.

To determine the population transfer due to the RF excitation, the experiment is performed with a sequence of laser pulses with a RF pulse followed by a sequence of laser pulses without RF pulse. For the first sequence, the transmitted probe pulse intensity is given by $I_1 = I_0\eta e^{-N\sigma LP_c}$, where I_0 is the probe pulse input intensity, η is a factor due to the dephasing, N is the atomic density, σ is the absorption cross section, L is the cell length, and P_c is the population of the upper sublevels due to the RF excitation. For the second sequence, in which there is no RF excitation, the transmitted probe pulse intensity is given by $I_2 = I_0\eta$. Therefore, the population due to the RF excitation is given by the quantity $-\ln(I_1/I_2) = N\sigma LP_c$, which is

presented as our experimental results in Fig. 44(D).

To calculate the behavior of this system, we employ the density matrix approach, which naturally incorporates the relaxation processes. Even though the relaxation of the atomic system with no optical pumping is slow, it is important to explain the experimentally observed results. The set of density matrix equations is given by $\dot{\rho} = -\frac{i}{\hbar}[H, \rho] - \Gamma(\rho - \rho_0)$, where H is given by Eq. (6.1), Γ describes the relaxation in the system from atomic motion, and ρ_0 is the thermal equilibrium density matrix of atoms in the cell without the optical and RF fields. We assume that the optical-pumping step transfers all of the population to the $|S_{1/2}F, m_F\rangle = |1, -1\rangle$ state, and then we simulate atomic dynamics using the density matrix equations.

The main experimental result is shown in Fig. 44(D), where the quantity $N\sigma LP_c$ is plotted as a function of the Zeeman splitting. The behavior is dramatically different for the sine and cosine pulses, as is shown by the blue and red curves respectively. The RF pulses all have the same carrier frequency (50 kHz), and we modulate the Zeeman splitting. The RF pulse has a Gaussian envelope with the duration (FWHM) of 20 μs (one cycle). For the sine pulse, we observe a well-defined one-photon resonance at 50 kHz and a three-photon resonance that is shifted to about 110 kHz (Bloch-Siegert shift [137]). For the cosine pulse, the upper state population decreases almost exponentially as the atomic frequency is tuned away from one photon resonance. An important feature is that, at 80 kHz, the RF excitation for the cosine pulse is larger by over an order of magnitude compared to that of the sine pulse. This shows that it is crucial to take into account the CE phase for processes involving few-cycle pulses.

2. Dependence on pulse duration and CE phase

We also studied the effect of the CE phase for different RF pulse durations. As an example, Fig. 46 shows the results for both the cosine and sine pulses with different

durations varying from 20 to 28 μs. We compared these experimental results with the theoretical simulations from the set of density matrix equations. The short pulse transfers population from the ground state $|1,-1\rangle$ to the states $|1,0\rangle$ and $|1,1\rangle$ (see Fig. 45). The circularly-polarized probe laser is absorbed because it is equally coupled to the transitions $|S_{1/2}1,0\rangle \rightarrow |P_{1/2}1,-1\rangle$ and $|1,1\rangle \rightarrow |P_{1/2}1,0\rangle$ as shown in Fig. 45 (the dipole moments of both transition are the same). The depletion of population from the ground state is given by $1-\rho_{1,-1}$. The calculated signals are shown in Fig. 46 (c) and (d), which agrees well with the experimental results in (a) and (b).

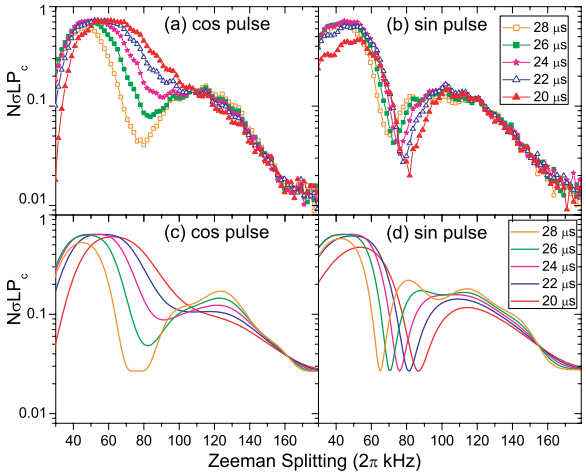

Fig. 46. The population of the upper Zeeman sublevels excited by (a) cos RF pulses; (b) sin RF pulses with different pulse durations from 28 to 20 μs. Corresponding theoretical simulations appear in (c) and (d).

The results can be understood as the CE phase dependent interference between one- and multi-photon transitions as suggested in [143, 155]. When the pulse is so short that its frequency spectrum is broad enough to cover two frequencies for both one- and three-photon transitions, the overall excitation depends on the interference between the one- and three-photon pathways. As shown in Fig. 44(D), the sine pulse has a destructive interference while the cosine pulse has a constructive one. If the

pulse duration becomes longer, the narrower spectrum makes the interference and the effect of CE phase less pronounced. As shown in Fig. 46, the difference of excitations is less influenced by the CE phase as the pulse duration goes from 20 μs to 28 μs. The results also suggest that a few-cycle pulse with adjustable CE phase can manipulate the atomic excitation, the same method can be used for quantum control in atoms [145], molecules [146] and semiconductors [147].

For a simple mathematical description of the results, let us neglect relaxation and consider only two levels coupled by the radiation field (see Fig. 44(C)). The Rabi frequency is given by $\Omega(t) = \Omega_0 f(t)\exp(-\alpha^2 t^2)$, where $f(t) = f_0(e^{i\nu t} + pe^{-i\nu t})$ is either $\sin(\nu t)$ or $\cos(\nu t)$. For $\sin(\nu t)$, $p = 1$ and $f_0 = 1/2$; for $\cos(\nu t)$, $p = -1$ and $f_0 = -i/2$. The equations for the state vector $|\Psi\rangle = Ce^{i\omega_c t}|c\rangle + D|d\rangle$ are

$$\dot{C} = -i\tilde{\Omega}D, \quad \dot{D} = -i\tilde{\Omega}^* C \tag{6.2}$$

where we introduce $\tilde{\Omega} = \Omega_0 f(t)\exp(-\alpha^2 t^2 + i\omega_c t)$. For the lowest order in the coupling field ($D \simeq 1$), the solution of Eq. (6.2) is

$$C^{(1)} \simeq -\frac{i\sqrt{\pi} f_0 \Omega_0}{\alpha}\left(e^{-\frac{(\omega_c-\nu)^2}{4\alpha^2}} + pe^{-\frac{(\omega_c+\nu)^2}{4\alpha^2}}\right). \tag{6.3}$$

One can see that for long ($\alpha << \omega_c$) and short ($\alpha \sim \omega_c$) pulses, both the sine and cosine pulses have a similar profile: we have a sum of two spectral components at $\pm\omega_c$. The profile has no zero points for $\nu > 0$. For the next non-zeroth order, we have four terms that correspond to spectral components at $\pm\omega_c$ and $\pm\omega_c/3$ and their spectral widths are broader. As in Eq. (6.3), the positive and the negative frequency components do not strongly influence each other. The components at ω_c and $\omega_c/3$ are given by

$$C^{(3)} \simeq i\frac{\sqrt{\frac{\pi}{3}} f_0^3 \Omega_0^3}{\alpha(\omega_c - \nu)^2}\left(p\xi e^{-\frac{(\omega_c-\nu)^2}{12\alpha^2}} + e^{-\frac{(\omega_c-3\nu)^2}{12\alpha^2}}\right), \tag{6.4}$$

where $\xi = (3\omega_c - \nu)/(\omega_c + \nu)$. For long pulses, these components are easily resolved. But for short pulses (a few periods of oscillations, $\alpha \sim \omega_c$), the widths of these components are broader than the widths of the components of $C^{(1)}$. For the cosine pulse, the components are not resolved: the profile resembles one broad spectral component. For the sine pulse, the situation is completely different: the total profile has zero at $\omega_c = 2\nu + 3\alpha^2 \frac{\ln \xi}{\nu}$ where the components (having opposite signs) cancel.

Another insight into the observed effect can be related to the Ramsey effect [157]. Namely, the two pulses delayed with respect to each other produce interference. Sine-pulse (see in Fig. 1) can be viewed as two pulses and changing the frequency introduces delay between pulses. Meanwhile a cosine-pulse is just one pulse and changing frequency changes just the duration of the pulse. Then, what we have observed is that the first half of the sine-pulse is interfering with the second half of the sin pulse, and this interference produces the dip in the excitation of upper level (see in Fig. 1).

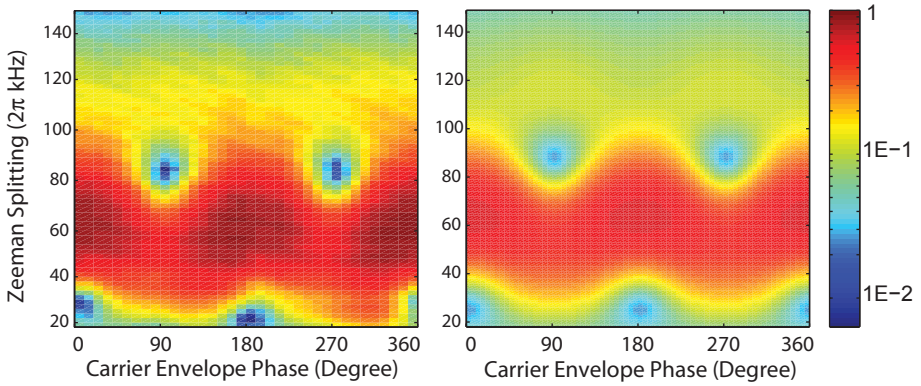

Fig. 47. The population excited by the RF pulse dependence on the CE phase. Experiment result is shown in left panel and simulation in right panel.

Thus, sine and cosine pulses, which correspond to a change of $\pi/2$ in CE phase difference, can be clearly distinguished. Our last study involved changing the CE phase in smaller steps. In particular, we performed experiments with the pulses with

CE phases varying from 0 to 360° by steps of 10° for various Zeeman splittings. The result is shown as an image in Fig. 47 (left panel). The RF pulses used in the experiment have the frequency 50 kHz and the pulse duration (FWHM) 20 μs. The obtained data is plotted using color coding showing in Fig. 47. The range of the population in the excited state is the same as in Fig. 46. One can see that the excited population is a continuous function of the CE phase at a given Zeeman splitting, and consequently, this can be used to determine and/or to control the CE phase of the ultra-short pulses. We have performed simulations that reproduce the observed results and they are shown in Fig. 47 (right panel). We note that measuring population in the excited state might be easier than the asymmetry of the direction of produced ions or electrons. This figure also demonstrates the temporal stability of the experimental setup.

In conclusion, we have theoretically and experimentally demonstrated that the carrier-envelope phase effect on population transfer between two bound atomic states interacting with intense ultra-short pulses. The pulses are only a few cycles in duration and have Rabi frequencies of the order of the carrier frequency. The phase difference between the carrier and the envelope of the pulses has a significant effect on excitation of atomic coherence and population transfer. We acknowledge and honor here the ground-breaking experiments performed with CW RF radiation [136]. These experiments in the RF region might furnish physical insight for the development of CE phase control in optical fields, which are important for the generation of pulses with a predetermined absolute phase.

B. Off-resonance excitation by short laser pulses *

The two-level system (TLS) is a useful model with application to many fields such as condensed matter physics, quantum field theory and quantum optics. Substantial work has been directed toward detailed analytical solutions as well as experimental verifications. Our experimental system with RF fields and Zeeman sublevels provides an opportunity to experimentally study such a two-level system.

In this section we consider a two-level atomic system under the action of a far-off resonance, strong, ultra short, pulse of laser radiation. We first develop new solutions for a TLS transcending the usual multiphoton adiabatic treatments. In particular, we show that intense ultrashort pulses can excite remarkable coherence on high frequency far-detuned transitions. We then show the experiment performed with RF fields whose result supports the theoretical calculation. This result holds promise for various applications, such as a new approach to the generation of XUV radiation as is discussed in detail in [158].

1. A Model of off-resonant field-atom interaction

In this section, I will present an analytical treatment of the detuned atom-field interaction beyond the rotative wave approximation (RWA). The Hamiltonian of a two-level system is given by

$$\hat{H} = \hbar\omega_c|c\rangle\langle c| - \wp\mathcal{E}|c\rangle\langle d| - (\wp\mathcal{E})^*|d\rangle\langle c|,$$

where $\hbar\omega_c$ is the energy difference between two levels; $\wp$ is the atomic dipole moment; $\mathcal{E}(t) = E(t)\cos(\nu t)$ is the classical external electromagnetic field having amplitude

*Part of the data reported in this section is reprinted with permission from "*Excitation of atomic coherence using off-resonant strong laser pulses,*" by Y.V. Rostovtsev *et al.*, Phys. Rev. A **79**, 063833 (2009), Copyright by the American Physical Society.

$E(t)$ and frequency ν. The state vector can be written as

$$|\Psi\rangle = C(t)e^{-i\omega_c t}|c\rangle + D(t)|d\rangle. \tag{6.5}$$

Introducing $\tilde{\Omega}(t) = \frac{\wp\mathcal{E}(t)}{\hbar}e^{i\omega_c t}$, the Schrödinger equation yields the set of equations

$$\dot{C} = -i\tilde{\Omega}(t)D \tag{6.6}$$

$$\dot{D} = -i\tilde{\Omega}^*(t)C \tag{6.7}$$

The amplitude of the Rabi frequency, even for modern level of laser intensities is much smaller than the frequency of transition, $|\tilde{\Omega}(t)| \ll \omega_c$, all population is in the ground state, $|D(t)| \simeq 1$, the value of $|C(t)|$ is small, and it is given by

$$C(t) \simeq -i\int_{-\infty}^{t} dt'\tilde{\Omega}(t'). \tag{6.8}$$

It is instructive to compare a solution of Eqs. (6.6) (6.7) for different pulse shapes and also to compare the RWA with the exact ones. For the Gaussian pulse, for RWA, $\tilde{\Omega}(t) = \Omega_0 e^{i\Delta t - \alpha^2 t^2}$, where $\Delta = \omega_c - \nu$. Eq. (6.8) gives

$$C(\infty) = -i\int_{-\infty}^{\infty} \Omega(t)e^{i\Delta t}dt = -i\sqrt{\pi}\frac{\Omega_0}{\alpha}\exp\left(-\frac{\Delta^2}{4\alpha^2}\right). \tag{6.9}$$

In particular, we note that Eq. (6.9) goes with the usual "wisdom" that it is the "high frequencies contained in the envelop" that make the transition resonant for large detunings. This is an oversimplification. Indeed, Eqs. (6.6) (6.7) are nonlinear with respect to the field and the excitation can be orders of magnitude higher than that given by Eq. (6.9). The best way to see it, let us introduce the function $f(t) = C/D$. Then Eqs. (6.6) (6.7) yield the following Riccati equation

$$\dot{f} = i\Omega^*(t)\cos(\nu t)e^{-i\omega_c t}f^2 - i\Omega(t)\cos(\nu t)e^{i\omega_c t}. \tag{6.10}$$

The solution of Eq. (6.10) allows one to find the amplitude for excited state $C(t)$ as $|C(t)| = |f(t)|/\sqrt{1+|f(t)|^2}$. In the RWA, Eq. (6.10) reduces to

$$\dot{f} = i\frac{\Omega^*(t)}{2}e^{-i\Delta t}f^2 - i\frac{\Omega(t)}{2}e^{i\Delta t}. \tag{6.11}$$

Now we are ready to calculate $C(\infty)$ for the Gaussian pulse in the next order. By substituting Eq. (6.8) into Eq. (6.11), we obtain, for $\Delta \gg \alpha$,

$$C(\infty) \approx -i\sqrt{\pi}\frac{\Omega_0}{\alpha}e^{-\frac{\Delta^2}{4\alpha^2}} + i\sqrt{\frac{\pi}{3}}\frac{\Omega_0^3}{\alpha\Delta^2}e^{-\frac{1}{12}\frac{\Delta^2}{\alpha^2}}. \tag{6.12}$$

The nonlinear-term correction is proportional to $\exp[-\frac{1}{12}\frac{\Delta^2}{\alpha^2}]$, while in the first order we have $\exp[-\frac{1}{4}\frac{\Delta^2}{\alpha^2}]$. The ratio of the second and the first terms in Eq. (6.12) is $\frac{\Omega_0^2}{\sqrt{3}\Delta^2}\exp[\frac{1}{6}\frac{\Delta^2}{\alpha^2}]$. As a result, for $\Delta \gg \alpha$ the nonlinear-term correction is exponentially larger than the answer obtained by solving the linearized equation.

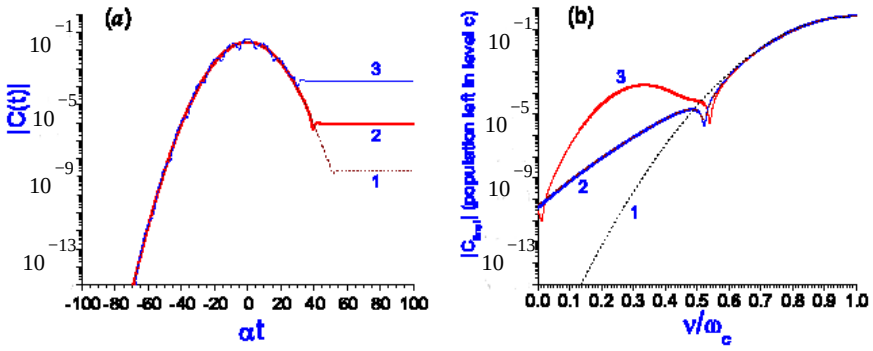

Fig. 48. (a) Time dependence of population in level C for a Gaussian pulse. Curve (1) corresponds to the linear solution of Eq. (6.8); (2) and (3) are the solutions of Eqs. (6.6) (6.7) for RWA and exact for $\nu/\omega_{cd} = 1/3$. (b) Population left in the upper level $|c\rangle$ after applying Gaussian pulse as a function of the pulse frequency ν obtained for linear solution given by Eq. (6.8) – curve (1), RWA – curve (2), and exact – curve (3).

In Fig. 48(a), we show the results for the Gaussian pulse obtained for the ap-

proximated and exact solutions of Eq. (6.6) (6.7) (for the exact solution, $\tilde{\Omega}(t) = \Omega_0 \cos(\nu t) e^{i\omega_c t - \alpha^2 t^2}$) shown by lines 1, 2, 3. We take $\alpha = 0.08\omega_c$ and $\Omega_0 = 0.02\omega_c$ (for RWA) and $\Omega_0 = 0.04\omega_c$ for the exact solution.

Dot line 1 in Fig. 48(b) shows the curve given by Eq. (6.9). Dash line 2 in Fig. 48(b) shows $|C(\infty)|$ given by Eq. (5). The exact solution agrees with the numerical solution of Eq. (6.6) (6.7). Dip on the curve occurs due to interference when the second term in Eq. (8) cancels the first one. Note that line 1 lies substantially below the solid lines 2 and 3 at large detuning.

Next, we rewrite the nonlinear term in Eq. (6.10) as

$$f^2 = (f - f_1)^2 + 2ff_1 - f_1^2, \tag{6.13}$$

where $f_1(t)$ is the solution of Eq. (6.10) without the f^2-term, that is

$$f_1(t) = -i\theta(t), \tag{6.14}$$

and the tip angle θ is defined by $\theta(t) = \int_{-\infty}^{t} dt' \tilde{\Omega}(t')$. Then, Equation (6.10) can be rewritten as

$$\dot{f} + i\dot{\theta} = 2\theta\dot{\theta}^*(f + i\theta) - i\theta^2\dot{\theta}^* + (f + i\theta)^2 \tag{6.15}$$

or in the form of an integral equation

$$f + i\theta = \int_{-\infty}^{t} dt'[(f + i\theta)^2 - i\theta^2\dot{\theta}^*] \exp[2\Phi(t, t')], \tag{6.16}$$

where $\Phi(t, t') = \int_{t'}^{t} dt'' \theta\dot{\theta}^*$. Now we can see that Eq. (6.16) is the solution of Eq. (6.10) if $|f + i\theta|^2 \ll |\theta^2\dot{\theta}^*|$.

Another way to go beyond the simple adiabatic solution, we consider the following approximation of the nonlinear term in Eq. (6.10)

$$f^2 = (f - f_1)^2 + 2ff_1 - f_1^2 \approx 2f_1 f - f_1^2, \tag{6.17}$$

Then Equation (6.10) reduces to

$$\dot{f} = \theta\dot{\theta}^*(2f + i\theta) - i\dot{\theta} \tag{6.18}$$

which has the exact solution given by

$$\frac{C(t)}{D(t)} = -i\int_{-\infty}^{t} dt' \left(\frac{d\theta(t')}{dt'} - \theta^2(t')\frac{d\theta^*(t')}{dt'}\right) \times$$
$$\exp\left(2\int_{t'}^{t} \theta(t'')\dot{\theta}^*(t'')dt''\right). \tag{6.19}$$

By iterating this procedure, we could have used the obtained solution to improve results further.

2. Experimental implementation with RF fields

To experimentally demonstrate the excitation difference between the calculations by taking into account the RWA and no RWA, we use the technique described above using RF fields and Zeeman sublevels. The experiment is performed with rubidium atoms. The atoms are initially optical pumped to the ground state sublevel with $m_F = +1$, then an RF pulse with the frequency of 50 kHz is applied to induce the excitation, as shown in Fig. 49(a). The splitting between the sublevels is tunable by changing the longitudinal magnetic field. In the experiment, the frequency of the RF field is fixed while we vary the splitting to introduce different detunings in the system. The RF field can be linearly polarized or circularly polarized. In the later case, two sets of coils are used to produce the magnetic field and the drive currents in two sets are out of phase by 90°.

The experimental result is shown in Fig. 49(b). We plot the population of upper states as a function of the ratio of field frequency to atomic frequency, i.e. Zeeman splitting. Curve (1) represents the result for the linear polarization and the curve

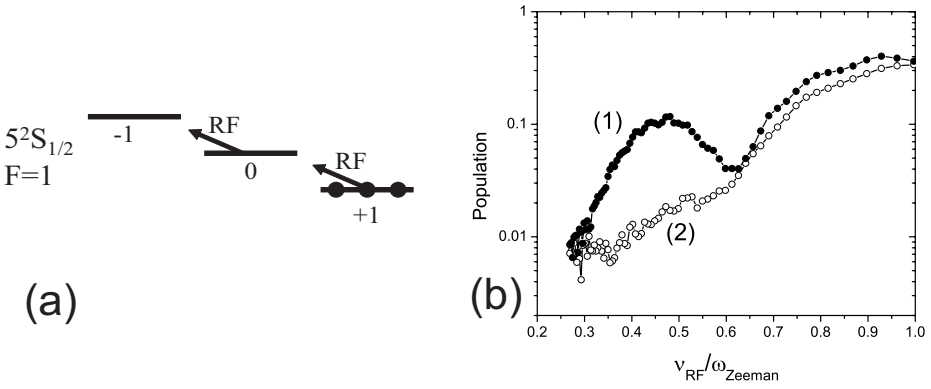

Fig. 49. (a) The energy diagram. (b) Experimentally observed excited population vs the ratio $\frac{\nu}{\omega_{cd}}$ for a Gaussian pulse.

(2) is the result for the circular polarization. For a circularly polarized field, there is only the rotating component in the field and the excitation curve can be described by the calculation with RWA. However, for the linearly polarized field, the excitation does not behave as described by the calculation with RWA. To properly model the excitation by a linearly polarized light, we need to use the approach described in the above section. Under the off-resonant conditions, the fields with different polarizations show a remarkable difference in the excitation. The result is helpful to understand how to use a short and strong laser pulse to induce the excitation under off-resonant conditions.

In conclusion, we presented an analytical solution for population transfer in a two-level system interacting with an external off-resonant classical field. The solution is valid for a very general driving perturbation without making the RWA. Multiphoton processes appearing due to the counter-rotating terms in the interaction Hamiltonian can substantially enhance the population transfer in a two-level system. One can suppress such processes, e.g., by making the applied driving field circularly polarized. As a consequence, predictions of the present analysis can be tested experimentally in

various regimes using circularly or linearly polarized driving fields. We have performed experiments in Rb vapor that support our theoretical results.

CHAPTER VII

OPTICAL PROPERTIES OF HIGHLY DENSE ATOMIC VAPOR

For a highly dense atomic vapor ($N > 10^{16}$ cm^{-3}), the dipole-dipole interaction between atoms in the ground and excited states becomes significant and can not be neglected. It is important for many applications and fundamental physics to study the nonlinear optical response of such dense vapor in which the dipole-dipole interaction dominates. The high optical density makes it hard to use conventional transmission spectroscopy to study highly dense media, while the reflection spectroscopy is the proper tool.

Almost a century ago, Wood [159] discovered that the reflection from the mercury vapor has a resonant structure around the mercury absorption line at 253.7 nm. The similar reflection spectra were observed later for alkali vapor [160, 161, 162]. This phenomenon is known as Selective Reflection (SR), in which the reflection coefficient of light reflected from an interface between a transparent dielectric and an absorbing vapor has a resonant structure near an absorption line of the atomic vapor. The SR spectrum solves the problem of strong absorption in a highly dense vapor. However, the spectrum broadening due to the dipole-dipole interaction reduces the spectral resolution.

In this chapter, we study the SR spectrum from the interface between the cell window and the Rb vapor. As we increase the atomic density, the spectrum is strongly broadened so that the hyperfine structures are not resolvable. We found that applying an additional pump laser can reduce the dipole-dipole interaction, thus reduces the broadening and increase the spectral resolution. We have also studied the excitation dependence of the broadening at different atomic densities to find the experimental evidence for the the disordered exciton theory [163] of self-broadening.

A. Selective reflection from Rb vapor

Selective reflection is a useful spectroscopic technique to study optical properties of dense atomic vapor and atom-surface interactions. Linear SR spectroscopy has been applied to study collision-induced self-broadening and shifts of atomic resonance lines [164, 165], the van der Waals interaction between atoms and a surface [166, 167], the Zeeman structure of the Cesium D_2 line [168], etc. Nonlinear extensions of SR spectroscopy with the probe-pump scheme have been theoretically studied for two-level [169, 170] as well as three-level atoms [171, 172]. Numerous nonlinear effects of SR have been observed and studied in the recent years. For instance, light-induced ground state Zeeman coherence [173, 174], spectral structure inside homogeneously self-broadened lines [175], the excitation dependence of the Lorentz local-field shift and self-broadening [176, 177], coherent effects in ladder scheme [178] have been observed. Practically, SR provides a potential means for novel optical filters [179] and possible optical bistability.

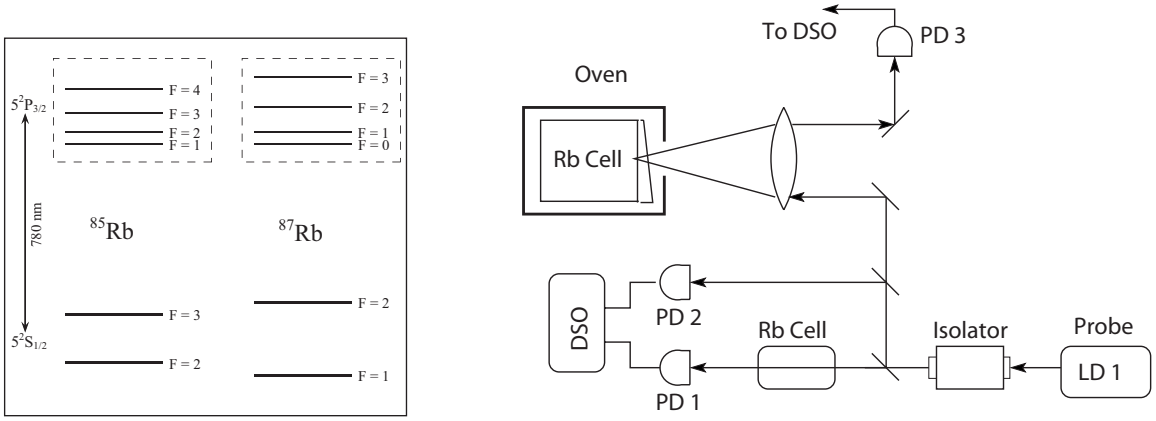

Fig. 50. The energy diagram of ^{85}Rb and ^{87}Rb atoms on the left. The schematic of selective reflection experiment on the right.

A simple selective reflection experiment can be performed on the window of a rubidium cell as shown in Fig. 50. The cell contains the natural abundance of isotopes

and it is installed in an oven so that the atomic density can be controlled. A laser beam from a free running diode laser shines on the window of the cell. The window is slightly wedged, thus the reflection from two surfaces can be separated. The reflected beam from the surface of the window and the vapor is detected by a photo-detector PD3. To establish a frequency reference, the absorption spectrum of rubidium vapor at the room temperature is recorded by PD1. The signal from PD2 is used to calibrate the laser intensity variation due to injecting-current scanning. The laser is tuned to the rubidium D2 line (780 nm). As shown in the energy diagram in Fig. 50, there are four hyperfine levels in the ground state while the splitting between the hyperfine levels in the excited state is smaller than the doppler broadening. When the atomic density is not too high, we can see four resonance structures in the reflectivity, as shown in Fig. 51(1), as we scan the laser frequency. The spectrum gets broader if the atomic density increases and the broadening due to dipole-dipole interaction dominates, in which case the ground state hyperfine levels can not be resolved as shown in Fig. 51(8).

The reflectivity from the interface of the window and the vapor can be calculated by the Fresnel equations [79],

$$R_{\parallel} = |\frac{n_w \cos i - n \cos t}{n_w \cos i + n \cos t}|^2, \quad R_{\perp} = |\frac{n \cos i - n_w \cos t}{n \cos i + n_w \cos t}|^2 \tag{7.1}$$

where i is the angle of incidence, t is the angle of refraction, n_w is the refractive index of the window and n is the refractive index of the vapor. The notation $\parallel$ represents the case where the light is polarized in the plane of incidence, while $\perp$ means that the polarization is perpendicular to the plane of incidence. The refractive index of the vapor is given by $n = \sqrt{\varepsilon}$, where ε is the dielectric coefficient of the vapor. For a very dense atomic vapor, the homogeneous broadening is larger than Doppler broadening

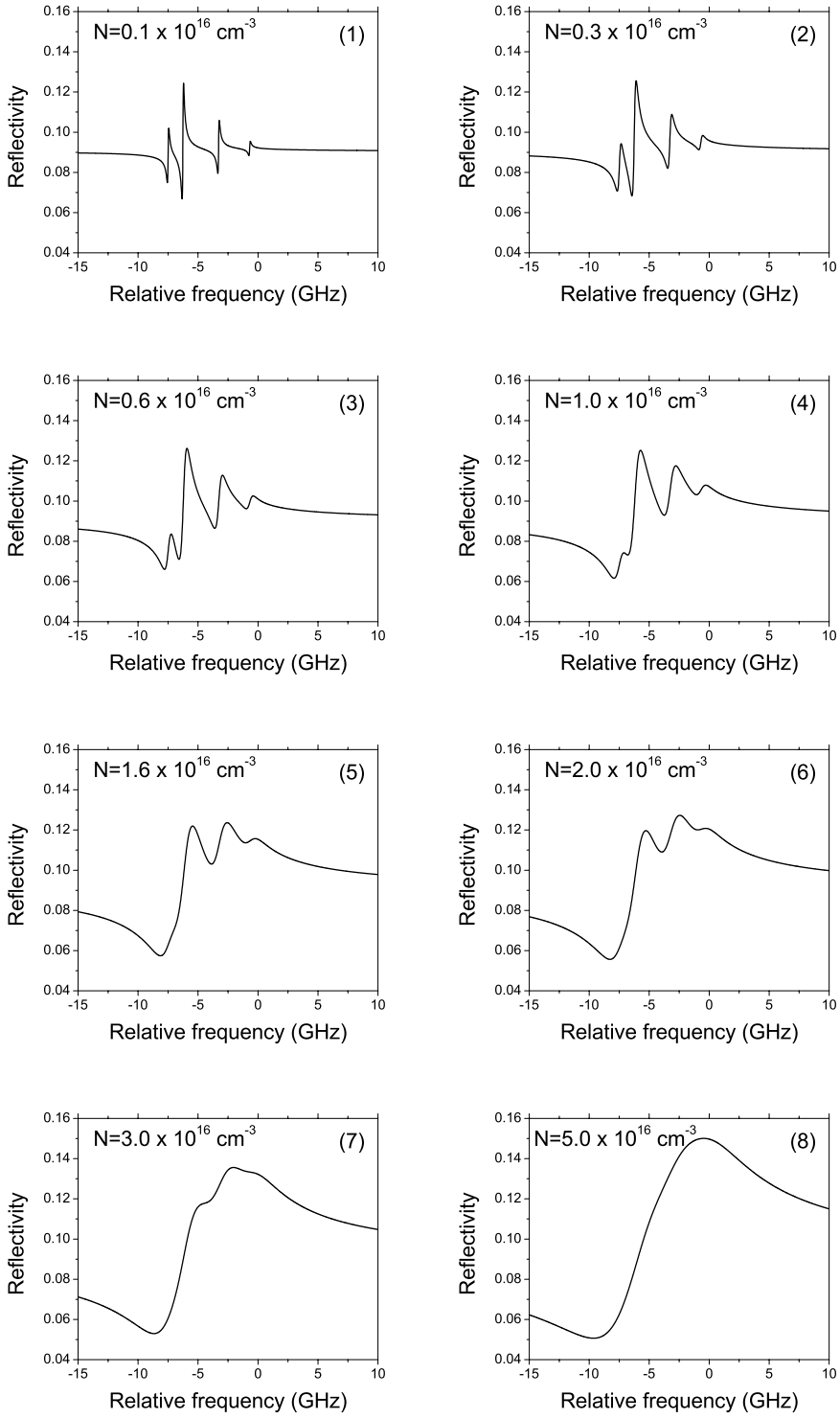

Fig. 51. The calculated reflection spectra from the interface of cell window and Rb vapor. The spectrum is broadened as the atomic density increases.

and the dielectric coefficient ε can be written as the following,

$$\varepsilon = 1 + \frac{kN}{\Delta\omega - ikN}, \tag{7.2}$$

where $\Delta\omega$ is the frequency detuning from the resonance frequency, N is the atomic density. The constant k is given by $k = fcr_e\lambda$ with r_e the classical radius of electron, f the oscillator strength of the transition, λ the wavelength and c the speed of light in vacuum. Using equations (7.1, 7.2), one can calculate the reflection spectrum which is dependent on the atomic density. As an example, the reflection spectra at different atomic density from $N = 0.1 \times 10^{16}$ cm^{-3} to $N = 5 \times 10^{16}$ cm^{-3} are shown in Fig. 51.

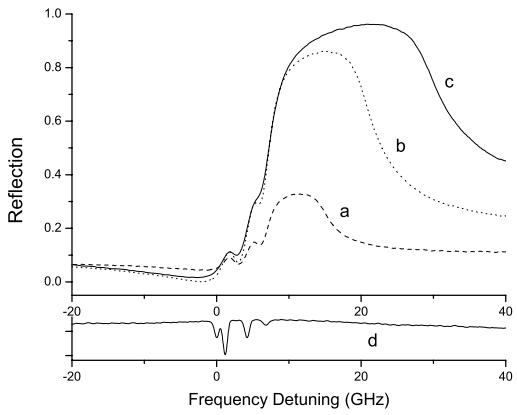

Fig. 52. Reflection spectra with the incident angle of 76° for different atomic densities. (a) atomic density $6.6 \times 10^{15} cm^{-3}$; (b) atomic density $9.0 \times 10^{15} cm^{-3}$; (c) atomic density $1.2 \times 10^{16} cm^{-3}$; (d) absorption spectrum as frequency reference.

For the sake of simplicity, the reflection spectrum is usually investigated at the normal incident angle. Few investigations have also been extended to the oblique incidence such as the incidence at Brewster angle [179]. It is of special interest to study the reflection spectrum at very large angles such that the frustrated total internal reflection occurs [180]. In Fig. 52, we show the reflection spectra with incident

angle of 76° at different atomic densities. The spectral profiles are featured with a flat top and a steep rising slope. This feature can be used to develop an optical filter with a very narrow linewidth which can not be realized by a dichroic filter. Moreover, the filter linewidth is adjustable within a range by changing the atomic density.

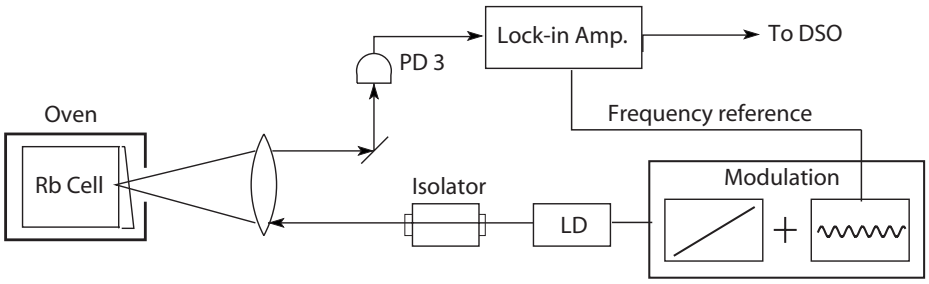

Fig. 53. Experimental schematic for the frequency modulated reflection spectrum. The laser is driven by a slow ramp and a fast modulation. A lock-in amplifier is used to detect small changes in the spectrum.

As the atomic density increases, the reflection spectrum becomes broader and the hyperfine structures become less pronounced. One way to increase the sensitivity and reveal small changes in the reflection spectrum is to use the frequency modulated reflection spectrum. The method takes the advantage of a lock-in amplifier to improve the sensitivity. An experimental schematic is shown in Fig. 53. In additional to the frequency scan (shown as a slope in the figure), a higher frequency cosine wave is used to modulate the laser frequency. The frequency reference for the lock-in amplifier is taken from the cosine wave. After being processed by the lock-in amplifier, the signal is recorded by an oscilloscope. The processed signal can be understood as the derivative of the reflection spectrum with respect to the frequency. This method is useful to study small changes in the spectrum and it will be used in the following sections.

B. Reduce dipole-dipole interaction in a dense vapor *

The improvement of the spectral resolution of atomic and molecular lines is very important for general research and for applications. There are many approaches for eliminating inhomogeneous spectral broadening: for example, in gases, Doppler-free saturation spectroscopy, or in solids, the hole-burning technique [181]. It is still a challenge to reduce the homogenous broadening of spectral lines caused by the interactions between atoms or molecules. For instance, the spectral resolution is limited by the broadening due to dipole-dipole interaction in the reflection spectrum of a highly dense atomic vapor. One way to improve the resolution is to create a narrow structure inside the homogeneously broadened line using the technique of hole burning, attributed to the influence of coherent population oscillations [175, 182]. A more direct way is to reduce the dipole-dipole interaction by partially exciting atoms using an additional pump laser beam [176, 177].

In this section, we discuss the use of the excitation dependence of the dipole-dipole interaction to improve the spectral resolution of self-broadened lines, when the atomic collision induced homogeneous spectral width is broader than the inhomogeneous Doppler width. We experimentally study the selective reflection from an interface between a transparent dielectric and a dense rubidium vapor when the vapor is incoherently excited by a pump laser. We found that the dipole-dipole interaction can be reduced in the presence of the pump laser and the width of spectrum becomes narrower. This reduction of spectral width can be used to improve the resolution of spectroscopy of dense media.

---

*Part of the data reported in this section is reprinted with permission from "*Improvement of spectral resolution by using the excitation dependence of dipole-dipole interaction in a dense atomic gas,*" by H. Li *et al.*, Appl. Phys. B **91**, 229 (2008), Copyright by Springer.

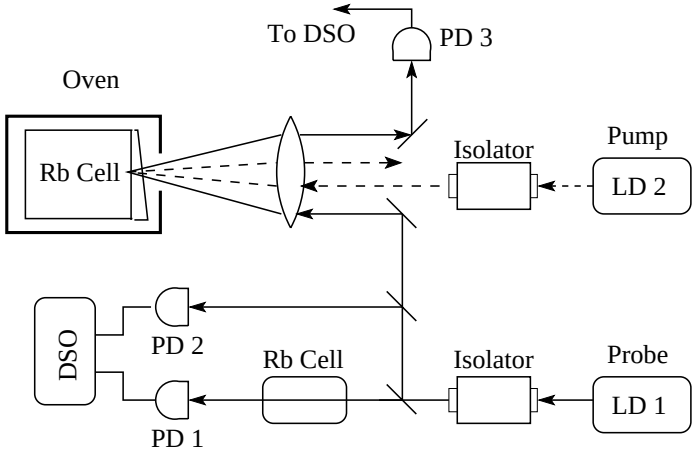

Fig. 54. Reflection spectroscopy with a pump laser. LD - laser diode, PD - photo detector, DSO - digital storage oscilloscope.

The experiment is performed with a typical reflection spectroscopy setup with an additional pump laser shown in Fig. 54. A sapphire cell filled with Rb vapor (natural isotope abundance) is installed in an oven which can heat the cell to 350 °C. Windows of the cell are made of Garnet crystal which is free of birefringence. The windows are slightly wedged in order to separate the reflections from the two surfaces of the window. The probe beam comes from a free running laser diode, LD1 (with linewidth 18 MHz), which is scanning in frequency over a range of 25 GHz near the D_2 absorption line of Rb atoms (780 nm). The probe beam is sent to the window of the cell at a near-normal angle of incidence. The selective reflection spectrum is recorded by PD3. To establish a frequency reference, the absorption spectrum of Rb vapor in a second cell at room temperature is recorded by PD1. The signal from PD2 is used to calibrate the LD1 intensity variations due to injection current scanning. Another laser diode, LD2, provides a pump beam with the power $P = 120$ mW. Its beam is sent to the window at a near-normal incident angle as well. Focused by a lens, the two beams are superposed at a spot with diameter $d \approx 0.1$ mm on the interface between the Rb vapor and the window.

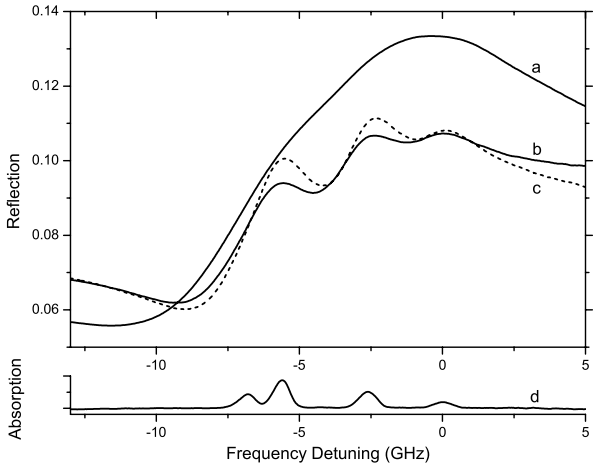

Fig. 55. Observed reflection spectra. (a) the linear reflection spectrum at $N = 3.5 \times 10^{16}$ cm^{-3}; (b) the saturated reflection spectrum with $P_{pump} = 120$ mW at $N = 3.5 \times 10^{16}$ cm^{-3}; (c) the linear reflection spectrum at $N = 1.2 \times 10^{16}$ cm^{-3}; (d) the absorption spectrum of the low density Rb vapor as the frequency reference.

The experimental results are shown in Fig. 55. Curve (a) shows the linear (no pump laser) reflection spectrum of the rubidium vapor with the atomic density $N = 3.5 \times 10^{16}$ cm^{-3}. At this atomic density, the spectrum is so broad that the hyperfine structures are not resolved. As shown in curve (b), however, the structure shows up at the same atomic density ($N = 3.5 \times 10^{16}$ cm^{-3}) when we apply the pump laser ($P = 120$ mW) tuned by 21 GHz into the red wing of the absorption line. Curve (d) is the D_2 line room temperature absorption spectrum of rubidium atoms.

As discussed in previous papers [176, 177], coherent effects can be neglected in the case when the pump laser is far-detuned from the resonance lines. In this case, the rubidium atoms are partially excited by the pump laser. The saturation is enhanced by the radiation trapping effect [176, 177]. To estimate how much the dipole-dipole interaction is reduced, we decrease the atomic density of the Rb vapor

until the reflection spectrum without the pump laser has a similar profile to that of curve (b). The result is shown as curve (c), which is the reflection spectrum recorded without pump laser at the atomic density $N = 1.2 \times 10^{16}$ cm^{-3}. Thus, the pump laser is able to reduce the dipole-dipole interaction to that of Rb vapor with three times less atomic density. This also shows that the width is reduced by a factor of three with the presence of the pump laser.

Note that the incoherent excitation of dense gas can strongly decrease homogeneous broadening of resonant lines. The inhomogeneous broadening due to the dipole-dipole interaction in solids can also be reduced by using the so-called "magic-angle" technique [183]. Both techniques of spectral narrowing may be used to improve spectral resolution.

The qualitative features of experimental results can be explained in terms of the dielectric coefficient ε of the rubidium vapor. The reflectivity can be calculated by the Fresnel formulas with the index of refraction given by $n = \sqrt{\varepsilon}$. Without the saturation, the dielectric coefficient ε for a two level system is given by the expression [165, 184]

$$\varepsilon(\Delta\omega) = 1 + \frac{kN}{\Delta\omega + \Delta\Omega - i\Gamma} \ , \tag{7.3}$$

where N is the atomic density, $\Delta\omega$ is the frequency detuning, $\Delta\Omega$ is the line shift and Γ is the self-broadened linewidth of the transition. The constant k is given by $k = fcr_e\lambda$, here r_e is the classical radius of electron, c is the speed of light, f is the oscillator strength of the transition, and λ is the wavelength. The line shift can be written as $\Delta\Omega = \Delta\omega_L + \Delta\omega_{NL}$, here $\Delta\omega_L$ is the Lorentz shift and $\Delta\omega_{NL}$ represents the non-Lorentz contribution to the line shift. The Lorentz shift is given by $\Delta\omega_L = kN/3$ theoretically [185, 186], both $\Delta\omega_L$ and $\Delta\omega_{NL}$ can be found experimentally [165, 176, 177, 184, 187, 188]. The self-broadened linewidth is given

by $\Gamma = kN\sqrt{g_e/g_g}$, with g_g and g_e the degeneracies of the ground and excited state respectively [189].

For partially excited Rb vapor (incoherent excitation), the fractional population difference between the ground and excited states is defined in [185, 186] as $\eta = (N_g - N_e g_g/g_e)/N$, where N_g and N_e are respectively the atomic densities of the ground and excited states. Zero excitation is represented by $\eta = 1$, and maximum excitation is signified by $\eta = 0$. According to Manassah's approach [186], the atomic density N in Eq. (1), as well as in the expressions of $\Delta\omega_L$, should be replaced by $N\eta$. Also the self-broadened linewidth should be rewritten as [176, 177]

$$\Gamma = kN_g\sqrt{g_e/g_g}\ . \tag{7.4}$$

The ground state density N_g can be calculated by the definition of η and $N = N_g + N_e$. In Rb vapor, we must take account the collisional mixing of the $5^2P_{3/2}$ and $5^2P_{1/2}$ states. The expression for ε in the partially excited vapor is therefore given by

$$\varepsilon(\Delta\omega) = 1 + \frac{kN\eta}{\Delta\omega + \Delta\Omega - ik\sqrt{g_e/g_g}N_g}\ . \tag{7.5}$$

Using this theoretical model, we perform a simulation of the reflection spectrum. In our experiment, there are four lines in the absorption spectrum because the cell contains both ^{87}Rb and ^{85}Rb atoms. These are taken into account in the simulation. The results are shown in Fig. 3, where curve (1) shows the calculated reflection spectrum at an atomic density of $N = 3.5 \times 10^{16}$ cm^{-3} in the absence of partial excitation. With partial excitation, the calculated reflection spectrum is shown in curve (2), which corresponds to $\eta = 0.4$. We see that the numerical simulation spectrum is in a good agreement with the spectrum obtained in the experiment.

To summarize the section, we have experimentally studied the dipole-dipole

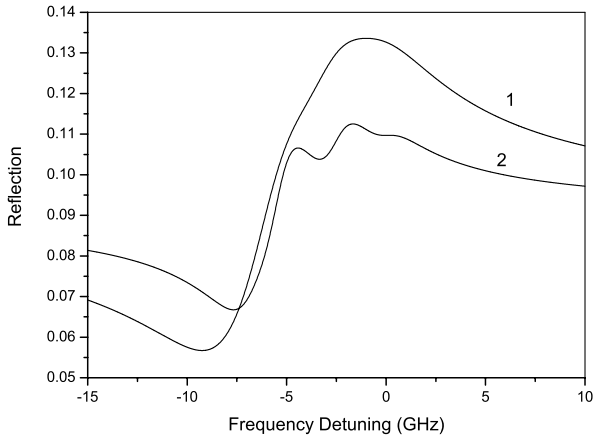

Fig. 56. The numerical simulation of reflection spectrum. (1) the linear reflection spectrum at $N = 3.5 \times 10^{16}$ cm^{-3}; (2) the narrowed reflection spectrum with $\eta = 0.4$ at $N = 3.5 \times 10^{16}$ cm^{-3}.

broadened reflection spectrum from the interface between a Garnet crystal and a dense Rb vapor. We have shown that the dipole-dipole interaction can be dramatically reduced when the rubidium vapor is excited by a strong pump laser. By using this technique, we have resolved hyperfine structures of Rb D_2 line hidden by collisional broadening. We also present a numerical simulation, which agrees with the experimental results. In this way, one can obtain a remarkable narrowing of dipole-dipole broadened spectra in dense media. This could be used to improve the resolution of spectroscopy of dense media.

C. Excitation dependence of self-broadening in a dense vapor *

As shown in the previous section, the spectral broadening is dominated by the homogeneous self-broadening for a dense vapor in which the dipole-dipole interaction between atoms in the ground and excited states can not be neglected. It is necessary to know the mechanism of self-broadening and the nonlinear optical response of such dense media.

There was a common opinion that calculations of self-broadening can be performed by using the two-particle approximation in the fast collision limit (impact collisions) as well as in the opposite limit, static interactions [163, 189, 190, 191, 192]. In [163], the theory of self-broadening is developed on the basis of disordered exciton in a dense resonance medium, in which many particle interaction should be taken into account. By using this model it was shown that the self-broadening is a combination of collision and static atomic interactions. A ratio of the static width to the collision width is independent on atomic density in a wide range where thermal motion of atoms can be neglected.

It has been shown that the probing of the homogeneous and inhomogeneous contributions to the linewidth can be performed efficiently by nonlinear optical methods such as photon echoes and hole burning [193]. The inhomogeneous component of the spectral line could be sensitive to the optical saturation. Recently by using time resolved femto-second spectroscopy, the non-Markovian collision dynamics and the bi-exponentional correlation of energy level fluctuations have been observed in a dense potassium vapor and simulations of molecular dynamic are in good agreement

*Part of the data reported in this section is reprinted with permission from "*Excitation dependence of resonance line self-broadening at different atomic densities,*" by H. Li *et al.*, J. Phys. B **42**, 065203 (2009), Copyright by Institute of Physics and IOP Publishing. The article is available online at http://www.iop.org/journals/jphysb.

with experimental results [194, 195]. The slow exponential component is attributed to long-range resonant attraction in a dense atomic vapor. By using CW pump-probe technique, the excitation dependence of the self-broadening is observed in rubidium [176, 196] and potassium [177, 197] vapors. Nevertheless, note that in these papers the measurements have been performed only at selected atomic densities.

In the current section the selective reflection spectra from the interface between the cell window and rubidium vapor are recorded in the presence of a far-detuned pump beam. We study the excitation dependence of self-broadening of a resonance atomic line at different atomic densities in the range where self-broadening of atomic line is stronger than Doppler broadening. The excitation dependence of self-broadening is found to be independent on the atomic density. These results support the disorder exciton based theory of self-broadening[163].

The experiment is performed with a pump-probe scheme shown in Fig. 54. To improve the sensitivity, we use the frequency modulated reflection spectrum described above in Fig. 53. The reflected beam from the interface between the rubidium vapor and the window is sent to a photodetector (PD). The signal from the photodetector is processed by a lock-in amplifier while we frequency modulate the probe laser with modulation depth of 37 MHz at frequency of 8 kHz. Frequency modulated reflection spectrum is used to improve the signal to noise ratio in our experiment, and it can reveal subtle details of change in reflectivity. A typical frequency modulated reflection spectrum is shown in Fig. 57 as curve (a) which was obtained at the atomic density N=1.3×10^{17} cm^{-3}. The dipole-dipole interaction and collisional broadening dominate at this atomic density, the spectral width due to self-broadening is larger than the ground state hyperfine splitting and the ground state hyperfine structures in reflection spectra that can be seen at low atomic density are not resolved. While we apply the pump laser beam, atoms are partially excited and the dipole-dipole interaction is

reduced. Thus, the self-broadened line width is also reduced [176, 177, 196, 197], and the ground state hyperfine structures start to be revealed as described in [176, 196]. The narrowed frequency modulated spectrum with pump power P=180 mW is shown as curve (b) in Fig. 57.

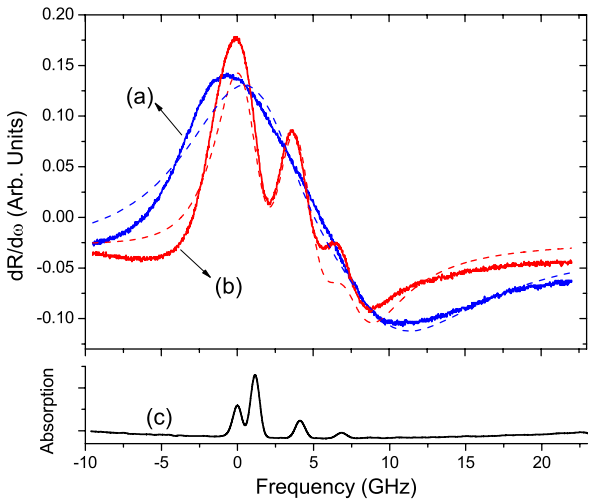

Fig. 57. FM reflectivity spectra at atomic density N=1.3×10^{17} cm^{-3}. Blue (a) and red (b) solid curves correspond to the cases without pump laser and with pump laser (P=180 mW), respectively. The dashed curves are corresponding fitting results. Curve (c) is the absorption spectra of a reference Rb cell, where the ground state hyperfine splitting is resolved.

As described in [177], the reflection spectra as well as the FM reflection spectra can be interpreted in terms of the dielectric coefficient of atomic vapor. Taking into account the excitation, the dielectric coefficient ε of a two-level atomic system is given as

$$\varepsilon(\omega) = 1 + \frac{k\eta N}{\Delta\omega + \Delta\Omega - i\Gamma}, \tag{7.6}$$

where N is the atomic density, $\Delta\omega$ is the frequency detuning, $\Delta\Omega$ is the overall

line shift which includes Lorentz and non-Lorentz shift, and Γ is the self-broadened linewidth. The constant k is given by $k = fcr_e\lambda$, where f the oscillator strength of transition, r_e the classical radius of electron, λ the wavelength of transition, and c is the speed of light in vacuum. An excitation factor η is defined as the fractional population difference between ground and excited states

$$\eta = \frac{N_g - N_e g_g/g_e}{N}, \tag{7.7}$$

where N_g and N_e are the ground and excited state atomic densities respectively, g_g and g_e are the degeneracies of the ground and excited states respectively. Maximum excitation corresponds to $\eta = 0$ and zero excitation $\eta = 1$. Using this expression for the dielectric coefficient ε and Fresnel formula, we are able to calculate the reflectivity and FM spectra which is the derivative of reflectivity with respect to frequency.

In order to obtain the width and excitation factor from the experimental data, we use the expression of FM spectra to fit the experiment data by leaving the self-broadened width Γ, the excitation factor η and the line shift $\Delta\Omega$ as fitting parameters. The excitation factor η is normalized to unity for the case where no pump laser is applied. In our experiment, Rb vapor contains natural abundance of ^{85}Rb and ^{87}Rb which gives rise to four doppler-broadened absorption lines in the absorption spectra. All of four components are taken into account in the fitting of reflection spectra. Each component is given a normalized oscillator strength. The dashed curves in Fig. 57 are the examples of the fitting. For the case without the pump laser, the fitted width is 13.0 ± 0.3 GHz and $\eta = 1.0$; for the case with the pump laser (laser power P=180 mW), the fitted width is 4.98 ± 0.05 GHz and $\eta = 0.36$. At the same atomic density (N=1.3×10^{17} cm^{-3}), the FM spectrum is recorded when we apply the pump laser with different powers. The fitting of these FM spectra gives the widths corresponding to the different excitation factors. The fitting results are shown as the red squares

in Fig. 58, where the width is plotted as a function of the excitation factor η. The dashed line in Fig. 58 is a linear fit ($y = a + bx$, where the dependent variable x represents the excitation η and a and b are fitting parameters) of the excitation dependence of the width at atomic density N=1.3×10^{17} cm^{-3}, and the slope (fitting parameter b) is 12.7 GHz.

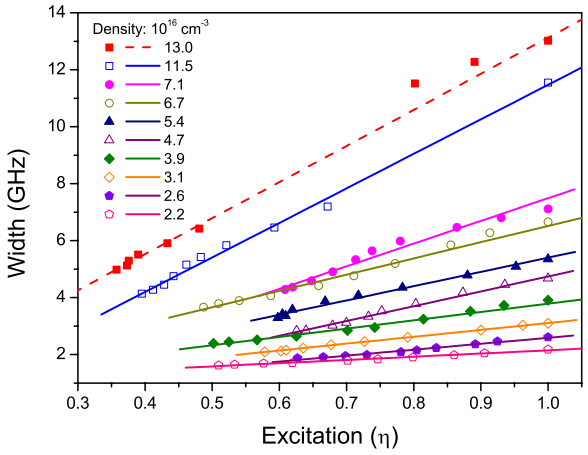

Fig. 58. The fitting value of the width is plotted as a function of the excitation factor η. Different colors represent the results at different atomic density from N=1.3×10^{17} cm^{-3} to N=2.2×10^{16} cm^{-3}. The straight lines are the linear fits.

We determine the widths and excitation factors by measuring and fitting the FM reflection spectra at different atomic densities from N=1.3×10^{17} cm^{-3} to N=2.2×10^{16} cm^{-3}. The measured density dependence of the self-broadened rubidium D_2 linewidth is the same as in Refs. [198, 199]. The excitation dependence of the width for different atomic densities is shown in Fig. 58 with different colors. The corresponding linear fit gives the slope (width/η) for each density. In Fig. 59 (left), the slope is plotted as a function of the atomic density. The solid line is a linear fit. If the slope for each

density is normalized by taking the ratio of the slope to the width without the pump laser at each density, the normalized slopes are close to unity. As shown in Fig. 59 (right), the value of the normalized slope is 0.90 ± 0.05. According to our simple model for the fit, the normalized slope is density independent. It indicates that the self-broadening at high atomic density is a combination of collision and static spectral broadening (inhomogeneous profile).

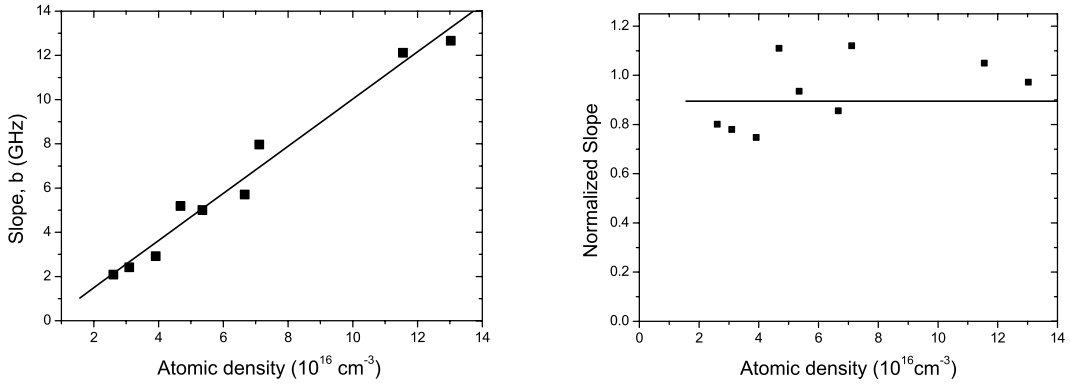

Fig. 59. The slope (left figure) and the normalized slope (right figure) of the excitation dependence on the atomic density is plotted as a function of the atomic density. Squares are the results of fitting from Fig. 58. The solid straight lines are linear fits.

We have observed that the excitation dependence of self-broadening is the same in the range of atomic density from 2.2×10^{16} to 1.3×10^{17} cm^{-3}, where dipole-dipole interactions are a dominant source of spectral broadening. Our results support the predictions of the theoretical model developed in Ref. [163]. The obtained results can be useful for understanding of excitation processes in a condensed media such as solutions, glasses, polymers, proteins and molecular crystals. In atomic gases it will be interesting to study a possible transition from many body interactions (disordered excitons) [163, 194, 195, 176] to the resonance two-body interaction (impact collisions)

at lower atomic densities [189, 190]. Probably the studies will require applications of non-linear optical methods in frequency and time domain as the complimentary spectroscopic techniques. We shall note that additional information about the dipole-dipole interaction in a dense gas may be obtained by using a nano-cell [200].

CHAPTER VIII

CONCLUSION

In summary, we have studied the interaction between electromagnetic fields, both in optical and radio frequency domain, and dense rubidium atomic vapors. The study includes the control of laser fields over transmission, spatial distribution and noise feature in coherent media; the atomic excitation by few-cycle radio frequency pulses interacting with Zeeman sublevels; and the reflection spectroscopy on a highly dense atomic vapor. The main results of the study are the following:

1. The time response of EIT to a rapid variation of optical phase has been studied. We have observed a very fast growth of the absorption when the phase of optical field abruptly changes, followed by a slow return to the level of steady-state absorption. The recovery time decreases with increasing optical power. The low power limit of the recovery time is determined by the ground state relaxation time which, in our case, is the time-of-flight of atoms through laser beam.

2. We have studied the so called close-Λ system formed by coupling two optical fields and a microwave field with a three level system. We found that the transmission of the probe beam depends on the relative phase between the optical and microwave fields. Both constructive and destructive interferences in EIT have been observed.

3. Spatial control of laser beam can be realized in a coherent medium by arranging the spatial distribution of laser fields. We have demonstrated an atomic gas prism which processes an extreme angular dispersion (10^3 nm^{-1}) and can optically steer an optical beam. We have also demonstrated the possibility to create an optical structure with the size smaller than the diffraction limit.

4. We have studied the intensity correlation of atomic excess noise in both EIT and NMOR. The atomic excess noise can be correlated and anti-correlated depending

on specific conditions. The study of power spectra of intensity fluctuations shows that we can reduce or eliminate the atomic excess noise using the correlation or anti-correlation.

5. We have developed a technique in which few cycle radio frequency pulses interact with ground state Zeeman sublevels of rubidium atoms. The radio frequency pulses can simulate short laser pulses in optical domain and their interaction with atoms. We have studied the off resonant excitation by short pulses and the carrier-envelope phase effect on atomic excitation by few cycle pulses.

6. We have studied the selective reflection from the interface between a glass window and dense rubidium atomic vapor. The spectrum is strongly broadened due to the dipole-dipole interaction as we increase the atomic density. We found that applying an additional pump laser to partially excite atoms can reduce the dipole-dipole interaction, thus reduce the broadening and increase the spectral resolution. The excitation dependence of the broadening at different atomic densities have also been studied.

REFERENCES

[1] M. O. Scully and M. S. Zubairy, *Quantum Optics* (Cambridge University Press, Cambridge, UK, 1997).

[2] E. Arimondo, in *Progress in Optics, Vol 35* (Elsevier Science Publ B V, Amsterdam, 1996), vol. 35 of *Progress in Optics*, pp. 257–354.

[3] S. E. Harris, Phys. Today **50**, 36 (1997).

[4] M. O. Scully, Phys. Rep. **219**, 191 (1992).

[5] M. O. Scully, Phys. Rev. Lett. **67**, 1855 (1991).

[6] A. S. Zibrov, M. D. Lukin, L. Hollberg, D. E. Nikonov, M. O. Scully, H. G. Robinson, and V. L. Velichansky, Phys. Rev. Lett. **76**, 3935 (1996).

[7] V. A. Sautenkov, Y. V. Rostovtsev, H. Chen, P. Hsu, G. S. Agarwal, and M. O. Scully, Phys. Rev. Lett. **94**, 233601 (2005).

[8] L. V. Hau, S. E. Harris, Z. Dutton, and C. H. Behroozi, Nature **397**, 594 (1999).

[9] M. M. Kash, V. A. Sautenkov, A. S. Zibrov, L. Hollberg, G. R. Welch, M. D. Lukin, Y. Rostovtsev, E. S. Fry, and M. O. Scully, Phys. Rev. Lett. **82**, 5229 (1999).

[10] A. B. Matsko, O. Kocharovskaya, Y. Rostovtsev, G. R. Welch, A. S. Zibrov, and M. O. Scully, Adv. At., Mol., Opt. Phys. **46**, 191 (2001).

[11] A. B. Matsko, Y. V. Rostovtsev, H. Z. Cummins, and M. O. Scully, Phys. Rev. Lett. **84**, 5752 (2000).

[12] A. B. Matsko, Y. V. Rostovtsev, M. Fleischhauer, and M. O. Scully, Phys. Rev. Lett. **86**, 2006 (2001).

[13] Y. V. Rostovtsev, Z. E. Sariyanni, and M. O. Scully, Phys. Rev. Lett. **97**, 113001 (2006).

[14] K. J. Boller, A. Imamoglu, and S. E. Harris, Phys. Rev. Lett. **66**, 2593 (1991).

[15] J. P. Marangos, J. Mod. Opt. **45**, 471 (1998).

[16] M. Fleischhauer, A. Imamoglu, and J. P. Marangos, Rev. Mod. Phys. **77**, 633 (2005).

[17] D. Budker, D. F. Kimball, S. M. Rochester, and V. V. Yashchuk, Phys. Rev. Lett. **83**, 1767 (1999).

[18] E. E. Mikhailov, V. A. Sautenkov, Y. V. Rostovtsev, and G. R. Welch, J. Opt. Soc. Am. B **21**, 425 (2004).

[19] R. Coussement, Y. Rostovtsev, J. Odeurs, G. Neyens, H. Muramatsu, S. Gheysen, R. Callens, K. Vyvey, G. Kozyreff, P. Mandel, R. Shakhmuratov, and O. Kocharovskaya, Phys. Rev. Lett. **89**, 107601 (2002).

[20] A. V. Turukhin, V. S. Sudarshanam, M. S. Shahriar, J. A. Musser, B. S. Ham, and P. R. Hemmer, Phys. Rev. Lett. **88**, 4 (2001).

[21] S. E. Harris, Phys. Rev. Lett. **85**, 4032 (2000).

[22] Y. Rostovtsev, A. B. Matsko, R. M. Shelby, and M. O. Scully, Opt. Spectrosc. **91**, 490 (2001).

[23] C. Y. Ye, A. S. Zibrov, Y. V. Rostovtsev, and M. O. Scully, Phys. Rev. A **65**, 043805 (2002).

[24] C. Y. Ye, V. A. Sautenkov, Y. V. Rostovtsev, and M. O. Scully, Opt. Lett. **28**, 2213 (2003).

[25] H. Xiong, M. O. Scully, and M. S. Zubairy, Phys. Rev. Lett. **94**, 023601 (2005).

[26] M. O. Scully, Phys. Rev. Lett. **55**, 2802 (1985).

[27] M. O. Scully and M. S. Zubairy, Phys. Rev. A **35**, 752 (1987).

[28] W. Schleich, M. O. Scully, and H. G. Vongarssen, Phys. Rev. A **37**, 3010 (1988).

[29] W. Schleich and M. O. Scully, Phys. Rev. A **37**, 1261 (1988).

[30] W. Maichen, F. Renzoni, I. Mazets, E. Korsunsky, and L. Windholz, Phys. Rev. A **53**, 3444 (1996).

[31] E. A. Korsunsky, N. Leinfellner, A. Huss, S. Baluschev, and L. Windholz, Phys. Rev. A **59**, 2302 (1999).

[32] E. A. Korsunsky and D. V. Kosachiov, Phys. Rev. A **60**, 4996 (1999).

[33] D. Kosachiov, B. Matisov, and Y. Rozhdestvensky, Opt. Commun. **85**, 209 (1991).

[34] A. F. Huss, E. A. Korsunsky, and L. Windholz, J. Mod. Opt. **49**, 141 (2002).

[35] Z. Li, L. P. Deng, L. S. Xu, and K. G. Wang, Eur. Phys. J. D **40**, 147 (2006).

[36] K. Yamamoto, K. Ichimura, and N. Gemma, Phys. Rev. A **58**, 2460 (1998).

[37] S. F. Yelin, V. A. Sautenkov, M. M. Kash, G. R. Welch, and M. D. Lukin, Phys. Rev. A **68**, 063801 (2003).

[38] H. Shpaisman, A. D. Wilson-Gordon, and H. Friedmann, Phys. Rev. A **71**, 043812 (2005).

[39] T. Abi-Salloum, J. P. Davis, C. Lehman, E. Elliott, and F. A. Narducci, J. Mod. Opt. **54**, 2459 (2007).

[40] V. A. Sautenkov, H. Li, Y. V. Rostovtsev, G. R. Welch, J. P. Davis, F. A. Narducci, and M. O. Scully, J. Mod. Opt. **56**, 975 (2009).

[41] V. A. Sautenkov, H. Li, Y. V. Rostovtsev, G. R. Welch, J. P. Davis, F. A. Narducci, and M. O. Scully, J. Mod. Opt. **55**, 3093 (2008).

[42] E. Figueroa, F. Vewinger, J. Appel, and A. I. Lvovsky, Opt. Lett. **31**, 2625 (2006).

[43] J. E. Thomas and W. W. Quivers, Phys. Rev. A **22**, 2115 (1980).

[44] W. Franzen, Phys. Rev. **115**, 850 (1959).

[45] M. Arndt, S. I. Kanorsky, A. Weis, and T. W. Hansch, Phys. Rev. Lett. **74**, 1359 (1995).

[46] D. V. Kosachiov and E. A. Korsunsky, Eur. Phys. J. D **11**, 457 (2000).

[47] E. A. Wilson, N. B. Manson, C. Wei, and L. J. Yang, Phys. Rev. A **72**, 063813 (2005).

[48] E. A. Wilson, N. B. Manson, and C. Wei, Phys. Rev. A **72**, 063814 (2005).

[49] M. S. Shahriar and P. R. Hemmer, Phys. Rev. Lett. **65**, 1865 (1990).

[50] A. S. Zibrov, A. B. Matsko, and M. O. Scully, Phys. Rev. Lett. **89**, 103601 (2002).

[51] G. S. Agarwal and T. N. Dey, Phys. Rev. A **68**, 063816 (2003).

[52] O. Kocharovskaya, Y. Rostovtsev, and M. O. Scully, Phys. Rev. Lett. **86**, 628 (2001).

[53] Y. Rostovtsev, O. Kocharovskaya, and M. O. Scully, J. Mod. Opt. **49**, 2637 (2002).

[54] D. F. Phillips, A. Fleischhauer, A. Mair, R. L. Walsworth, and M. D. Lukin, Phys. Rev. Lett. **86**, 783 (2001).

[55] C. Liu, Z. Dutton, C. H. Behroozi, and L. V. Hau, Nature **409**, 490 (2001).

[56] N. S. Ginsberg, S. R. Garner, and L. V. Hau, Nature **445**, 623 (2007).

[57] I. Novikova, A. V. Gorshkov, D. F. Phillips, A. S. Sorensen, M. D. Lukin, and R. L. Walsworth, Phys. Rev. Lett. **98**, 243602 (2007).

[58] I. Novikova, D. F. Phillips, and R. L. Walsworth, Phys. Rev. Lett. **99**, 173604 (2007).

[59] A. V. Gorshkov, A. Andre, M. D. Lukin, and A. S. Sorensen, Phys. Rev. A **76**, 033804 (2007).

[60] A. V. Gorshkov, A. Andre, M. D. Lukin, and A. S. Sorensen, Phys. Rev. A **76**, 033805 (2007).

[61] A. V. Gorshkov, A. Andre, M. D. Lukin, and A. S. Sorensen, Phys. Rev. A **76**, 033806 (2007).

[62] Q. Q. Sun, Y. V. Rostovtsev, J. P. Dowling, M. O. Scully, and M. S. Zubairy, Phys. Rev. A **72**, 031802 (2005).

[63] M. Xiao, Y. Q. Li, S. Z. Jin, and J. Geabanacloche, Phys. Rev. Lett. **74**, 666 (1995).

[64] R. R. Moseley, S. Shepherd, D. J. Fulton, B. D. Sinclair, and M. H. Dunn, Phys. Rev. Lett. **74**, 670 (1995).

[65] R. R. Moseley, S. Shepherd, D. J. Fulton, B. D. Sinclair, and M. H. Dunn, Phys. Rev. A **53**, 408 (1996).

[66] A. G. Truscott, M. E. J. Friese, N. R. Heckenberg, and H. Rubinsztein-Dunlop, Phys. Rev. Lett. **82**, 1438 (1999).

[67] J. A. Andersen, M. E. J. Friese, A. G. Truscott, Z. Ficek, P. D. Drummond, N. R. Heckenberg, and H. Rubinsztein-Dunlop, Phys. Rev. A **63**, 023820 (2001).

[68] R. Kapoor and G. S. Agarwal, Phys. Rev. A **61**, 053818 (2000).

[69] Q. Q. Sun, Y. V. Rostovtsev, and M. S. Zubairy, Phys. Rev. A **74**, 033819 (2006).

[70] V. A. Sautenkov, H. Li, Y. V. Rostovtsev, and M. O. Scully, arXiv:quant-ph/0701229v1 (available online at http://arxiv.org/abs/quant-ph/0701229).

[71] V. Westphal and S. W. Hell, Phys. Rev. Lett. **94**, 143903 (2005).

[72] P. R. Hemmer, A. Muthukrishnan, M. O. Scully, and M. S. Zubairy, Phys. Rev. Lett. **96**, 163603 (2006).

[73] M. Kiffner, J. Evers, and M. S. Zubairy, Phys. Rev. Lett. **100**, 073602 (2008).

[74] A. V. Gorshkov, L. Jiang, M. Greiner, P. Zoller, and M. D. Lukin, Phys. Rev. Lett. **100**, 093005 (2008).

[75] H. Kosaka, T. Kawashima, A. Tomita, M. Notomi, T. Tamamura, T. Sato, and S. Kawakami, Phys. Rev. B **58**, 10096 (1998).

[76] F. Vasey, F. K. Reinhart, R. Houdre, and J. M. Stauffer, Appl. Opt. **32**, 3220 (1993).

[77] M. W. Farn, Appl. Opt. **33**, 5151 (1994).

[78] L. Karpa and M. Weitz, Nature Physics **2**, 332 (2006).

[79] M. Born and E. Wolf, *Principles of Optics: Electromagnetic Theory of Propagation, Interference and Diffraction of Light, 7th ed.* (Cambridge University Press, Cambridge, UK, 1999).

[80] R. Schlesser and A. Weis, Opt. Lett. **17**, 1015 (1992).

[81] S. E. Harris and Y. Yamamoto, Phys. Rev. Lett. **81**, 3611 (1998).

[82] V. Balic, D. A. Braje, P. Kolchin, G. Y. Yin, and S. E. Harris, Phys. Rev. Lett. **94**, 183601 (2005).

[83] M. O. Scully and K. Druhl, Phys. Rev. A **25**, 2208 (1982).

[84] A. N. Boto, P. Kok, D. S. Abrams, S. L. Braunstein, C. P. Williams, and J. P. Dowling, Phys. Rev. Lett. **85**, 2733 (2000).

[85] M. D'Angelo, M. V. Chekhova, and Y. Shih, Phys. Rev. Lett. **87**, 013602 (2001).

[86] K. D. Stokes, C. Schnurr, J. R. Gardner, M. Marable, G. R. Welch, and J. E. Thomas, Phys. Rev. Lett. **67**, 1997 (1991).

[87] J. R. Gardner, M. L. Marable, G. R. Welch, and J. E. Thomas, Phys. Rev. Lett. **70**, 3404 (1993).

[88] J. T. Chang, J. Evers, and M. S. Zubairy, Phys. Rev. A **74**, 043820 (2006).

[89] J. T. Chang, J. Evers, M. O. Scully, and M. S. Zubairy, Phys. Rev. A **73**, 031803 (2006).

[90] S. W. Hell and J. Wichmann, Opt. Lett. **19**, 780 (1994).

[91] E. Betzig, G. H. Patterson, R. Sougrat, O. W. Lindwasser, S. Olenych, J. S. Bonifacino, M. W. Davidson, J. Lippincott-Schwartz, and H. F. Hess, Science **313**, 1642 (2006).

[92] M. J. Rust, M. Bates, and X. W. Zhuang, Nature Methods **3**, 793 (2006).

[93] G. S. Agarwal and K. T. Kapale, J. Phys. B **39**, 3437 (2006).

[94] D. D. Yavuz and N. A. Proite, Phys. Rev. A **76**, 041802 (2007).

[95] H. Li, V. A. Sautenkov, M. M. Kash, A. V. Sokolov, G. R. Welch, Y. V. Rostovtsev, M. S. Zubairy, and M. O. Scully, Phys. Rev. A **78**, 013803 (2008).

[96] T. Haslwanter, H. Ritsch, J. Cooper, and P. Zoller, Phys. Rev. A **38**, 5652 (1988).

[97] H. Ritsch, P. Zoller, and J. Cooper, Phys. Rev. A **41**, 2653 (1990).

[98] T. Yabuzaki, T. Mitsui, and U. Tanaka, Phys. Rev. Lett. **67**, 2453 (1991).

[99] S. Machida, Y. Yamamoto, and Y. Itaya, Phys. Rev. Lett. **58**, 1000 (1987).

[100] D. H. Mcintyre, C. E. Fairchild, J. Cooper, and R. Walser, Opt. Lett. **18**, 1816 (1993).

[101] J. C. Camparo, J. Opt. Soc. Am. B **15**, 1177 (1998).

[102] J. C. Camparo and J. G. Coffer, Phys. Rev. A **59**, 728 (1999).

[103] W. V. Davis, M. Kauranen, E. M. Nagasako, R. J. Gehr, A. L. Gaeta, R. W. Boyd, and G. S. Agarwal, Phys. Rev. A **51**, 4152 (1995).

[104] R. Walser and P. Zoller, Phys. Rev. A **49**, 5067 (1994).

[105] J. Kitching, H. G. Robinson, L. Hollberg, S. Knappe, and R. Wynands, J. Opt. Soc. Am. B **18**, 1676 (2001).

[106] G. Hetet, O. Glockl, K. A. Pilypas, C. C. Harb, B. C. Buchler, H. A. Bachor, and P. K. Lam, J. Phys. B **40**, 221 (2007).

[107] A. B. Matsko, I. Novikova, G. R. Welch, D. Budker, D. F. Kimball, and S. M. Rochester, Phys. Rev. A **66**, 043815 (2002).

[108] J. Ries, B. Brezger, and A. I. Lvovsky, Phys. Rev. A **68**, 025801 (2003).

[109] M. T. L. Hsu, G. Hetet, A. Peng, C. C. Harb, H. A. Bachor, M. T. Johnsson, J. J. Hope, P. K. Lam, A. Dantan, J. Cviklinski, A. Bramati, and M. Pinard, Phys. Rev. A **73**, 023806 (2006).

[110] E. E. Mikhailov and I. Novikova, Opt. Lett. **33**, 1213 (2008).

[111] A. Weis and R. Wynands, Opt. Las. Eng. **43**, 387 (2005).

[112] P. D. D. Schwindt, L. Hollberg, and J. Kitching, Rev. Sci. Inst. **76**, 126103 (2005).

[113] D. Budker, D. F. Kimball, S. M. Rochester, V. V. Yashchuk, and M. Zolotorev, Phys. Rev. A **62**, 043403 (2000).

[114] V. A. Sautenkov, M. D. Lukin, C. J. Bednar, I. Novikova, E. Mikhailov, M. Fleischhauer, V. L. Velichansky, G. R. Welch, and M. O. Scully, Phys. Rev. A **62**, 023810 (2000).

[115] D. Budker, W. Gawlik, D. F. Kimball, S. M. Rochester, V. V. Yashchuk, and A. Weis, Rev. Mod. Phys. **74**, 1153 (2002).

[116] S. M. Rochester, D. S. Hsiung, D. Budker, R. Y. Chiao, D. F. Kimball, and V. V. Yashchuk, Phys. Rev. A **63**, 043814 (2001).

[117] E. B. Alexandrov, M. V. Balabas, A. S. Pasgalev, A. K. Vershovskii, and N. N. Yakobson, Laser Phys. **6**, 244 (1996).

[118] I. K. Kominis, T. W. Kornack, J. C. Allred, and M. V. Romalis, Nature **422**, 596 (2003).

[119] M. P. Ledbetter, V. M. Acosta, S. M. Rochester, D. Budker, S. Pustelny, and V. V. Yashchuk, Phys. Rev. A **75**, 023405 (2007).

[120] J. F. Roch, K. Vigneron, P. Grelu, A. Sinatra, J. P. Poizat, and P. Grangier, Phys. Rev. Lett. **78**, 634 (1997).

[121] M. D. Lukin, A. B. Matsko, M. Fleischhauer, and M. O. Scully, Phys. Rev. Lett. **82**, 1847 (1999).

[122] A. Dantan, J. Cviklinski, E. Giacobino, and M. Pinard, Phys. Rev. Lett. **97**, 023605 (2006).

[123] A. B. Matsko, I. Novikova, M. S. Zubairy, and G. R. Welch, Phys. Rev. A **67**, 043805 (2003).

[124] V. A. Sautenkov, Y. V. Rostovtsev, and M. O. Scully, Phys. Rev. A **72**, 065801 (2005).

[125] L. S. Cruz, D. Felinto, J. G. A. Gomez, M. Martinelli, P. Valente, A. Lezama, and P. Nussenzveig, Eur. Phys. J. D **41**, 531 (2007).

[126] M. Martinelli, P. Valente, H. Failache, D. Felinto, L. S. Cruz, P. Nussenzveig, and A. Lezama, Phys. Rev. A **69**, 043809 (2004).

[127] V. A. Sautenkov, H. Li, Y. V. Rostovtsev, and M. O. Scully, J. Mod. Opt. **54**, 2451 (2007).

[128] T. S. Varzhapetyan, H. B. Li, G. O. Ariunbold, V. A. Sautenkov, Y. V. Rostovtsev, and M. O. Scully, Opt. Commun. **282**, 39 (2009).

[129] H. Li, V. A. Sautenkov, T. S. Varzhapetyan, Y. V. Rostovtsev, and M. O. Scully, J. Opt. Soc. Am. B **25**, 1702 (2008).

[130] V. V. Vassiliev, S. A. Zibrov, and V. L. Velichansky, Rev. Sci. Inst. **77**, 013102 (2006).

[131] V. A. Sautenkov, M. M. Kash, V. L. Velichansky, and G. R. Welch, Laser Phys. **9**, 889 (1999).

[132] P. G. Pappas, M. M. Burns, D. D. Hinshelwood, M. S. Feld, and D. E. Murnick, Phys. Rev. A **21**, 1955 (1980).

[133] A. M. Akulshin, V. A. Sautenkov, V. L. Velichansky, A. S. Zibrov, and M. V. Zverkov, Opt. Commun. **77**, 295 (1990).

[134] H. Chen, H. B. Li, Y. V. Rostovtsev, M. A. Gubin, V. A. Sautenkov, and M. O. Scully, J. Opt. Soc. Am. B **23**, 723 (2006).

[135] S. E. Harris, Phys. Rev. Lett. **70**, 552 (1993).

[136] C. Cohen-Tannoudji, *Atoms in Electromagnetic Fields* (World Scientific Publishing Company, Singapore, 2005).

[137] F. Bloch and A. Siegert, Phys. Rev. **57**, 522 (1940).

[138] T. Brabec and F. Krausz, Rev. Mod. Phys. **72**, 545 (2000).

[139] A. de Bohan, P. Antoine, D. B. Milosevic, and B. Piraux, Phys. Rev. Lett. **81**, 1837 (1998).

[140] G. G. Paulus, F. Grasbon, H. Walther, P. Villoresi, M. Nisoli, S. Stagira, E. Priori, and S. De Silvestri, Nature **414**, 182 (2001).

[141] A. Gurtler, F. Robicheaux, M. J. J. Vrakking, W. J. van der Zande, and L. D. Noordam, Phys. Rev. Lett. **92**, 063901 (2004).

[142] V. Roudnev, B. D. Esry, and I. Ben-Itzhak, Phys. Rev. Lett. **93**, 163601 (2004).

[143] T. M. Fortier, P. A. Roos, D. J. Jones, S. T. Cundiff, R. D. R. Bhat, and J. E. Sipe, Phys. Rev. Lett. **92**, 147403 (2004).

[144] S. A. Diddams, D. J. Jones, J. Ye, S. T. Cundiff, J. L. Hall, J. K. Ranka, R. S. Windeler, R. Holzwarth, T. Udem, and T. W. Hansch, Phys. Rev. Lett. **84**, 5102 (2000).

[145] Y. Y. Yin, C. Chen, D. S. Elliott, and A. V. Smith, Phys. Rev. Lett. **69**, 2353 (1992).

[146] M. Shapiro and P. Brumer, Adv. At., Mol., Opt. Phys. **42**, 287 (2000).

[147] A. Hache, Y. Kostoulas, R. Atanasov, J. L. P. Hughes, J. E. Sipe, and H. M. vanDriel, Phys. Rev. Lett. **78**, 306 (1997).

[148] D. J. Jones, S. A. Diddams, J. K. Ranka, A. Stentz, R. S. Windeler, J. L. Hall, and S. T. Cundiff, Science **288**, 635 (2000).

[149] A. Baltuska, T. Udem, M. Uiberacker, M. Hentschel, E. Goulielmakis, C. Gohle, R. Holzwarth, V. S. Yakoviev, A. Scrinzi, T. W. Hansch, and F. Krausz, Nature **421**, 611 (2003).

[150] A. J. Verhoef, A. Fernandez, M. Lezius, K. O'Keeffe, M. Uiberacker, and F. Krausz, Opt. Lett. **31**, 3520 (2006).

[151] T. Wittmann, B. Horvath, W. Helml, M. G. Schatzel, X. Gu, A. L. Cavalieri, G. G. Paulus, and R. Kienberger, Nature Physics **5**, 357 (2009).

[152] S. Hughes, Phys. Rev. Lett. **81**, 3363 (1998).

[153] N. Doslic, Phys. Rev. A **74**, 013402 (2006).

[154] C. Jirauschek, L. Duan, O. D. Mucke, F. X. Kartner, M. Wegener, and U. Morgner, J. Opt. Soc. Am. B **22**, 2065 (2005).

[155] L. Y. Peng, E. A. Pronin, and A. F. Starace, New J. Phys. **10**, 025030 (2008).

[156] Y. V. Rostovtsev, H. Eleuch, A. Svidzinsky, H. B. Li, V. Sautenkov, and M. O. Scully, Phys. Rev. A **79**, 063833 (2009).

[157] N. F. Ramsey, Phys. Rev. **76**, 996 (1949).

[158] M. O. Scully, Y. Rostovtsev, A. Svidzinsky, and J. T. Chang, J. Mod. Opt. **55**, 3219 (2008).

[159] R. Wood, *Researches in Physical Optics*, vol. 2 (Columbia University Press, New York, 1919).

[160] A. Mitchell and M. Zemansky, *Resonance Radiation and Excited Atoms* (Macmillan, New York, 1934).

[161] A. C. Lauriston and H. L. Welsh, Can. J. Phys. **29**, 217 (1951).

[162] J. P. Woerdman and M. F. H. Schuurmans, Opt. Commun. **14**, 248 (1975).

[163] J. A. Leegwater and S. Mukamel, Phys. Rev. A **49**, 146 (1994).

[164] V. Vuletic, V. A. Sautenkov, C. Zimmermann, and T. W. Hansch, Opt. Commun. **99**, 185 (1993).

[165] J. J. Maki, M. S. Malcuit, J. E. Sipe, and R. W. Boyd, Phys. Rev. Lett. **67**, 972 (1991).

[166] M. Chevrollier, M. Fichet, M. Oria, G. Rahmat, D. Bloch, and M. Ducloy, J. De Phys. **2**, 631 (1992).

[167] D. Bloch and M. Ducloy, Adv. At., Mol., Opt. Phys. **50**, 91 (2005).

[168] N. Papageorgiou, A. Weis, V. A. Sautenkov, D. Bloch, and M. Ducloy, Appl. Phys. B **59**, 123 (1994).

[169] T. A. Vartanyan, Jetp Lett. **41**, 364 (1985).

[170] G. Nienhuis, F. Schuller, and M. Ducloy, Phys. Rev. A **38**, 5197 (1988).

[171] F. Schuller, O. Gorceix, and M. Ducloy, Phys. Rev. A **47**, 519 (1993).

[172] G. Nienhuis and F. Schuller, Phys. Rev. A **50**, 1586 (1994).

[173] A. Weis, V. A. Sautenkov, and T. W. Hansch, Phys. Rev. A **45**, 7991 (1992).

[174] S. Grafstrom, T. Blasberg, and D. Suter, J. Opt. Soc. Am. B **13**, 3 (1996).

[175] V. A. Sautenkov, R. G. Gamidov, and A. Weis, Phys. Rev. A **55**, 3137 (1997).

[176] V. A. Sautenkov, H. vanKampen, E. R. Eliel, and J. P. Woerdman, Phys. Rev. Lett. **77**, 3327 (1996).

[177] H. van Kampen, V. A. Sautenkov, C. J. C. Smeets, E. R. Eliel, and J. P. Woerdman, Phys. Rev. A **59**, 271 (1999).

[178] H. van Kampen, V. A. Sautenkov, E. R. Eliel, and J. P. Woerdman, Opt. Commun. **180**, 81 (2000).

[179] B. Senitzky, Appl. Phys. Lett. **24**, 68 (1974).

[180] A. M. Akulshin, V. L. Velichanskii, A. I. Zherdev, A. S. Zibrov, V. I. Malakhova, V. V. Nikitin, V. A. Sautenkov, and G. G. Kharisov, Sov. J. Quan. Elec. **19**, 416 (1989).

[181] W. Demtroder, *Laser Spectroscopy* (Springer, Berlin, 1996).

[182] R. W. Boyd and S. Mukamel, Phys. Rev. A **29**, 1973 (1984).

[183] P. Anisimov, Y. Rostovtsev, and O. Kocharovskaya, Phys. Rev. B **76**, 094422 (2007).

[184] J. J. Maki, W. V. Davis, R. W. Boyd, and J. E. Sipe, Phys. Rev. A **46**, 7155 (1992).

[185] R. Friedberg, S. R. Hartmann, and J. T. Manassah, Phys. Rep. **7**, 101 (1973).

[186] J. T. Manassah, Phys. Rep. **101**, 359 (1983).

[187] P. Wang, A. Gallagher, and J. Cooper, Phys. Rev. A **56**, 1598 (1997).

[188] S. T. Cundiff, Laser Phys. **12**, 1073 (2002).

[189] E. L. Lewis, Phys. Rep. **58**, 1 (1980).

[190] Y. A. Vdovin and N. Dobrodeev, Sov. Phys. Jetp **28**, 544 (1969).

[191] M. Movre and G. Pichler, J. Phys. B **13**, 697 (1980).

[192] V. Horvatic, M. Movre, R. Beuc, and C. Vadla, J. Phys. B **26**, 3679 (1993).

[193] Y. J. Yan and S. Mukamel, J. Chem. Phys. **94**, 997 (1991).

[194] V. O. Lorenz and S. T. Cundiff, Phys. Rev. Lett. **95**, 163601 (2005).

[195] V. O. Lorenz, S. Mukamel, W. Zhuang, and S. T. Cundiff, Phys. Rev. Lett. **100**, 013603 (2008).

[196] H. Li, T. S. Varzhapetyan, V. A. Sautenkov, Y. V. Rostovtsev, H. Chen, D. Sarkisyan, and M. O. Scully, Appl. Phys. B **91**, 229 (2008).

[197] V. A. Sautenkov, Y. V. Rostovtsev, and E. R. Eliel, Phys. Rev. A **78**, 013802 (2008).

[198] K. Niemax, M. Movre, and G. Pichler, J. Phys. B **12**, 3503 (1979).

[199] R. Kondo, S. Tojo, T. Fujimoto, and M. Hasuo, Phys. Rev. A **73**, 062504 (2006).

[200] T. Varzhapetyan, A. Nersisyan, V. Babushkin, D. Sarkisyan, S. Vdovic, and G. Pichler, J. Phys. B **41**, 185004 (2008).

[201] A. N. Nesmeyanov, *Vapor Pressure Curve of Chemical Elements* (Elsevier, New York, 1963).

APPENDIX A

SOME PROPERTIES OF RUBIDIUM ATOMS

The experiments in this dissertation were performed with the chemical element rubidium. Rubidium is an alkali metal. It was discovered by Robert Bunsen and Gustav Kirchhoff in 1861. The name rubidium originated from Latin *rubidus* (deepest red) for its near infared spectroscopic lines.

Rubidium has the atomic number of 37 and one unbound electron. Its melting point is 39.3 °C and the boiling point is 688 °C. There are twenty six known isotopes of rubidium and two naturally occurring isotopes ^{85}Rb and ^{87}Rb with the natural abundance of 72.2% and 27.8% respectively. ^{85}Rb is a stable isotope while ^{87}Rb is radiative with the half-life of 4.88×10^{10} years.

In our experiments, we fill the rubidium metal into a glass cell and use the saturated rubidium atomic vapor as the sample. The atomic density of the vapor is determined by the temperature at the cold point of cell and can be calculated by the imperical formula [201]

$$N = \frac{\exp(16.963 - \frac{9580.8}{T+273.15}) \times 133.322}{(T + 273.15) \times 1.38 \times 10^{-17}}, \tag{A.1}$$

where the temperature T is in unit of °C and the atomic density is in unit of cm^{-3}. As an example, we plot the atomic density at the temperature from 0 to 300 °C calculated from this formula. It is shown in Fig. 60.

Our experiments involve D lines which are the transitions from the ground state 5S to the first excited state 5P. The state 5P splits into two states $5P_{1/2}$ and $5P_{3/2}$ due to spin-orbit coupling. The transition from $5S_{1/2}$ to $5P_{1/2}$ is called D_1 line, it has the wavelength of 794.760 nm and the excited state has the lifetime of 29.4 ns. The

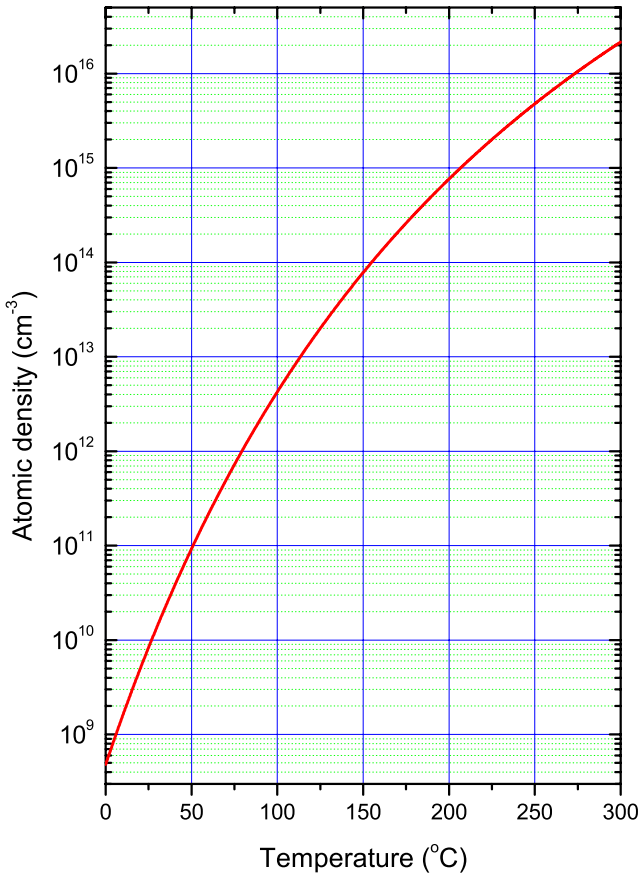

Fig. 60. Atomic density of Rb atoms at different temperatures.

transition from $5S_{1/2}$ to $5P_{3/2}$ is called D_2 line, it has the wavelength of 780.027 nm and the excited state has the lifetime of 27.0 ns. The energy levels of both D_1 and D_2 transitions of ^{85}Rb and ^{87}Rb are shown in Fig. 61 and 62.

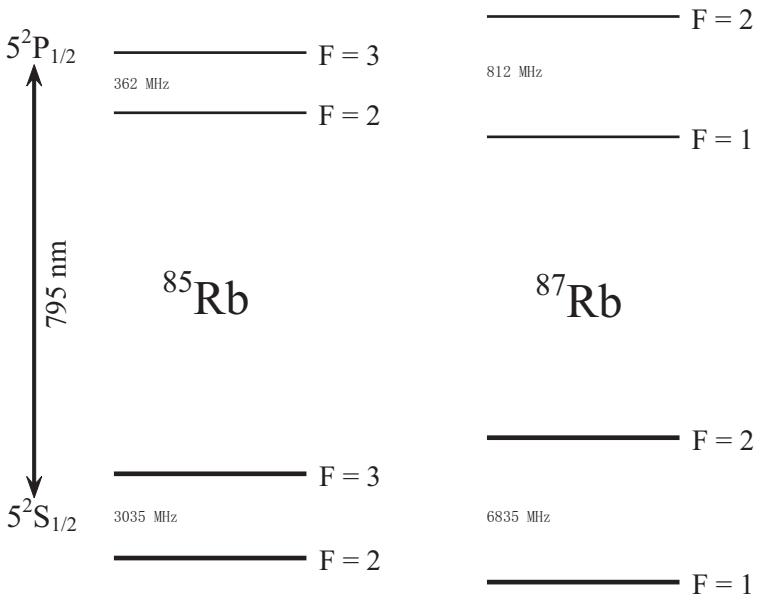

Fig. 61. D_1 transition energy levels of ^{85}Rb and ^{87}Rb, the splitting between hyperfine levels is given in the figure.

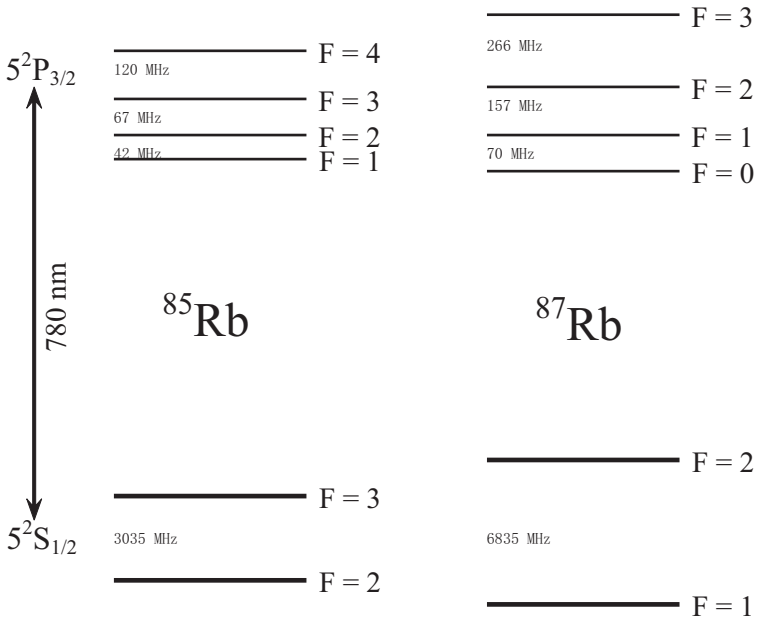

Fig. 62. D_2 transition energy levels of ^{85}Rb and ^{87}Rb, the splitting between hyperfine levels is given in the figure.

VITA

Name: Hebin Li

Address:

Department of Physics

Texas A&M University

College Station, TX 77843-4242, USA

Email:

lihebin@tamu.edu

Education:

2004 - 2010

Ph.D. in Physics, Texas A&M University, College Station, TX

1997 - 2001

B.S. in Physics, Wuhan University, Wuhan, China

The typist for this thesis was Hebin Li.